Chem Soc Rev

REVIEW ARTICLE

Check for updates

Piezo-phototronic effect on photocatalysis, solar cells, photodetectors and light-emitting diodes

Baoying Dai, Gill M. Biesold, Meng Zhang, Haiyang Zou, (iD) Yong Ding, Zhong Lin Wang* and Zhiqun Lin (iD) *

The piezo-phototronic effect (a coupling effect of piezoelectric, photoexcitation and semiconducting properties, coined in 2010) has been demonstrated to be an ingenious and robust strategy to manipulate optoelectronic processes by tuning the energy band structure and photoinduced carrier behavior. The piezo-phototronic effect exhibits great potential in improving the quantum yield efficiencies of optoelectronic materials and devices and thus could help increase the energy conversion efficiency, thus alleviating the energy shortage crisis. In this review, the fundamental principles and challenges of representative optoelectronic materials and devices are presented, including photocatalysts (converting solar energy into chemical energy), solar cells (generating electricity directly under light illumination), photodetectors (converting light into electrical signals) and light-emitting diodes (LEDs, converting electric current into emitted light signals). Importantly, the mechanisms of how the piezo-phototronic effect controls the optoelectronic processes and the recent progress and applications in the above-mentioned materials and devices are highlighted and summarized. Only photocatalysts, solar cells, photodetectors, and LEDs that display piezo-phototronic behavior are reviewed. Material and structural design, property characterization, theoretical simulation calculations, and mechanism analysis are then examined as strategies to further enhance the quantum yield efficiency of optoelectronic devices via the piezo-phototronic effect. This comprehensive overview will guide future fundamental and applied studies that capitalize on the piezo-phototronic effect for energy conversion and storage.

School of Materials Science and Engineering, Georgia Institute of Technology, Atlanta, GA 30332, USA. E-mail: zhong.wang@mse.gatech.edu, Zhiqun.lin@mse.gatech.edu

Baoying Dai received her PhD degree in Materials Science from Nanjing Tech University, China in 2020. She was a visiting student in Prof. Zhiqun Lin's group in the School of Materials Science and Engineering at Georgia Institute of Technology from 2019 to 2021. Currently, she is an Associate Professor in the School of Materials Science and Engineering at Nanjing University of Posts and Tele-communications. Her research focuses on photocatalysts and piezo-phototronic effect-modulated photocatalysis.

Baoying Dai

Gill V. Biesold-McGee received his Bachelor of Science in Materials Science and Engineering at Clemson University in 2017. He is currently a PhD student in the School of Materials Science and Engineering at Georgia Institute of Technology. His research interests include exploring the luminescence properties of semiconductor nanocrystals in a variety of environments.

Gill M. Biesold

1. Introduction

In recent decades, plenty of optoelectronic materials and devices (*i.e.*, photocatalysts, solar cells, photodetectors, and LEDs) have been developed, which witnessed industrial success while meeting most of the energy requirements in our daily life.[1–4] For example, photocatalysts have great potential in remedying the current environmental and energy shortage issues because of their ability to utilize solar light to degrade organic pollutants, generate clean hydrogen fuel, and convert the greenhouse gas carbon dioxide.[5–8] Solar cells can directly convert solar energy into electricity, and their extensive use could provide a strategy to circumvent the troublesome problems arising from the utilization of fossil fuels.[9,10] Photodetectors are designed to generate electrical signals under light illumination, which can be applied in video imaging, optical communication, biomedical imaging, night-vision, and motion detection.[11,12] LEDs are optoelectronic devices that can emit light with wavelengths ranging from near infrared (NIR) to ultraviolet (UV), which has a wide range of applications, including in displays, sterilization of medical equipment, and biological imaging.[13,14] The most critical photo-physical processes in the above-mentioned optoelectronic materials and devices are the generation, separation/recombination, and transfer of photoexcited carriers.[15] Therefore, to improve energy conversion efficiency, tremendous efforts have been focused on tuning the carrier behavior during the optoelectronic process, including the preparation of heterojunction/homojunction nanomaterials (*e.g.*, C-TiO_2/g-C_3N_4 heterojunction, CdS–MoS_2 nanocrystals, $BiVO_4$/TiO_2 nanocomposites, P-doped CdS) to adjust

Meng Zhang

Dr Meng Zhang is a research scientist in Dr Zhiqun Lin's group in the School of Materials Science and Engineering at Georgia Institute of Technology. She received her PhD degree in Engineering Thermophysics from Zhejiang University, China in 2016. Her research interests are centered on solar energy conversion and storage, including perovskite solar cells, CO_2 conversion and utilization, and advanced energy materials.

Haiyang Zou

Dr Haiyang Zou received his MS degree from Worcester Polytechnic Institute, USA, and was honored as the first award of Outstanding Graduate Researcher in WPI. He joined the University of Hong Kong as a senior research assistant in the Department of Mechanical Engineering. He then received his PhD from Georgia Institute of Technology and worked as a postdoctoral research fellow under the supervision of Professor Zhong Lin Wang. His interests include nanomaterials and nanosystems, optoelectronics, energy conversion and harvesting, and piezo-electronics.

Yong Ding

Yong Ding received his PhD from Nanjing University in 2001. After working as a research scientist in Forschungszentrum Juelich, Germany for a year, he joined Georgia Institute of Technology in 2003. Now, he is a principal research scientist at Georgia Institute of Technology. His research interests focus on the nanomaterials characterization, majorly by transmission electron microscopy. He has published over 200 papers and has an h-index of 88.

Zhong Lin Wang

Dr Zhong Lin (ZL) Wang is the Hightower Chair in Materials Science and Engineering, Regents' Professor, and Distinguished Professor at Georgia Institute of Technology. Dr Wang has made original and innovative contributions to the synthesis, discovery, characterization and understanding of the fundamental physical properties of oxide nanobelts and nanowires, as well as applications of nanowires in energy sciences, electronics, optoelectronics and biological science. His discovery and breakthroughs in developing nanogenerators and self-powered nanosystems establish the principle and technological road map for harvesting mechanical energy from environmental and biological systems for powering personal electronics and future sensor networks. He coined and pioneered the field of piezotronics and piezo-phototronics.

the energy band structure and thus facilitate carrier transfer.[16–19] Despite great achievements, further increases in the quantum efficiencies of photocatalysts, solar cells, photodetectors and LEDs encounter some bottlenecks. Hence, it is highly desirable and significant to develop a universal strategy to break the deadlock and thus realize highly efficient energy conversion and storage properties over the above-stated optoelectronic materials and devices.

The piezo-phototronic effect is a three-way coupling of piezoelectric, photoexcitation, and semiconducting properties that can exist in noncentral symmetry semiconductors.[20,21] The quantum efficiencies of optoelectronic semiconductors are often inhibited by the random nature of the motion of photo-induced electrons and holes (some of the carriers get separated, while the others recombine before transferring to the surface of semiconductors).[22] In the semiconductors that exhibit the piezo-phototronic effect, however, the application of external strain can lead to piezoelectric polarization (a piezoelectric field is generated), which can promote preferential transport of carriers to opposite surfaces of the semiconductors.[23,24] Thus, in piezo-phototronic materials the combination of light excitation and strain stands as an intriguing strategy to enhance the separation/recombination and transfer behavior of photo-excited carriers, which is the core physics of the piezo-phototronic effect.[21] Based on this, the piezo-phototronic effect has been employed to improve the performance of a variety of optoelectronic semiconductor materials and devices, including photocatalysts (*i.e.* improving photocatalytic pollution degradation activity, hydrogen evolution reaction, and carbon dioxide conversion efficiency), photodetectors (boosting responsivity), solar cells (increasing power conversion efficiency, PCE) and LEDs (modulating light emission intensity).[25–27] Perhaps most notably, the piezo-phototronic effect enables these enhanced performances by simply applying a static or dynamic strain without altering the major device materials and structures. As such, an increasing number of optoelectronic materials and devices with tailored compositions and structures have been constructed to make full use of the piezo-phototronic effect in the past decades, which well demonstrates the fast development of the piezo-phototronic effect and its great popularity in
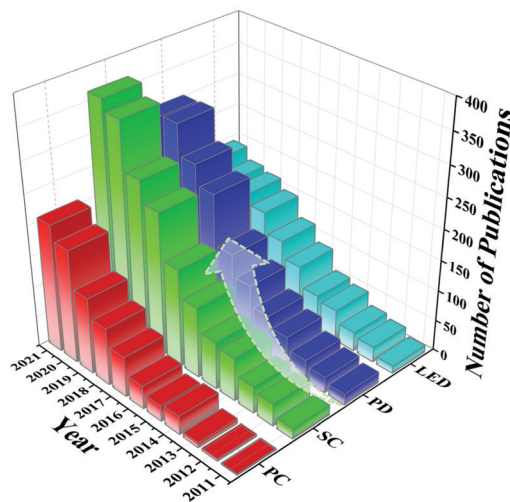

Fig. 1 Summary of the number of publications on optoelectronic materials and devices enabled by the piezo-phototronic effect in each year over the past decade when the term "piezo-phototronic effect" and one of the following terms: "photocatalysts, solar cells, photodetectors, and light-emitting diodes" are searched using Google Scholar. PC, SC, PD and LED represent photocatalysts, solar cells, photodetectors, and light-emitting diodes, respectively.

academic research (Fig. 1). In this regard, a systematic and comprehensive summary of these achievements is urgently needed.

The first paper that systematically reviewed the fundamental principles of the piezo-phototronic effect and its applications in solar cells, photodetectors, LEDs and photoelectrochemical processes was published 9 years ago, which has been cited 414 times by June, 2021.[21] Since that time, other reviews have been published in this area, but they predominately cover the progress of the piezo-phototronic effect and its applications in one specific field (photocatalysts, solar cells, photodetectors or LEDs). For example, Lun Pan and co-authors highlighted the piezo-phototronic effect on promoting the performance of photocatalysts, and Caofeng Pan *et al.* examined the progress in piezo-phototronic effect-enhanced light-emitting diodes.[25,27] In addition, Caofeng Pan and co-authors summarized the principles of piezo-phototronics and its applications in photocatalysts, solar cells, photodetectors, and LEDs, but the review focused only on materials with a nanowire structure.[15] Therefore, the existing literature can be enriched by providing a systematic and comprehensive guideline for researchers who work in this field and related disciplines. Notably, no review has examined how the composition and structural design of piezo-phototronic materials can be used to improve the performance of photocatalysts (*e.g.*, photocatalytic hydrogen evolution activity and photocatalytic degradation/conversion rate), solar cells (*e.g.*, short-circuit current (J_{SC}), open-circuit voltage (V_{OC}), and PCE), photodetectors (*e.g.*, responsivity) and LEDs (*e.g.*, light emission intensity). Additionally, to date, there has been no review scrutinizing the synergy of the piezo-phototronic effect and incident light intensity or surface plasmon resonance on optoelectronic processes for further promoting the performance of energy materials and devices.

Dr Zhiqun Lin is a Professor in the School of Materials Science and Engineering at Georgia Institute of Technology. His research interests include electrocatalysis, photocatalysis, solar energy conversion, batteries, semiconductor organic–inorganic nanocomposites, multifunctional nanocrystals, conjugated polymers, block copolymers, hierarchical structure formation and assembly, and surface and interfacial properties.

Zhiqun Lin

Table 1 Summary of all the abbreviations used in the review and the corresponding full terms

Abbreviations	Full terms
LEDs	Light-emitting diodes
PVDF	Polyvinylidene fluoride
CFs	Carbon fibers
NW	Nanowire
PET	Polyethylene terephthalate
RhB	Rhodamine B
MO	Methyl orange
MB	Methyl blue
UV	Ultraviolet
PVDF-HFP	Poly(vinylidene fluoride-co-hexafluoropropylene)
PDMS	Polydimethylsiloxane
PMMA	Polymethyl methacrylate
PS	Polystyrene
PU	Polyurethane
PCE	Power conversion efficiency
S-Q	Shockley–Queisser
J_{SC}	Short-circuit current
V_{OC}	Open-circuit voltage
QDSCs	Quantum dot solar cells
MQW	Multiple quantum well
DSSCs	Dye sensitized solar cells
PSC	Perovskite solar cell
PL	Photoluminescence
ITO	Indium-tin oxide
P3HT	Poly-3-hexylthiophene
PCBM	[6,6]-Phenyl-C61-butyric acid methyl ester
NIR	Near infrared
FNT	Fowler–Nordheim tunneling
HILs	Hole-injection layers
EILs	Electron-injection layers
HTLs	Hole-transport layers
ETLs	Electron-transport layers
HBLs	Hole-blocking layers
EBLs	Electron-blocking layers
MPE	Multiphoton emission
TAPC	4,4′-Cyclohexylidenebis[N,N-bis(p-tolyl)-aniline]
TCTA	Tris(4-carbazoyl-9-ylphenyl)amine
Ir(ppy)$_3$	1,3-Di-9-carbazolylbenzene (mCP):tris(2-phenylpyridinato-C^2,N)iridium(III)
TPBi	1,3,5-Tris(1-phenyl-1H-benzimidazol-2-yl)benzene
PEDOT:PSS	Poly(3,4-ethylenedioxythiophene):poly(sodium-p-styrenesulfonate)

Therefore, in this critical and compelling review paper, we detail the fundamental mechanisms of the piezo-phototronic effect at first. Next, we examine the applications of the piezo-phototronic effect in photocatalysis, solar cells, photodetectors, and LEDs. Third, we scrutinize the challenges facing the widespread applications of piezo-phototronics. Finally, we outline future research directions. Notably, for the convenience of readers, all the abbreviations used in this review are summarized in Table 1.

2. Fundamentals of the piezo-phototronic effect

2.1 The piezoelectric effect and piezoelectric potential

The piezoelectric effect is a coupling effect between mechanical deformation and electrical polarization and was first demonstrated by brothers Pierre and Jacques Curie in 1880.[28] The basic principle of the direct piezoelectric effect is that an external force applied to a dielectric material along its asymmetric direction will generate positive and negative charges on opposite surfaces. When the applied force is removed, the induced charges will disappear and the symmetric crystal structure can naturally produce the piezoelectric effect under strain. It is well known that a wurtzite crystal has a hexagonal structure which exhibits anisotropic properties in the c-axis direction and in the direction perpendicular to the c-axis. In an unstrained wurtzite ZnO crystal structure, the Zn^{2+} cations and O^{2-} anions are tetrahedrally coordinated and the centers of the positive and negative ions are located at the same position. When an external stress is applied at an apex of the tetrahedron, the center of the cations and the center of the anions will be relatively displaced, generating a dipole moment (Fig. 2a).[21] The addition of all the dipole moments over all units in the crystal will form a piezoelectric field, and as a result the macroscopic potential drops along the strain direction in the crystal, which is the piezoelectric potential (Fig. 2b–d).[29]

2.2 The piezo-phototronic effect

As displayed in Fig. 3, the coupling among photoexcitation, semiconducting, and piezoelectric properties can enable new exciting properties.[30] The disciplines of piezotronics, optoelectronics and piezo-phototronics originated from the coupling effects between semiconducting and piezoelectric properties, and semiconducting and photoexcitation properties, and the three-way coupling effect among piezoelectric, photoexcitation and semiconducting properties, respectively. The piezo-phototronic effect widely exists in non-central symmetric semiconductor materials and has been employed to enhance the
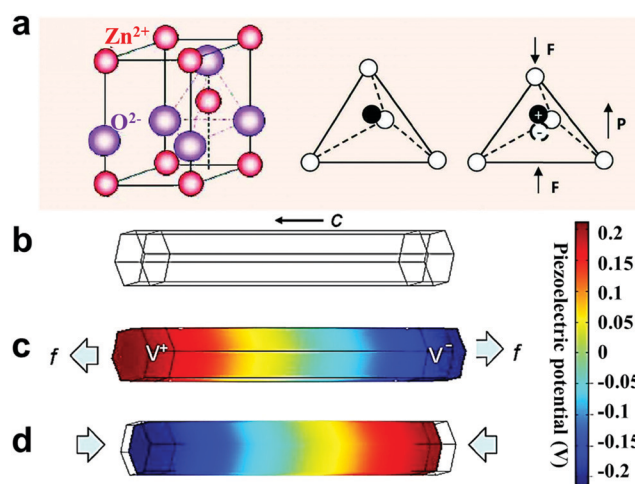

Fig. 2 Piezoelectric potential in a wurtzite crystal. (a) Atomic model of the wurtzite-structured ZnO. Reproduced from ref. 21 with permission from WILEY-VCH Verlag GmbH & Co. KGaA, Weinheim, copyright 2012. Numerical calculation of the piezoelectric potential distribution together with the deformation shape in a ZnO nanowire (grown along the c-axis with a length of 1200 nm and a hexagonal side length of 100 nm) without doping (b) without strain, under (c) a stretching force of 85 nN, and (d) a compressive force of 85 nN. Two ends of the nanowire are assumed to be surrounded by electrodes for a length of 100 nm. Reproduced from ref. 29 with permission from AIP Publishing, copyright 2009.
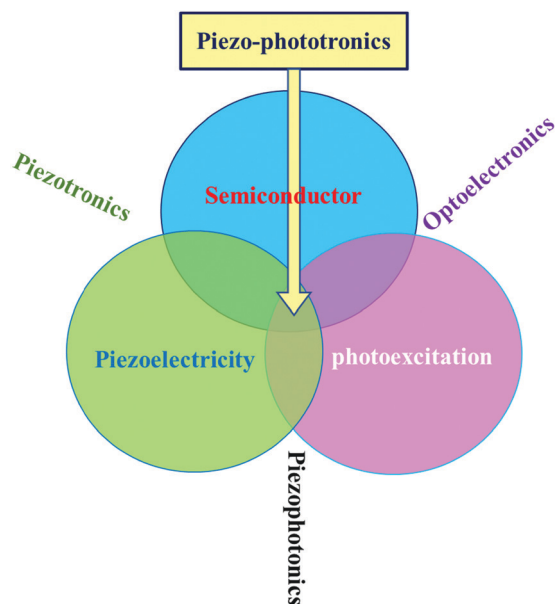
Fig. 3 Schematic diagram showing the three-way coupling among piezoelectric, photoexcitation and semiconducting properties, which is the basis of piezotronics (piezoelectric–semiconductor coupling), piezophotonics (piezoelectric–photoexcitation coupling), optoelectronics, and piezo-phototronics (piezoelectric–semiconductor–photoexcitation coupling). The core of these couplings relies on the piezoelectric potential created by piezoelectric materials. Reproduced from ref. 30 with permission from Elsevier Ltd, copyright 2010.
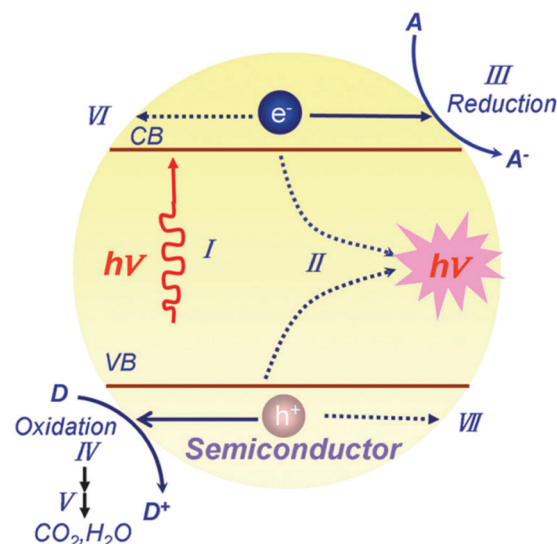

Fig. 4 Schematic illustration of the principle of semiconductor photocatalysis: (I) the formation of charge carriers by a photon, (II) the charge carrier recombination to liberate heat, the initiation of (III) a reductive pathway by a conduction-band electron and (IV) an oxidative pathway by a valence-band hole, (V) the further thermal and photocatalytic reactions to yield mineralization products, the trapping of (VI) a conduction-band electron in a dangling surficial bond and (VII) a valence-band hole at the surface of the semiconductor. Reproduced from ref. 39 with permission from The Royal Society of Chemistry, copyright 2014.

performance of many optoelectronic materials and devices.[31] The core physics of the piezo-phototronic effect relies on the use of piezoelectric potential to modulate the band structure at the contact or junction of devices to effectively tune/control charge generation, separation/recombination, and transport processes. In detail, under strain, piezoelectric polarization charges and the corresponding piezoelectric potentials are induced at the surfaces and interfaces of the material. This altered piezoelectric potential could sufficiently modify the energy band structure at the heterojunction and thus dictate the carrier behavior in optoelectronic processes. Therefore, high-performance optoelectronic materials and devices (such as solar cells, photocatalysts, photodetectors, and LEDs) can be achieved *via* the piezo-phototronic effect. The detailed mechanisms of how the piezo-phototronic effect modulates the properties of optoelectronic materials and devices will be described in the following sections.

3. The piezo-phototronic effect enhanced photocatalysis

3.1 Fundamental principles and key challenges of photocatalysis

Semiconductor photocatalysts hold great promise in harnessing solar power to accomplish many environmentally-sustainable goals, including splitting water into hydrogen, converting carbon dioxide, and degrading organic pollutants.[32–35] Through several

decades of unremitting efforts, researchers have achieved deep insights into the fundamental principles of photocatalysis.[36,37] During a typical photocatalytic reaction process, light irradiation of the photocatalyst promotes electrons from the valence band to the conduction band (simultaneously leaving holes in the valence band, Fig. 4I).[38,39] Some of the photoinduced electrons and holes then move to the surface of the photocatalyst and participate in reduction and oxidation reactions, respectively (Fig. 4III–V). Additionally, electrons and holes can get trapped in metastable surface states, where they are unable to participate in redox reactions (Fig. 4VI and VII). It should be pointed out that the majority of photogenerated carriers recombine or dissipate in the form of heat or light before participating in photocatalytic reactions (Fig. 4II), which seriously restricts solar light conversion efficiency (or quantum yield).[40]

Recombination and capture of photoinduced carriers in bulk and on the surface of semiconductors is a significant hindrance during photocatalysis. To overcome this troublesome barrier, many modification strategies have been developed to improve photocatalytic performance by promoting the separation of photogenerated carriers. Building an internal electric field within photocatalysts (such as developing ferroelectric semiconductor photocatalysts or preparing ferroelectric–photocatalytic composites) is regarded as a particularly promising strategy because of its ability to create a driving force to accelerate electrons and holes in opposite directions.[41–45] Unfortunately, these kinds of internal electric fields created in ferroelectric photocatalysts or ferroelectric–photocatalytic composites are static and easily saturated by photogenerated

charges, free charge carriers, and ions by the electrostatic screening effect.[46] Once saturated, carrier separation is no longer enhanced and photocatalytic properties return to their original state.

3.2 Theory of the piezo-phototronic effect on improving the photocatalytic performance

Utilizing piezo-phototronic catalysts under strain and light illumination provides a simple yet robust method to overcome the above stated deficiency of static internal electric field.[47] The piezo-induced internal electric field and degree of energy band bending of photocatalysts can be tuned by adjusting the applied strain (direction and strength) and thus serve as a dynamic driving force to sustainably promote the bulk charge separation. Additionally, the piezo-induced internal electric field can modulate the surface/interface energy band structure of the photocatalyst, which will impact the carrier transfer behavior as well as the corresponding photocatalytic performance.[25]

To elucidate the detailed mechanisms of how the piezo-phototronic effect works on photocatalytic reactions, an n-type piezoelectric semiconductor is taken as an example (Fig. 5).[25] When it is immersed in electrolyte solution (Fig. 5a and b), the photogenerated charges will transfer to the electrolyte solution through the interface between the semiconductor and electrolyte solution. As a result, the surface energy band of the photocatalyst will bend upward, which will impede the transfer of photogenerated electrons to the photocatalyst surface for taking part in the photocatalytic reduction reaction, but accelerate the movement of photogenerated holes towards the photocatalyst surface and then participate in the photocatalytic oxidation reaction. When this n-type piezoelectric semiconductor photocatalyst was positively polarized (polarized under an applied electric field with the same direction as that of the spontaneous polarization of the piezoelectric photocatalyst), the surface energy band will bend downward and therefore the surface would be at a higher potential than before (Fig. 5c). As a consequence, the migration of photogenerated electrons towards the electrolyte would be promoted, whereas the reductive potential is reduced slightly. On the contrary, in the presence of negative polarization (the applied polarization direction is opposite to the spontaneous polarization direction of the piezoelectric photocatalyst), a potential is achieved across the domain and the surface energy band bends upwards, leading to a relatively lower potential compared with before (Fig. 5d). Because of the increased energy barrier, the migration behavior of photoexcited electrons is restricted, but the transfer kinetics of photogenerated holes is accelerated with the slightly reduced oxidative potential. Consequently, the photocatalytic process of piezoelectric semiconductor photocatalysts can be modulated.

In the case of piezoelectric–photocatalyst hybrids (consisting of one photocatalyst and one piezoelectric material with or without photocatalytic properties), the TiO_2/ZnO heterojunction hybrid photocatalyst (TiO_2 is the photocatalyst and ZnO possesses piezoelectric and photocatalytic properties) is taken as a specific example here. When the sample is strained, piezoelectric potential will be generated on the surface of the piezoelectric material (Fig. 5e).[42] Under sole light illumination, electron–hole pairs are excited in the piezoelectric photocatalyst ZnO monocrystalline nanoplatelets and the photocatalyst TiO_2 nanoparticles, and the random motion of charges would lead to a high carrier recombination rate (Fig. 4f) due to the relatively flat band structure without enough driving forces to separate the electrons and holes. When the hybrid is under strain and negative piezoelectric polarization charges are generated on the interface of ZnO and TiO_2, these immobile ionic charges will deplete free electrons near the interface and result in upward band bending (Fig. 5g). Hence, the photoexcited carriers are efficiently separated driven by this introduced strong local electric field across the interface and thus the carrier recombination rate is suppressed. When positive polarization charges are introduced at the interface, free electrons will be attracted to the interface of ZnO and TiO_2, resulting in downward band bending at the contact interface (Fig. 5h). In this case, the local electric field will promote the migration of electrons from the conduction band of ZnO towards TiO_2 and holes from the valence band of TiO_2 to ZnO; therefore, the opposite carrier transfer direction is achieved and the charge separation efficiency is boosted.

3.3 Photocatalytic materials and composites with the piezo-phototronic effect

Due to the seminal impact of the piezo-phototronic effect on photocatalysis, numerous photocatalysts with the piezo-phototronic effect have been reported (some of them are summarized in Table 2), all of which can be divided into three types according to the structure and properties of materials, piezoelectric semiconductor photocatalysts (*e.g.*, ZnO, $ZnSnO_3$, CdS, MoS_2), inorganic-piezoelectric-based photocatalyst composites (such as ZnO- and $BaTiO_3$-based photocatalysts) and organic-piezoelectric-based photocatalyst hybrids (for example, polyvinylidene fluoride (PVDF)-based photocatalysts).[48–54] Some representative photocatalysts will be exemplified in the following sections to unravel the robust role of the piezo-phototronic effect in improving photocatalysis.

3.3.1 Piezoelectric semiconductor photocatalysts. Piezoelectric semiconductor photocatalysts are materials that exhibit both piezoelectric and photocatalytic properties. In the presence of light irradiation and mechanical energy, piezoelectric potential will be introduced and distributed on the surface of the piezoelectric semiconductor, and electrons as well as holes will be excited at the same time. In this case, the piezoelectric and photocatalytic properties of piezoelectric semiconductors will couple into one internal physical–chemical process. Significantly, the induced piezoelectric potential will efficiently drive the photogenerated electrons and holes to move toward the positive and negative potential surfaces of the semiconductor, respectively (in this process, the charge separation rate is increased and the photocatalytic efficiency is consequently improved).

ZnO, possessing both piezoelectric and photocatalytic properties, was selected as an example of a piezoelectric semiconductor photocatalyst by Xue and co-authors to investigate
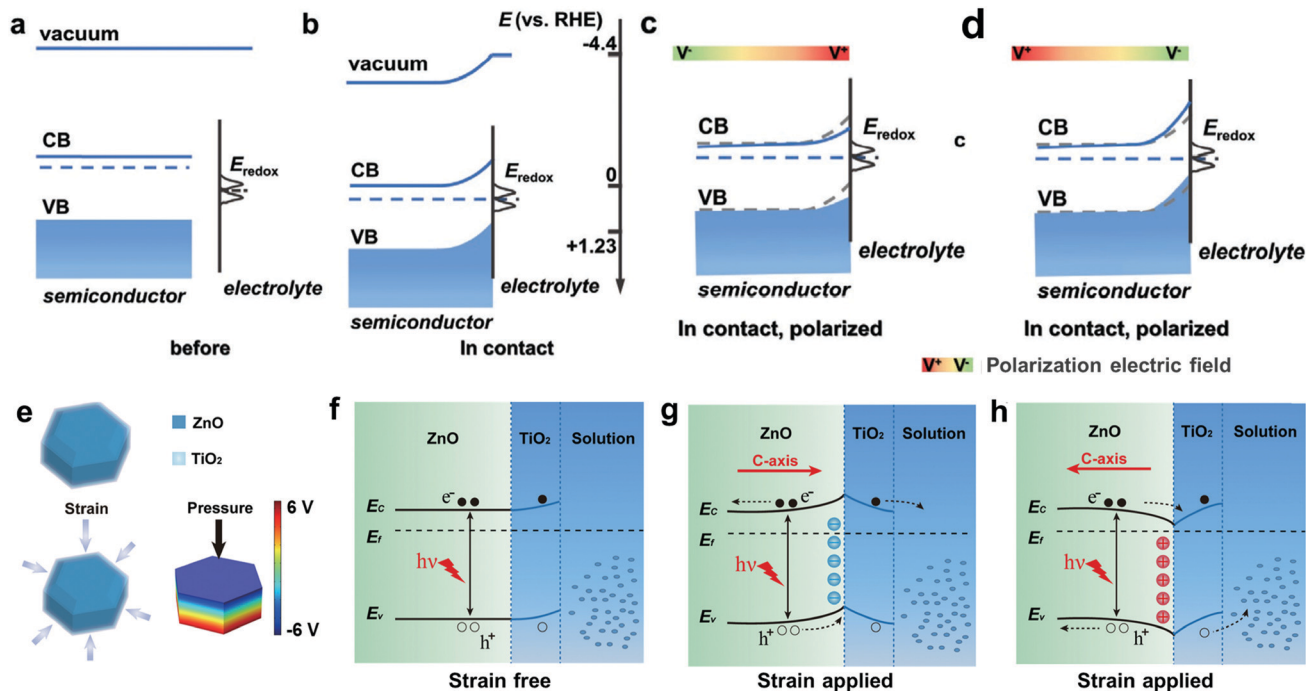
Fig. 5 Band structure diagrams of the piezoelectric semiconductor/electrolyte interface based on an n-type semiconductor in photocatalysis: (a) before and (b) after the contact, and further under (c) positive or (d) negative polarizations. Reproduced from ref. 25 with permission from WILEY-VCH Verlag GmbH & Co. KGaA, Weinheim, copyright 2020. (e) 3D schematic demonstration of ZnO/TiO$_2$ hybrids without (top) and with strain (bottom left). Piezo-potential distributions in a ZnO nanoplatelet (hexagonal edge: 2 µm, height: 1.5 µm) under an axial pressure of 10 MPa, simulated by a finite-element analysis method (COMSOL) (bottom right). Schematic band diagrams of the ZnO/TiO$_2$ heterojunction (f) without and (g and h) with strain. The gray dashed line and blue solid line in (e–h) represent the initial band edge without strain and the band edge under strain, respectively. Reproduced from ref. 42 with permission from American Chemical Society, copyright 2016.

the piezo-phototronic effect enhanced photocatalytic performance.[55] In their work, ZnO nanowires were vertically aligned on carbon fibers (CFs) through a seed-assisted hydrothermal method, and several bundles of ZnO/CFs were woven together, forming multi-fiber devices (Fig. 6a). As discussed above, using piezoelectric polarization (introducing piezoelectric potential) on the surface/interface of photocatalysts to govern the separation and transfer behavior of photoexcited charges is key to utilizing the piezo-phototronic effect to enhance photocatalysis, and a proper applied force is required to ensure that an adequate piezoelectric potential is continuously present for photocatalysts that use the piezo-phototronic effect. Therefore, an external mechanical brushing/sliding force was employed as the driving force to extrude ZnO nanowires outward radially and consequently bend ZnO wires. Under light irradiation, the negative and positive piezoelectric potentials distributed on the compressive and tensile strain regions were found to promote the transfer of photoinduced holes and electrons towards the negative and positive potential surfaces of ZnO, respectively (Fig. 6b). As a result, the carrier recombination rate was suppressed and the photocatalytic performance was enhanced (the photocatalytic degradation efficiency of methyl blue (MB) was increased by about 30%).

In addition, ultrasonication was used to drive the generation of a piezoelectric field over the piezo-photocatalytic activity of NaNbO$_3$ (exhibiting n-type conductivity and ferroelectric characteristics at room temperature) in Khare's group and a

much larger (~115%) enhancement in the photodegradation rate of MB was obtained under periodic ultrasonic vibration.[52] It is worth noting that ultrasonication could play two roles during photocatalysis. On the one hand, it can impart the desorption of products and therefore refresh the active sites of photocatalysts in a timely manner. On the other hand, it may break large-molecule dyes into fragments and thus facilitate their degradation. The low conversion rate (less than 20%) of MB under ultrasonic vibration in the dark demonstrated that the second role of ultrasonication was limited. The increase in photocatalytic activity was ascribed primarily to the promoted mass transfer (refreshing photocatalytic active sites) and ultrasonic-vibration-driven piezoelectric potential in NaNbO$_3$, which made photoexcited electrons and holes transfer to opposite directions and thus reduced the charge recombination (Fig. 6c). Similarly, higher photocatalytic degradation efficiencies were also realized for BaZnO$_2$ (the conversion capability of MB was boosted by about 15%) and BaTiO$_3$ (the degradation rate of methyl orange (MO) was increased more than 50%) under light illumination and ultrasonic vibration compared with that detected under light irradiation alone.[56,57] Moreover, as shown in Fig. 6d, the conversion efficiency of MB was higher for ZnSnO$_3$ nanowires grown on glass with ultrasonic vibration compared with the degradation rate of MB characterized under other conditions, which indicated that the Schottky barrier could couple with piezoelectric potential to further improve

Table 2 Summary of photocatalysts and composites with the piezo-phototronic effect and their corresponding performance

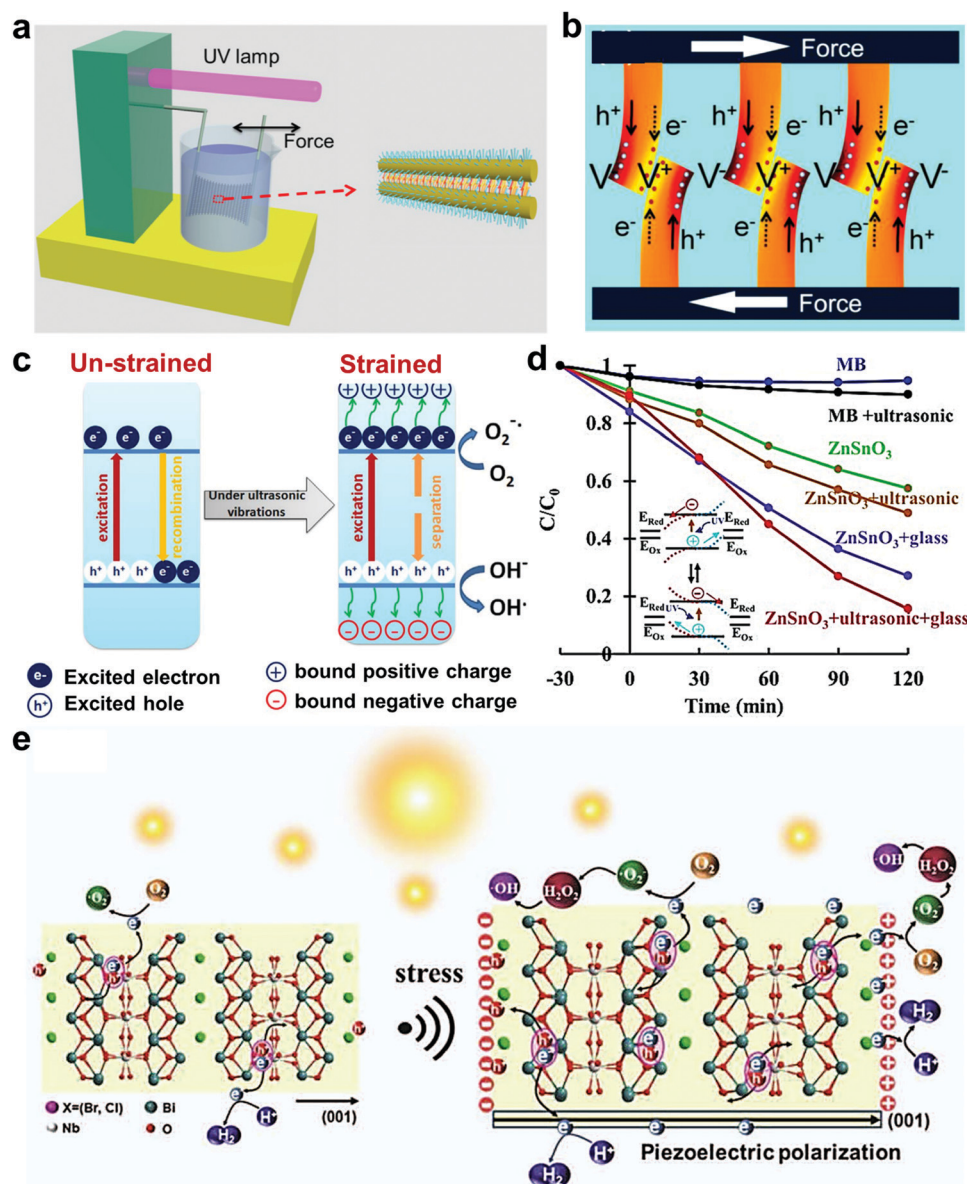| Materials	Applications	Applied forces	Performance			Enhancement mechanisms	Ref.
			Only piezoelectric potential	No piezoelectric potential	Light + piezoelectric potential		
ZnO NW/CFs	200 mg photocatalyst degraded 5 mg L⁻¹ 100 mL MB in 120 min	Mechanical force	—	64%	96%	Piezo-phototronic effect	55
NaNbO₃	100 mg photocatalyst degraded 250 mL of $(1 \times 10^{-5}$ M) MB in 180 min	Ultrasonication	15%	50%	75%	Piezo-phototronic effect	52
BaTiO₃ NW	The prepared sample degraded 100 mL of 5 mg L⁻¹ MO in 80 min	Ultrasonication	76%	43%	98%	Piezo-phototronic effect	57
ZnO nanorods	20 mg ZnO converted CO_2 into CH_4	Ultrasonication	—	0.0391 µL h⁻¹	0.112 µL h⁻¹	Piezo-phototronic effect	61
CdS nanosheets	10 mg CdS in 20 mL aqueous solution containing 0.1 M Na_2S and 0.1 M Na_2SO_3 to produce H_2	Ultrasonication	144 µL h⁻¹	168 µL h⁻¹	633 µL h⁻¹	Piezo-phototronic effect	62
ZnSnO₃ + glass	2.4 cm × 2.4 cm sample degraded 10 mL 4 ppm MB in 120 min	Ultrasonication	50%	75%	85%	Coupling with the Schottky barrier	58
Ag/ZnO nanotetrapods	200 mg photocatalyst degraded 100 mL 5 mg L⁻¹ MO in 25 min	Ultrasonication	~0	87%	~100%	Coupling with the plasmonic effect	64
Al/BaTiO₃ foam	25.4 mm × 10 mm foam submerged in 16 mL water and 4 mL methanol to produce H_2	Mechanical vibration	15 µmol h⁻¹ cm⁻²	327 µmol h⁻¹ cm⁻²	657 µmol h⁻¹ cm⁻²	Coupling with the plasmonic effect	65
Ag–NaNbO₃	100 mg photocatalyst degraded 250 mL MB in 180 min	Ultrasonication	0.0002 min⁻¹ (NaNbO₃) 0.0004 min⁻¹ (Ag–NaNbO₃)	0.001 min⁻¹ (NaNbO₃) 0.002 min⁻¹ (Ag–NaNbO₃)	0.004 min⁻¹ (NaNbO₃) 0.011 min⁻¹ (Ag–NaNbO₃)	Coupling with the plasmonic effect	66
Ag₂O–BaTiO₃	20 mg photocatalyst degraded 20 mL 15 mg L⁻¹ RhB in 60 min	Ultrasonication	10%	65%	90%	Piezo-phototronic effect	67
FeS/ZnO nanoarrays	~100 mg FeS/ZnO degraded 100 mL 5 mg L⁻¹ MB in 50 min	Ultrasonication	16%	75%	97%	Piezo-phototronic effect	68
ZnO–Ag₈S hybrid	1 cm × 1 cm sample degraded 100 mL of 1×10^{-3} M RhB in 120 min	Ultrasonication	1%	36%	93%	Piezo-phototronic effect	70
PMN-PT@TiO₂	50 mg photocatalyst degraded 50 mL 12 mg L⁻¹ RhB in 210 min	Ultrasonication	18%	50%	99%	Piezo-phototronic effect	72
PDMS–PMN-PT@TiO₂	A piece of the 2.5 cm × 7.6 cm prepared film degraded 90 mL of 12 mg L⁻¹ RhB in 4 h	Ultrasonication	20%	35%	90%	Piezo-phototronic effect	73
MoS₂@Ag₂O	20 mg photocatalyst degraded 50 mL of 20 mg L⁻¹ MO in 30 min	Ultrasonication	~25%	~80%	95%	Piezo-phototronic effect	74
PVDF–TiO₂ film	A piece of the 2.5 cm × 7.6 cm prepared film degraded 100 mL of 12 mg L⁻¹ RhB in 4 h	Ultrasonication	~20%	38%	95%	Piezo-phototronic effect	79
BQD@ZnO-RA on a Zn foil film	The photocatalytic film degraded 150 mL of 50 ppm formaldehyde	Wind	—	~50%	~80%	Piezo-phototronic effect	71
TiO₂@rGO-F/PVDF–HFP film	The 2 cm × 5 cm film degraded 50 mL of 5×10^{-5} mol L⁻¹ MO in 60 min	Water flow	—	30%	99%	Piezo-phototronic effect	80
BiOI@rGO-F/PVDF–HFP film	The 2 cm × 1 cm film sample degraded 30 mL of 2.5×10^{-5} mol L⁻¹ MO in 24 h	Water flow	—	~1%	21%	Piezo-phototronic effect	81
CdS@rGO-F/PVDF–HFP film	The 2 cm × 2 cm prepared film deposited with Pt in 100 mL lactic acid (10 vol%) to produce H_2	Water flow	—	2.5 mmol h⁻¹ g⁻¹	10.4 mmol h⁻¹ g⁻¹		82
ZnO@PVDF film	The prepared film degraded 100 mL 12 mg L⁻¹ RhB in 100 min	Water flow	—	~60%	~95%	Piezo-phototronic effect	81
PVDF/g-C₃N₄ helical microfiber	The prepared fiber degraded 5 mL 12 mg L⁻¹ RhB in 75 min	Water flow	—	73%	96%	Piezo-phototronic effect	82
ZnO/P3U7 cilia array	50 mL 20 mg L⁻¹ tetracycline	Water flow	—	55%	75%	Piezo-phototronic effect	83

Fig. 6 Schematic diagram of (a) the prepared ZnO nanowire/CF woven multi-fiber device immersed in methyl blue (MB) solution under ultraviolet (UV) irradiation and periodically applied force, and (b) the relative sliding between neighboring ZnO nanowires and the bending of ZnO nanowires with positive and negative piezoelectric potentials across their width under the periodically applied force. Electrons and holes migrate to the surface in opposite directions. Reproduced from ref. 55 with permission from Elsevier Ltd, copyright 2015. (c) Schematic diagram of photogenerated charge separation in the unstrained and strained $NaNbO_3$ nanorods. Reproduced from ref. 52 with permission from Elsevier Ltd, copyright 2017. (d) Photocatalytic degradation activities of MB over $Zn_{1-x}SnO_3$. The inset shows a diagram of energy band evolution under ultrasonic vibration. Reproduced from ref. 58 with permission from American Ceramic Society, copyright 2016. (e) The schematic diagram of the mechanism of reactive oxygen species and H_2 evolution over Bi_4NbO_8X (X = Cl, Br) under light irradiation and simultaneous light and ultrasonic irradiation. Reproduced from ref. 63 with permission from WILEY-VCH Verlag GmbH & Co. KGaA, Weinheim, copyright 2019.

photocatalytic degradation efficiency based on the piezo-phototronic effect.[58] In another study, the increased photo-catalytic degradation rates of Rhodamine B (RhB) over $Bi_4Ti_3O_{12}$ nanostructures and $Bi_{0.5}Na_{0.5}TiO_3$ nanorods were also observed under both ultrasonic vibration and light illumination as compared to that detected under one of ultrasonication and light irradiation.[59,60] This further suggested the potential of the piezo-phototronic effect in enhancing photocatalytic efficiency for various kinds of piezoelectric semiconductors.

The piezo-phototronic effect has also been found to influence photocatalytic CO_2 conversion, which was studied and verified over ZnO nanorods in Liu's group.[61] Their work indicated that, with the help of ultrasonic-vibration-induced piezo-electric potential, CO_2 tended to be converted to CH_4 rather than CO, and the production selectivity rate of CH_4 was doubled. This was ascribed to the fact that eight and two electrons were required for the formation of each CH_4 and CO molecule, respectively (the production of CH_4 needed more

electrons than that of CO). In the presence of ultrasonic-vibration-enabled piezoelectric potential, many more electrons and holes would be compelled to migrate in opposite directions across ZnO and distribute in different locals to take part in redox reactions, increasing the electron density on the ZnO surface and thus improving the selective generation of CH_4. Moreover, to further explore the role of the piezo-phototronic effect in photocatalytic water splitting properties, Liu's group synthesized CdS nanosheets that possessed both photocatalytic and piezoelectric properties and carried out hydrogen evolution experiments under visible light irradiation, ultrasonic vibration and their simultaneous superposition, respectively. The results indicated that the hydrogen evolution yield obtained under the synchronous irradiation of light and ultrasonication was more than twice the superposition of that detected under light irradiation and vibration alone.[62] The notable improvement in photocatalytic hydrogen production was ascribed to the promoted charge separation rate caused by the piezoelectric potential of CdS. Recently, the piezo-phototronic effect in Bi_4NbO_8X (X = Cl, Br) polar single crystals was reported to boost photocatalytic hydrogen evolution activity by Ma and co-authors (Fig. 6e).[63] The enhancement was attributed to the ultrasonic-vibration-imparted polarized electric field and the corresponding band bending that facilitated directional separation of charge carriers.

To further improve the photocatalytic activity, the surface plasmon resonance effect coupled with the piezo-phototronic effect was introduced into photocatalysts. Ag/ZnO nanotetrapods (Ag nanoparticles randomly grew on the surface of ZnO nanotetrapods) were synthesized by Zhang et al.[64] As depicted in Fig. 7, under solar light illumination, UV light was absorbed by ZnO to generate electrons and an equal number of holes, and visible light (which cannot excite the generation of electrons and holes of ZnO due to its low photon energy) was captured by Ag nanoparticles through local surface plasmon resonance to form electrons and Ag^+. These generated electrons were then observed to transfer

Fig. 8 Schematic illustration of (a) charge carrier generation in a Ag_2O nanoparticle when excited by a photon and (b) the separation of electrons and holes in Ag_2O nanoparticles attached to the two opposite surfaces of a $BaTiO_3$ nanocube that has opposite polarization charges due to the piezoelectric effect and the corresponding tilting in the bands. The solid line is the bands with the presence of spontaneous polarization charges at the two surfaces of the $BaTiO_3$ nanocube, and the dashed line represents the decrease of the piezoelectric polarization with mechanical strain. Reproduced from ref. 67 with permission from American Chemical Society, copyright 2015.

from Ag towards the conduction band of ZnO. Moreover, the lower work function of Ag compared with ZnO led to ohmic contact at the Ag/ZnO interface. As a consequence, electrons tended to transfer from Ag to ZnO and holes tended to transfer from ZnO to Ag. In this end, the light absorption efficiency was broadened from the UV to visible light region, and the carrier separation rate was promoted. In addition, with the assistance of ultrasonic vibration, negative and positive piezoelectric potentials were created across the tentacles, which further promoted the transfer of electrons and holes to positive and negative piezo-potential surfaces, respectively. With the coupling effect of surface plasmon resonance and the piezo-phototronic effect, the organic dyes MO, MB, phenol red and RhB could be almost completely degraded by Ag/ZnO in 25 min. The plasmon resonance of non-noble metal Al was also coupled with the piezo-phototronic effect to synergistically enhance the photocatalytic hydrogen evolution efficiency of $Al/BaTiO_3$ (Al nanoparticles were loaded on the surface of a $BaTiO_3$ nanocavity), and more than 50% higher hydrogen generation activity was obtained under light illumination and mechanical vibration.[65] Ag nanoparticle decorated $NaNbO_3$ nanorods ($Ag–NaNbO_3$) were synthesized by Khare's group and exhibited a nearly 10-fold enhancement in the degradation of organic methylene blue under ultrasonic vibration and light irradiation in comparison with bare $NaNbO_3$, thanks to the combined plasmonic and piezo-phototronic effect.[66]

These previous studies verified that the piezo-phototronic effect can be used to boost photocatalytic degradation efficiencies, photocatalytic hydrogen evolution rates, and carbon dioxide conversion activities. Therefore, the photocatalytic quantum yield can be greatly improved by incorporating the piezo-phototronic
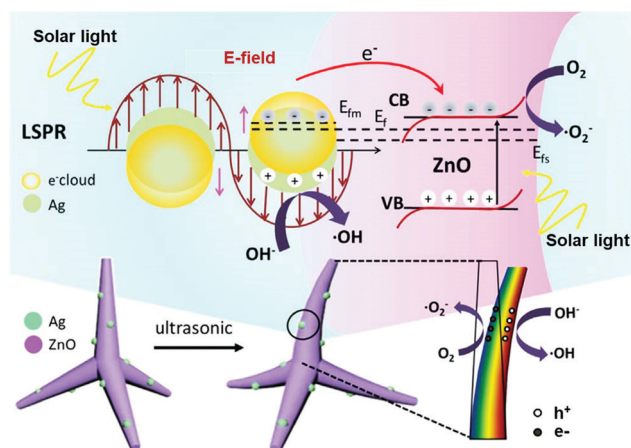

Fig. 7 Schematic diagram of the coupling effect of local surface plasmon resonance and the piezo-phototronic effect on photocatalytic degradation activity over Ag/ZnO nanotetrapods. Reproduced from ref. 64 with permission from Elsevier Ltd, copyright 2016.
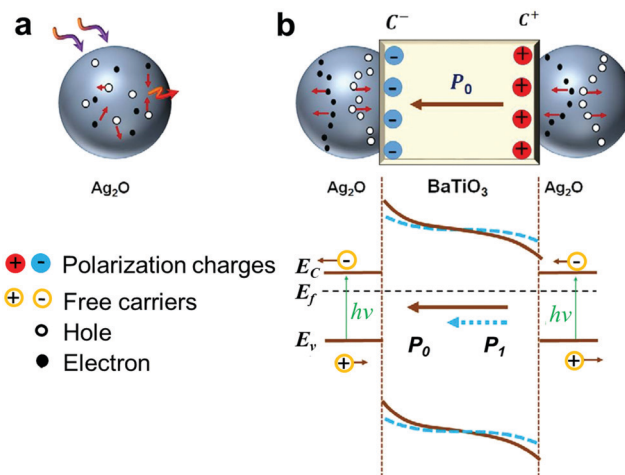
effect, which is beneficial for the practical application of semiconductor photocatalysts in energy and environmental fields. Importantly, the synergistic effect of local surface plasmon resonance and the piezo-phototronic effect can enable a much higher photocatalytic performance.

3.3.2 Inorganic-piezoelectric/photocatalyst composites. Although piezoelectric photocatalysts have many advantages, the limited number of piezoelectric semiconductors severely restricts their potential for widespread photocatalytic applications. Therefore, a combination of inorganic piezoelectric materials exhibiting a high electromechanical coupling coefficient and photocatalysts possessing high photocatalytic activity was proposed to form high performance inorganic-piezoelectric–photocatalyst composites. It is worth noting that it is crucial that close bonding occurs at the interface/junction between the piezoelectric material and semiconductor photocatalyst to enable the positive influence of piezoelectric potential on the motion of photoinduced carriers.

To exert the piezo-phototronic effect on photocatalysis over a piezoelectric–photocatalytic composite, Ag_2O (metal-oxide-semiconductor) was deposited on the surface of $BaTiO_3$ (a typical piezoelectric material) to form a Ag_2O–$BaTiO_3$ hybrid photocatalyst.[67] When tested alone, Ag_2O displayed low photocatalytic activity due to a high recombination rate of photogenerated carriers (Fig. 8a). When integrated into composite Ag_2O–$BaTiO_3$ hybrids, however, an electric field and spontaneous polarization were observed inside $BaTiO_3$ (due to its ferroelectric nature), as shown in Fig. 8b (solid line). This polar charge-created field was found to serve as a driving force to attract the holes and electrons of Ag_2O, distributing on the left-hand and right-hand side surfaces to move to the C^- (negative polarization charges distributed) and C^+ (positive polarization charges distributed) sides of $BaTiO_3$, respectively. Although the internal electric field of $BaTiO_3$ endowed the Ag_2O–$BaTiO_3$ hybrid with a higher photocatalytic activity compared with Ag_2O, this polarized ferroelectric field was static and might be screened by photogenerated and free charge carriers, diminishing charge separation. To remedy this, ultrasonic wave vibration was introduced during the photocatalytic reaction, which was shown to alter the internal electric field in the Ag_2O–$BaTiO_3$ composite and thus boost its photocatalytic performance. In detail, when a compressive stress was applied on $BaTiO_3$, the polarization potential was diminished ($P_1 < P_0$), and most of the photogenerated electrons and holes attached on the C^+ and C^- surfaces of $BaTiO_3$ were abruptly discharged (Fig. 8b, dashed line). Conversely, when the strain disappeared, many more photoexcited electrons and holes transferred to the C^+ and C^- surfaces of $BaTiO_3$, respectively, corresponding to a recharge process. This process mitigated screening of the piezoelectric field and sustainably enhanced the photocatalytic performance of the Ag_2O–$BaTiO_3$ composite. Notably, the photocatalytic degradation efficiency of organic pollution over Ag_2O–$BaTiO_3$ with ultrasonic vibration was about 20% higher than that of Ag_2O and 25% higher than that of Ag_2O–$BaTiO_3$ with physical stirring. These increases demonstrated the positive influence of the construction of piezoelectric–photocatalytic composites and the significant

effect of ultrasonication in photocatalysis. Importantly, this work compared the degradation rates over P25, Ag_2O, $BaTiO_3$, the Ag_2O–$BaTiO_3$ hybrid and the Ag_2O–$BaTiO_3$ physical mixture under different conditions (light with physical stirring, ultrasonic vibration in the dark and ultrasonic vibration with light irradiation), suggesting that the ultrasonication effect on refreshing active sites and breaking large-molecule dyes was limited and the dynamic modulation of the ultrasonication-induced piezo-phototronic effect played a predominant role in modulating the photoexcited carrier motion behavior and photocatalytic performance. Moreover, in this work, the photocatalytic activities of different piezoelectric-based photocatalyst hybrids in the absence and presence of ultrasonication were studied, and it was observed that a higher piezoelectric potential output is more beneficial for improving the photocatalytic performance.

In addition to $BaTiO_3$, the piezoelectric semiconductor ZnO has also been combined with other photocatalysts to construct composites with the piezo-phototronic effect. For example, FeS nanoparticles were coated on the surface of ZnO nanoarrays.[68] Sole ZnO nanoarrays under solar light irradiation were observed to degrade only 4% of methylene blue in 50 min and 16% when ultrasonic vibration was introduced. The increase demonstrated the positive effect that ultrasonic-induced piezoelectric potential can have on photocatalysis. Interestingly, the FeS/ZnO composites were found to degrade 75% of methylene blue within 50 min under solar light illumination, and the enhancement was attributed to the higher light absorption rate of FeS/ZnO (visible light can be absorbed by FeS) compared with ZnO. Moreover, under simultaneous solar irradiation and ultrasonic vibration, the conversion rate of methylene blue in 50 min by FeS/ZnO was further boosted to about 97%. The significantly higher photocatalytic degradation activity of FeS/ZnO (compared to pure ZnO) further highlighted how combining piezoelectric semiconductors and narrower energy band gap photocatalysts stood as a promising method to improve photocatalytic performance. Similarly, CuS/ZnO heterostructure nanowire arrays showed about 40% higher degradation efficiency under solar light irradiation and ultrasonic vibration in comparison with that detected under solar light illumination alone.[69] In addition, it was reported that the photodegradation efficiency of RhB by the ZnO–Ag_8S hybrid exhibited a 57% degradation efficiency increase with the help of an ultrasonic-vibration-imparted piezoelectric field when compared with ZnO.[70]

Moreover, as displayed in Fig. 9a and b, the photocatalyst $BiVO_4$ quantum dots were loaded on ZnO nanorod arrays (ZnO-RA) on Zn foil, which was attached onto a flexible polyethylene terephthalate (PET) film (the obtained sample was named BQD@ZnO-RA).[71] In this work, the photocatalytic activities of the prepared composite films (fixed on the blades of a windmill) were characterized by their ability to degrade formaldehyde in a closed quartz reactor. A mini electric fan was employed to blow the windmill with a wind speed of about 2.3 m s^{-1} to deform the constructed photocatalyst BQD@ZnO-RA and thus a piezoelectric field was introduced inside ZnO (Fig. 9b). The degradation efficiency of formaldehyde over BQD@ZnO-RA was about 30% higher than that detected without piezo-potential generation in
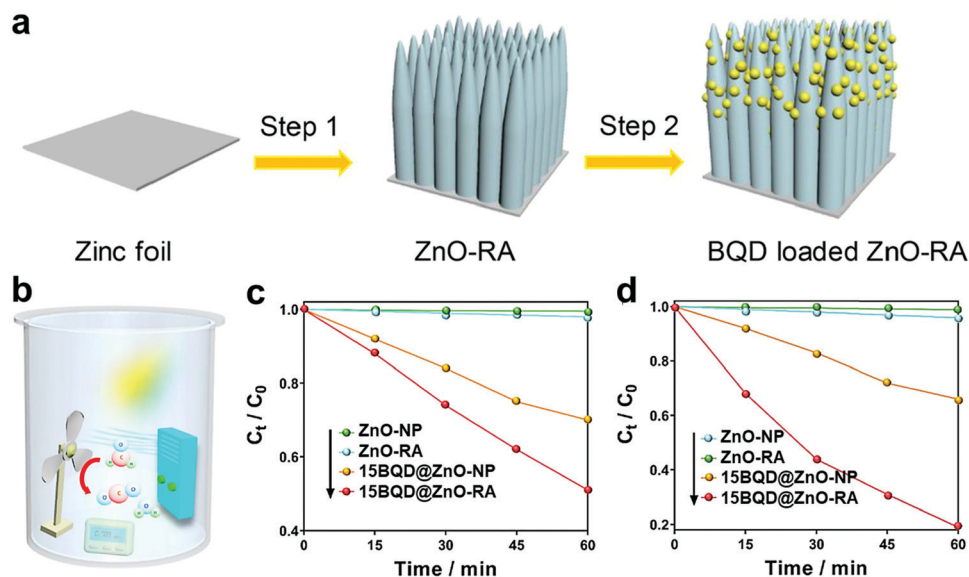
Fig. 9 Schematic diagram of (a) the preparation of BiVO$_4$ quantum dot loaded ZnO nanorod arrays and (b) the home-built installation for formaldehyde degradation. The degradation of formaldehyde in the case (c) without and (d) with the windmill being blown directly. Reproduced from ref. 71 with permission from Elsevier Ltd, copyright 2020.

the same case (Fig. 9c and d). Importantly, the COMSOL simulation, voltage output, and time-resolved surface photo-voltage characterization results corroborated that the improved photocatalytic activity originated from the promoted charge separation and accelerated carrier transfer rate driven by the piezoelectric potential of ZnO. This work indicated that the photocatalytic activity of semiconductors (such as BiVO$_4$) with narrow bandgap and poor carrier separation characteristics can be greatly boosted by the piezo-phototronic effect. Additionally, this work implied that a piezoelectric field over inorganic piezoelectric–photocatalytic composites could be introduced *via* various mechanical energy forms in addition to ultrasonic vibration, such as natural wind, which opened new avenues to introduce the piezo-phototronic effect and broadened its practical applications.

By now, some photocatalysts and piezoelectrics (with or without photocatalytic properties) have been combined with photocatalysts to construct inorganic piezoelectric–photocatalytic composites, such as ZnO, BaTiO$_3$, PMN-PT and MoS$_2$.[72–74] Previous research results indicated that the construction of inorganic piezoelectric–photocatalytic composites would make the role of the piezo-phototronic effect in promoting photocatalysis more efficiently if visible-light responsible photocatalysts were introduced for broadening the light absorption region.[75] Additionally, the piezoelectric properties of photocatalysts would no longer be a requirement to realize the piezo-phototronic effect when piezoelectric–photocatalyst hybrids were used, and because of this flexibility, the piezo-phototronic effect can be used to enhance photocatalytic performance in more practical applications. Therefore, designing and developing novel photocatalytic composites with the piezo-phototronic effect are greatly needed and welcomed.

3.3.3 Organic-piezoelectric-based photocatalyst hybrids. As mentioned above, some inorganic piezoelectric materials

that possess a high electromechanical coupling coefficient have been combined with photocatalysts to create highly active photo-catalytic hybrids *via* the piezo-phototronic effect. Although organic piezoelectric materials possess a relatively lower piezo-electric constant than their inorganic counterpart, organic piezo-electrics exhibit excellent flexibility, which enables facile defor-mation that can generate considerable piezoelectric potential under mild forces.[76–78] The ability to easily deform organic piezoelectrics stands in sharp contrast to inorganic piezoelec-trics because their hardness is dependent on ultrasonic vibration to generate a piezoelectric field. Ultrasonic vibration is non-ideal for widespread applications due to its massive energy consump-tion and serious noise pollution (harmful to human hearing). It is also difficult to generate ultrasound throughout a large-scale reactor, which further impedes its practical application. In this regard, organic piezoelectric substrates (*i.e.*, PVDF and its copolymers) have been integrated with photocatalysts to form flexible organic-piezoelectric-based photocatalyst hybrids to introduce a piezoelectric field with a low-density natural energy input and to boost the photocatalytic activity.[79,80]

Poly(vinylidene fluoride-*co*-hexafluoropropylene) (PVDF–HFP), a typical organic piezoelectric material was combined with 4-azidotetrafluorobenzoic acid-modified graphene (rGO-F) and various photocatalysts to form a flexible porous composite film.[80] In this work, TiO$_2$, BiOI and CdS were selected as the representatives of classical UV-responsive, narrow band gap, visible-light-active, and hydrogen evolution photocatalysts to combine with the rGO-F/PVDF–HFP film substrate, respectively. When compared with the reference materials (TiO$_2$, BiOI and CdS were immobilized on an inert substance cotton cloth, respectively), the photocatalytic degradation rates of MO by TiO$_2$@rGO-F/PVDF–HFP and BiOI@rGO-F/PVDF–HFP and the hydrogen evolution rate by the CdS@rGO-F/PVDF–HFP film

were boosted over 3 times, 21% and 4 times in the presence of magnetic stirring or shaking (regular photocatalytic reaction conditions), respectively. The enhanced photocatalytic efficiency for the hybrids was ascribed to the piezoelectric field over the porous-structure film substrate rGO-F/PVDF–HFP introduced by the mechanical disturbance of water flow, which increased charge transfer rates and suppressed carrier recombination rates during the photocatalytic reaction (Fig. 10a). In another study, organic piezoelectric PVDF was combined with ZnO (an inorganic piezoelectric semiconductor photocatalyst) to study the effect of double piezoelectric fields on the photocatalytic activity.[81] The prepared composite flexible film was found to efficiently deform and generate considerable piezoelectric potential on the surface (varying from -0.30 to $+0.30$ V) driven by water flow. Compared with the control sample (ZnO combined with the organic flexible film polydimethylsiloxane (PDMS) without the piezoelectric effect), the photocatalytic degradation activity was increased by about 35% with the assistance of water flow. These studies implied that the construction of organic-piezoelectric-based photocatalyst hybrid films made the formation of a piezoelectric field in typical catalytic settings possible, and extra energy input was not required to realize the piezo-phototronic effect boosting the photocatalytic performance.

To further make use of water flow, the organic piezoelectric based photocatalyst composite PVDF/g-C_3N_4 with a helical microfiber structure (Fig. 10b) was designed and fabricated *via* microfluidic technology.[82] The resultant sample exhibited greater flexibility and the higher photocatalytic conversion

activity (increased by 20%) of RhB over the PVDF/g-C_3N_4 helical microfibers was detected at a relatively higher water flow rate (100 mL min^{-1}, beneficial for helical microfibers to deform and thus generate piezoelectric potential). With the increases of the screw diameter (from 0.7 to 1.8 mm) and thread pitch (from 1.0 to 4.0 mm) of PVDF/g-C_3N_4 helical microfibers, the photocatalytic degradation efficiencies of RhB increased to the maximum value (with a screw diameter of 1.5 mm and a thread pitch of 1.5 mm) and then decreased, which further substantiated that the greater flexibility of the composite fiber was more favorable for piezoelectric potential generation as well as photocatalytic performance enhancement. Moreover, the dynamic behavior of the photoexcited carriers during the generation and saturation of a piezoelectric field was investigated *via* transient photovoltage and photoluminescence characterization, and the results suggested that the charge separation rate can be boosted by about 4 times in the presence of a piezoelectric field. However, the piezoelectric field could be gradually screened by photoinduced electrons and holes as the light illumination time prolonged in about 16 min, and thus the charge separation was not promoted. Interestingly, the piezoelectric field could be refreshed after the sample was re-deformed and then continued to play a positive role in accelerating carrier separation (Fig. 10b). The significance to emerge from this study was that the periodic or persistent deformation of the piezoelectric substrate was demonstrated to be vitally required for refreshing the piezoelectric field to sustainably promote the photocatalytic activity through direct experimental evidence.
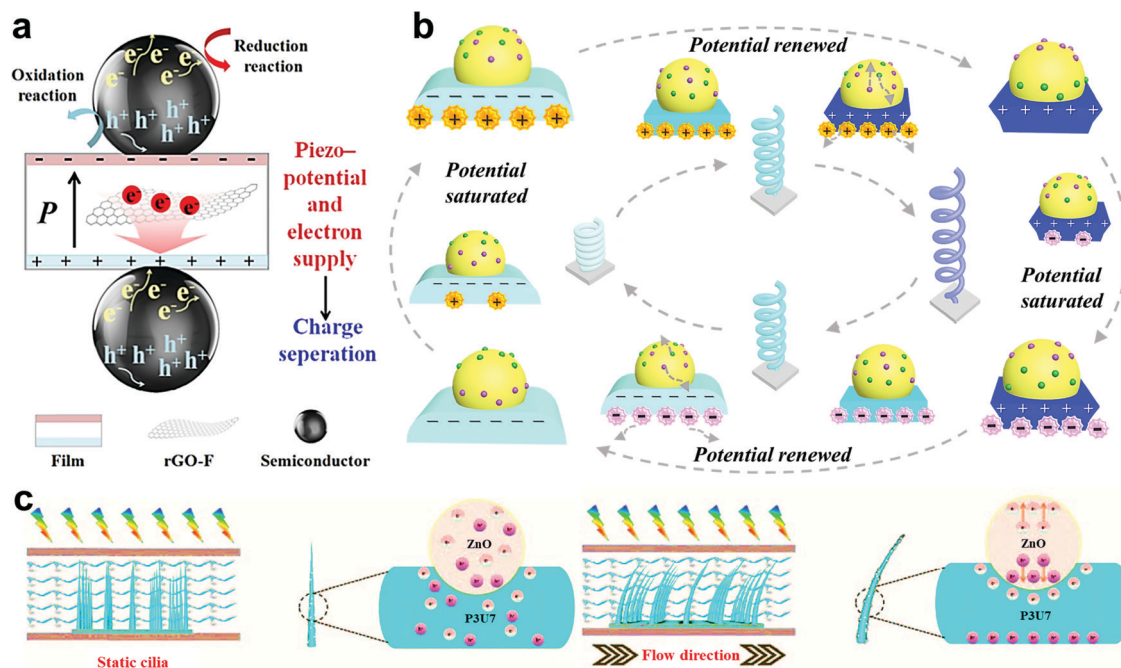

Fig. 10 (a) Schematic illustration of the semiconductors' electron supply and electric potential-enhanced electron–hole separation that stemmed from the migration of electrons in the piezoelectric field within the composite film. Reproduced from ref. 80 with permission from Elsevier Ltd, copyright 2018. (b) Diagram of the process of piezoelectric potential being saturated and self-renewed and the corresponding carrier transfer behavior. Reproduced from ref. 82 with permission from WILEY-VCH Verlag GmbH & Co. KGaA, Weinheim, copyright 2019. (c) Schematic illustration of the surface state of cilia under static state and water flow; P3U7 stands for the weight ratio of PVDF to PU of 3 : 7. Reproduced from ref. 83 with permission from The Royal Society of Chemistry, copyright 2020.

In addition to helical structures, seaweed bio-inspired organic piezoelectric based photocatalysts with a flexible cilia array structure were developed and implanted into a microreactor to maximize the advantage of water wave and solar energy.[83] In this work, piezoelectric PVDF was chosen as the skeleton of the cilia arrays and polyurethane (PU) was introduced to further improve the flexibility of the cilia. ZnO was integrated into the PVDF and PU to endow the cilia arrays with photocatalytic functionality. A 261% higher photocatalytic degradation rate of tetracycline over the composite cilia arrays ZnO/P3U7 (P3U7 stands for the weight ratio of PVDF to PU of 3 : 7) in comparison with the reference sample ZnO/P3U7 film was observed, and the increase was ascribed to the light localization of the cilia arrays. Moreover, compared to ZnO integrated into a non-piezoelectric PDMS cilia substrate, the photocatalytic activity of ZnO constructed with PVDF and PU was increased over 80% with simulated natural water flowing back and forth. The increase was attributed to the enhanced charge separation from the piezoelectric field generated by PVDF (Fig. 10c). When the cilia arrays were implanted into a microreactor (40 mm × 25 mm × 5 mm, as shown in Fig. 10c), due to the fast mass transfer and the low distance between the top and the bottom of the solution in the microreactor, the photocatalytic activity was 222% higher than that in a bulk reactor (60 mL regular photocatalytic reaction reactor). This work implied that the coupling of the piezo-phototronic effect, an accelerated mass transfer rate, and increased light absorption efficiency can be used to further enhance the photocatalytic performance.

These investigations suggested that the robust and tailored structure designs (*i.e.*, flexible porous composite film, helical microfibers, cilia and microreactor) could endow organic-piezoelectric-based photocatalyst hybrids with good flexibility which was highly desirable to realize natural-energy-imparted piezo-phototronic effect improved photocatalysis. Notably, with the exception of the surface plasmon resonance effect discussed in Section 3.3.2, increased light absorption efficiency and fast mass transfer can also be coupled with the piezo-phototronic effect to further boost the photocatalytic performance.

4. Piezo-phototronic effect-enhanced solar cells

4.1 Fundamental process of solar cells

Solar cells are devices that can directly convert solar light into electricity based on the photovoltaic effect and are considered as a means to endless energy as long as sunshine persists.[84] In this regard, various kinds of solar cells have been developed in the past decades, which can be mainly divided into three generations: first-generation solar cells are based on crystalline silicon; second-generation solar cells are based on amorphous and hybrid silicon (such as cadmium telluride, gallium arsenide and copper indium (gallium) selenide thin films); and third-generation solar cells are prepared by simple and low-cost methods (*e.g.*, dye-sensitized solar cells, quantum dot solar cells, organic solar cells, and perovskite solar cells).[85,86] With the rapid development of photovoltaic solar cell technology, the type and number of the third-generation solar cells are constantly increasing.[87,88] Therefore, it is critical to gain insights into the working principles and the physical and chemical processes of solar cells.

A basic solar cell is fabricated with a p–n junction structure, an architecture that is mainly composed of two types of semiconductor (an n-type semiconductor and a p-type semiconductor), electrodes, and an external circuit (Fig. 11a).[89] During the
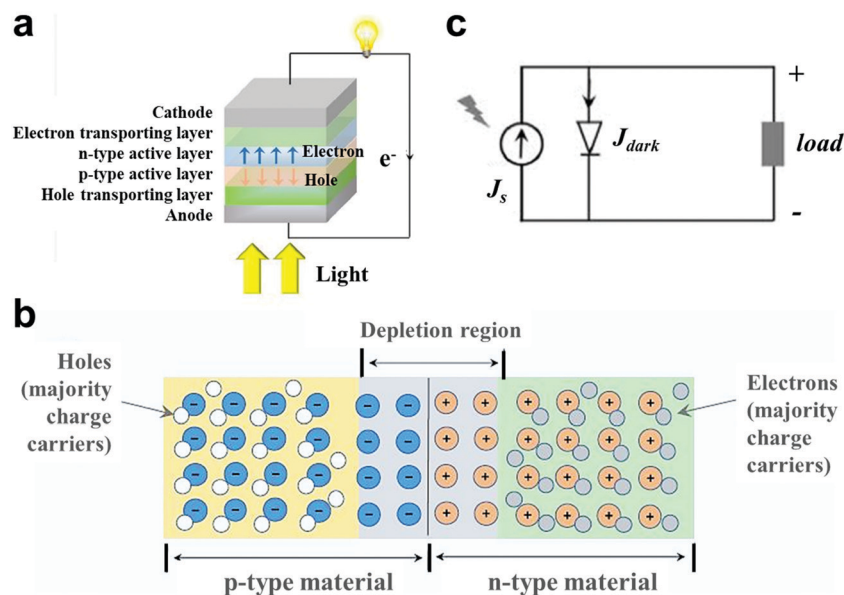

Fig. 11 Schematic diagram of (a) a typical solar cell device structure and (b) carrier transfer close to the p–n junction. Free carriers diffuse close to the junction so that the p-side becomes negatively charged and the n-side becomes positively charged. (c) The equivalent circuit of the ideal solar cell. Reproduced from ref. 89 with permission from Elsevier Inc, copyright 2019.

operation of a solar cell, incident photons with an energy equal to or higher than the band gap of the semiconductors is absorbed, which generates electrons and holes. The photoinduced carriers are then collected and separated spatially by the p–n junction. If light with a photon energy higher than the bandgap of the p–n junction shines the solar cell (*i.e.*, if the solar cell is short-circuited), the carriers will be generated and then flow through the external circuit, and thus both electric current and bias voltage that generate electric power are produced. To better understand the working principles of solar cells, the carrier behavior at the interface of the p–n junction in the dark and under light irradiation is discussed below.

When a p-type semiconductor contacts with an n-type semiconductor without light illumination, the free electrons (majority carriers) of the n-type semiconductor near the p–n junction will transfer to the p-type semiconductor due to the higher concentration of electrons in the n-type region than in the p-type region. The diffusion of free electrons across the junction leads to the formation of a layer of fixed positive charge in the n-type semiconductor (Fig. 11b). Similarly, the majority carrier (free holes) in the p-type semiconductor near the heterojunction will move to the n-type semiconductor and induce a layer of negative charge in the p-type semiconductor. As a consequence, these space charges set up an electrostatic field (built-in electric field) that impedes further diffusion across the junction. Finally, the diffusion of majority carriers and the drifting of minority carriers equilibrate driven by this built-in electrostatic field. Solar cells behave like a diode, and the electrically equivalent model is depicted in Fig. 11c, which can be tuned by a current source in parallel with a diode (formed by a p–n junction). Thus, a much higher electric current will be formed under forwarding bias ($V > 0$) than that obtained under reverse bias ($V < 0$). When solar cells are exposed to light, the photoexcited electrons and holes will transfer towards n-type and p-type semiconductors, respectively, and then get collected at the opposite ends of the p–n junction directed by the built-in electric field. The photocurrent will be produced and the current density is proportional to light intensity, which is divided into two pathways (the diode and the load). The current density of each pathway relies on the resistance of load, diode, and level of illumination. For example, if the resistance of load is larger than that of the diode, much more photocurrent will flow through the diode and a potential difference between cell terminals will be formed.

The most significant parameter to evaluate the performance of solar cells is PCE (the efficiency of incident solar power converted to the maximum output power), which is determined by several factors (Fig. 12).[90] Only photons with an energy higher than the band gap of the semiconductor can be absorbed, and some of these photons cannot be converted to electrical energy due to carrier thermalization (Fig. 12a, inset). It was calculated (based on the Shockley–Queisser (S–Q) limit) that the maximum efficiency of a semiconductor with a 1.34 eV band gap was 33.7% under "one sun" illumination (with the standard AM 1.5 solar spectrum), as presented in Fig. 12b. However, the characterized J_{SC} and V_{OC} were lower than the

corresponding Q–S values due to the poor optical absorption and carrier accumulation rates, and the charge recombination mechanism, respectively. Although the practical performance of solar cells was always lower than the S–Q limit, the performance of solar cells could be enhanced by light and carrier management strategies (Fig. 12c), including constructing solar cell materials with high light absorption, optimizing the material structure, and promoting charge separation. Recently, the piezo-phototronic effect was reported to be an effective method to significantly improve the output power by modulating charge separation and transfer motion in solar cells.[91]

4.2 Mechanism of the piezo-phototronic effect in enhancing solar cell performance

Recently, the development of piezotronics and piezo-phototronics, accompanied with novel physical science, has attracted increasing interest, and the corresponding device applications have been sparked. The piezo-phototronic effect can intriguingly impact the transfer behavior of photogenerated carriers at the interface/junction of optoelectronic devices and thus influence performance. Notably, enormous research studies have demonstrated that the piezo-phototronic effect endows solar cells with enhanced performance by modulating the band structure at the p–n junction interface and therefore promote charge separation.[92] The detailed mechanisms of using the piezo-phototronic effect to tune the performance of solar cells is described in the following part.

As shown in Fig. 13, when a p-type semiconductor and an n-type semiconductor are contacted and form a junction, the holes at the p-type side and the electrons at the n-type side tend to redistribute to balance the local potential, which leads to the formation of a charge depletion zone in the junction *via* the interdiffusion and recombination of the electrons and holes.[93] When light shines on a solar cell device, the photoexcited electrons and holes will transfer from the depletion layer to the n-type and p-type semiconductor regions driven by the built-in electric field, respectively, and thus create photocurrent. Notably, the n-type semiconductor can be piezoelectric, and piezoelectric charges can be formed on its surface under applied strain. When positive piezoelectric polarization charges are generated and distribute in the n-type region (Fig. 13a), the depletion layer region will expand and shift to the p-type side, increasing the effective series resistance for charge injection to the contact and thus decreasing the current output. Moreover, the formation of a charge channel in the conduction band and the downward bending of the valence band edge on the n-type side will give rise to less-effective charge separation. Conversely, when negative polarization charges are introduced and distribute at the junction in the n-type region, the depletion layer region will expand and move to the n-type side, which will consequently decrease the effective series resistance for charge injection to the contact and therefore improve the current output (Fig. 13b). Importantly, upward band bending can restrict charge recombination and efficiently facilitate carrier separation. To this end, piezoelectric polarization charge enabled piezoelectric potential at the junction or interface can function as
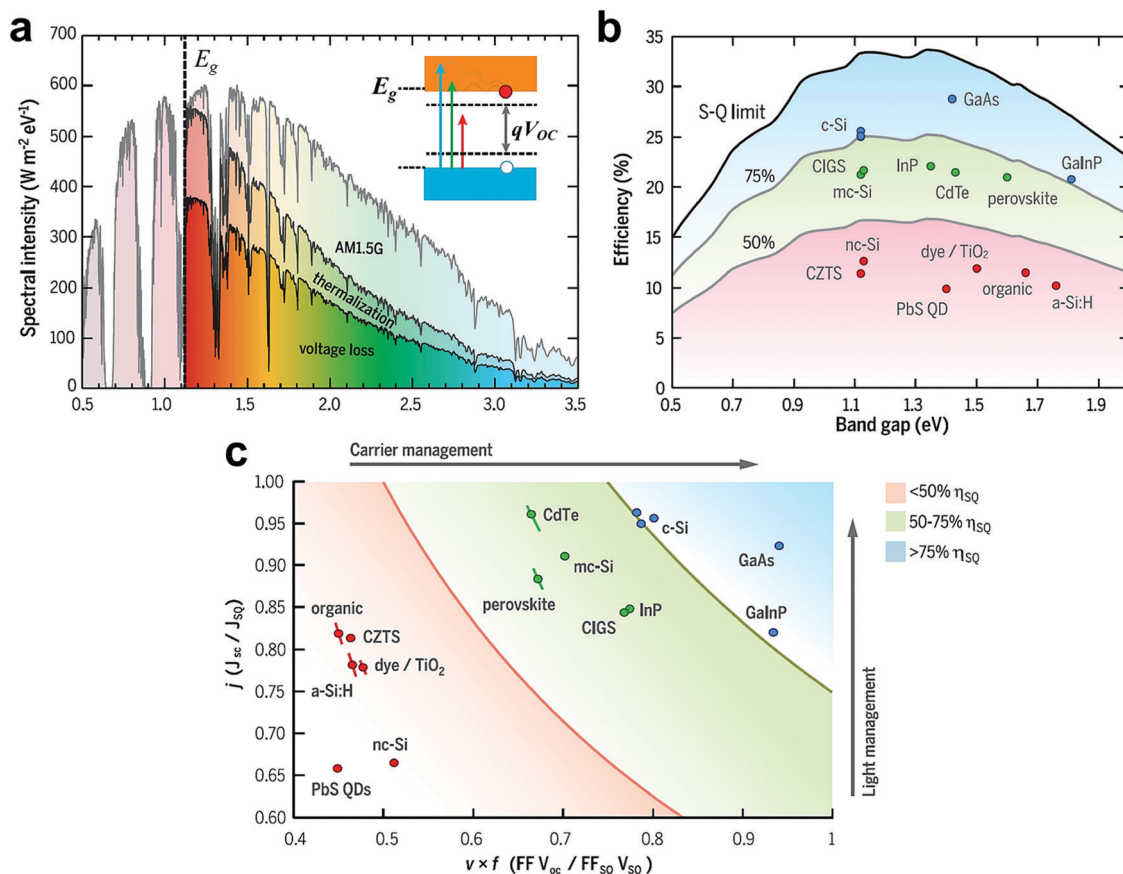
Fig. 12 Fundamental solar cell efficiency limits and state-of-the-art records. (a) The AM 1.5 solar spectrum with distinct dips due to molecular absorption in Earth's atmosphere. Photons with energies above the band gap are not fully converted to electrical energy because of thermalization of charge carriers. The maximum power generated by the cell is limited by voltage loss relative to the band gap voltage. The inset of (a) stands for the electronic band structure with the separation of the quasi-Fermi levels determining the open-circuit voltage. (b) Theoretical Shockley–Queisser detailed-balance efficiency limit as a function of band gap (black line) and 75% and 50% of the limit (gray lines). (c) An efficient solar cell captures and traps all incident light ("light management") and converts it into electrical carriers that are efficiently collected ("carrier management"). Reproduced from ref. 90 with permission from Science, copyright 2016.

a "gate" voltage to modulate the energy band structure of the heterojunction and hence tune charge separation, transport, and/or recombination during the solar cell operation, resulting in either an enhanced or a reduced photocurrent.[26] Therefore, it is important to govern/manage the applied force (direction and strength) to realize the piezo-phototronic effect enhanced photovoltaic solar cell devices.

4.3 Solar cells under the application of the piezo-phototronic effect

Owing to the modulation role of the piezo-phototronic effect in optoelectronic processes, various types of solar cells enabled by the piezo-phototronic effect have been developed, including silicon-based solar cells, quantum dot solar cells, dye sensitized solar cells and perovskite solar cells. Some representatives and their performance controlled by the piezo-phototronic effect are summarized in Table 3.[92,94]

4.3.1 Silicon-based solar cells. Silicon, the most classical semiconductor, can be converted to p-type or n-type by doping with different kinds of impurities. Silicon-based solar cells have

been studied intensively for some decades and are the most widely used photovoltaic devices due to their low cost and long lifetime.[95] Although great achievements have been made, the conversion efficiency (quantum yield) of silicon-based solar cells is still limited by their poor light absorption and high carrier recombination rate. In this context, the piezo-phototronic effect could be used to improve the efficiency of silicon-based solar cells by promoting charge separation. For instance, Zhu and co-authors prepared a silicon-based heterostructure (p^+-Si/p-Si/n^+-Si/n-ZnO nanowire arrays) photovoltaic solar cell device (Fig. 14a), in which the nanowire array structure endowed the device with high light absorption and piezoelectric potential under applied strain.[96] Their results showed that, under a static comprehensive strain of 800 kPa, the PCE increased from 8.97% to 9.51%, which was attributed to the positive role of the piezo-phototronic effect in modulating charge behavior. Fig. 14b describes the energy band gap of the interface of p-Si and n^+-Si. It should be noted that there was a surface barrier due to the lower P^+ density at the surface than that at the inner of n^+-Si, and thus a large number of
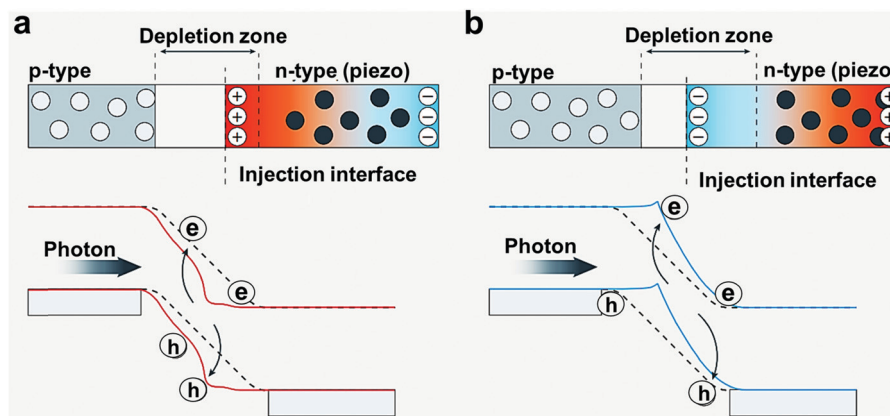
Fig. 13 Schematic illustration of energy band diagrams for the piezo-phototronic effect tuned p–n junction contacts under positive (a) and negative (b) piezoelectric potentials introduced in the n-type semiconductor side. Reproduced from ref. 93 with permission from Macmillan Publishers Limited, copyright 2016.

Table 3 Summary of typical solar cells with the piezo-phototronic effect and their performance

Materials for constructing solar cells	Applied strain	Performance			Ref.
		PCE (%)	J_{SC} (mA cm^{-2})	V_{OC} (V)	
p$^+$-Si/p-Si/n$^+$-Si/n-ZnO NW arrays	800 MPa compressive strain	8.97 (without strain) 9.51 (with strain)	4.66 (without strain) 4.71 (with strain)	0.54 (without strain) 0.58 (with strain)	96
ZnO/PbS QDSCs (PbS QDs deposited on a ZnO thin film)	−0.25% compressive strain	3.1 (without strain) 4.0 (with strain)	—	—	99
nGaN/GaN MQW	0.134% tensile strain	1.12 (without strain) 1.24% (with strain)	1.05 (without strain) 1.17 (with strain)	Basically stable	100
Ag-InGaN/GaN MQW	0.152% tensile strain	0.98 (without strain) 1.25 (with strain)	1.03 (without strain) 1.37 (with strain)	Basically stable	101
ZnO@N719	0.5% tensile strain	0.45 (with strain)	Basically stable	0.49 (without strain) 0.57 (with strain)	102
Cu$_2$S/CdS NWs	−0.41% compressive strain	—	0.25 nA (without strain) 0.33 nA (with strain)	0.26 (without strain) 0.29 (with strain)	106
Cu(In,Ga)Se$_2$	0.74% tensile to −0.74% compressive strain	4.82 (0.74% strain) 5.97 (−0.74% strain)	18.81 (0.74% strain) 22.22 (−0.74% strain)	0.505 (0.74% strain) 0.523 (−0.74% strain)	109
ZnO/CH$_3$NH$_3$PbI$_3$ (the c-axis of ZnO pointing away from the perovskite)	−0.8% compressive strain	0.0216 (without strain) 0.298 (with strain)	2.07 nA (without strain) 15.10 nA (with strain)	0.59 (without strain) 0.74 (with strain)	110
	0.71% tensile strains	—	5.93 nA (without strain) 4.19 nA (with strain)	0.73 (without strain) 0.70 (with strain)	
ZnO/CH$_3$NH$_3$PbI$_3$ (the c-axis of ZnO pointing towards the perovskite)	−0.42% compressive strain	—	77.60 nA (without strain) 59.50 nA (with strain)	0.86 (without strain) 0.81 (with strain)	
	0.30% tensile strain	0.068 (without strain) 0.352 (with strain)	14.80 nA (without strain) 87.20 nA (with strain)	0.72 (without strain) 0.86 (with strain)	
ZnO NWs/CH$_3$NH$_3$PbI$_3$	1.88% tensile strain	9.3 (without strain) 12.8 (with strain)	17.8 (without strain) 23.5 (with strain)	Basically stable	111
ZnO@ZnS/Cs$_{0.05}$(FA$_{0.83}$MA$_{0.17}$)$_{0.95}$Pb (I$_{2.6}$Br$_{0.4}$)	1.5% tensile strain	12.94 (without strain) 14.68 (with strain)	21.82 (without strain) 24.40 (with strain)	—	4

photogenerated electrons were trapped in the middle of n$^+$-Si. When compressive strain was applied, piezoelectric potential was formed and distributed along the ZnO nanowires. Meanwhile, positive piezoelectric polarization charges appeared at the junction, further lowering the energy level of the depletion zone between n$^+$-Si and n-ZnO. As a result, the electrons that were trapped in n$^+$-Si were released and then moved to n-ZnO (Fig. 14c), leading to increased photoinduced carriers. Moreover, the flow of trapped electrons gave rise to a temporary increase of J_{SC}, V_{OC} as well as the PCE. It should be noted that the enhancement of J_{SC} (from 4.66 to 4.71 mA cm^{-2}) and V_{OC} (from about 0.54 to 0.58 V) was not very high in the presence of compressive strain because of

the screen effect of photoexcited free carriers on the piezoelectric charges at the end of ZnO nanowires. Conversely, when tensile strain was introduced, negative piezoelectric polarization charges distributed at the bottom surfaces, which increased the energy level of the depletion zone between n$^+$-Si and n-ZnO (Fig. 14d), increasing the number of trapped electrons. Consequently, the J_{SC}, V_{OC} and PCE of solar cells were reduced as the applied tensile strain increased. This work provided a strong demonstration that the performance of silicon-based solar cells could be efficiently modulated by applied strain via the piezo-phototronic effect, and it is crucial to introduce an appropriate strain to achieve a higher solar cell conversion efficiency.
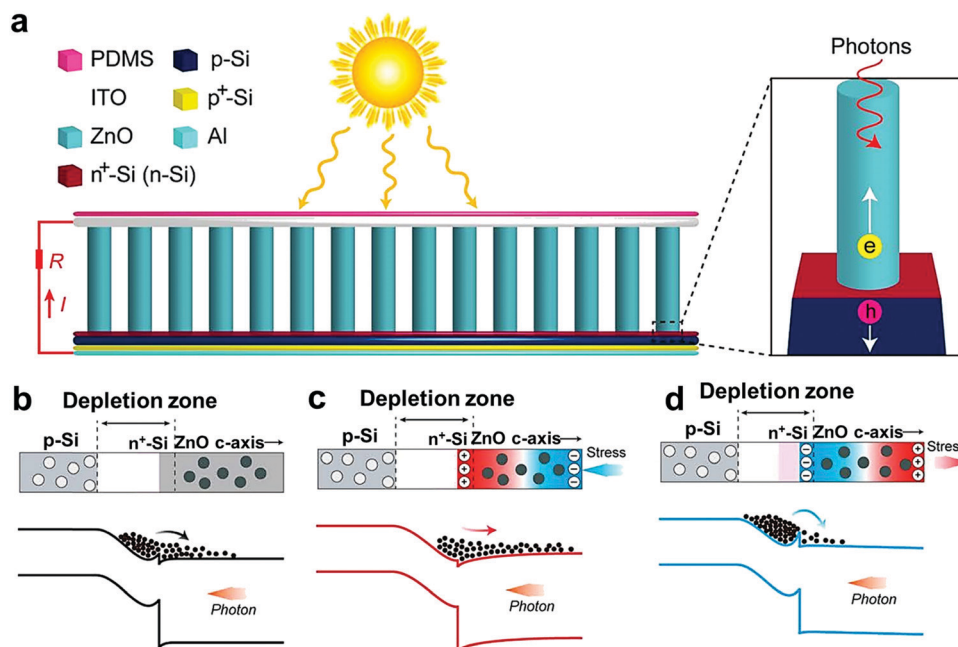
Fig. 14 (a) Schematic diagram of the prepared silicon-based solar cell. Under illumination, photoexcited electron−hole pairs are produced and subsequently separated at the n-ZnO nanowire/n⁺-Si/p-Si interface because of band bending and internal field. The electrons and holes move to the ZnO nanowire and p-Si, respectively. Energy band diagram of the p⁺-Si/p-Si/n⁺-Si/n-ZnO nanowire array solar cell (b) without strain and under (c) compressive strain and (d) tensile strain on the device. Reproduced from ref. 96 with permission from American Chemical Society, copyright 2017.

4.3.2 Quantum dot solar cells. Quantum dot solar cells (QDSCs) are another class of solar cells in which quantum dots serve as the absorbing photovoltaic material. Due to the tunable size of quantum dots (QDs), the bandgap of QDSCs can be tailored across a wide range of energy levels, making QDSCs attractive for use in multi-junction solar cells with high quantum efficiency. Therefore, QDs can be designed to replace bulk materials (i.e., silicon, copper indium gallium selenide and cadmium telluride) which have a fixed energy bandgap. In addition, QDSCs display long-lifetime hot carriers, tunable spectral absorption, and multiple exciton generation by a single photon, and are cost efficient. These properties endow QDSCs with great potential in converting solar energy into electricity with high efficiency.[97] To further improve energy conversion efficiency, endeavors have been made based on developing QDSCs, and it was reported that the PCE of QDSCs could be theoretically increased up to 66% due to their excellent hot carrier collection ability.[98] Although their theoretical efficiency is high, the performance of QDSCs is still hampered by low charge-extraction/transport rates. Fortunately, in recent years, the piezo-phototronic effect was proposed to overcome this problem and has been demonstrated to be a promising strategy to realize a higher performance of QDSCs.

P-type PbS QDs were deposited on the surface of an n-type ZnO thin film substrate by a layer-by-layer dip-coating method to prepare QDSCs.[99] The PCE of the designed ZnO/PbS QDSC device was about 3.1% in the absence of strain and 4.0% under a compressive strain of −0.25% (the efficiency was increased by about 30%). In addition, an approximately linear relationship between the applied strain (varying from −0.25% to 0.15%) and

PCE of QDSCs was presented, with efficiency increasing 1.2% with the strain dropping by 0.01%. These results corroborated the modulation role of the piezo-phototronic effect in tuning the performance of QDSCs. Moreover, a higher PCE for ZnO/PbS QDSC devices was attained under a lower illumination intensity. It was caused by the reduced effective depletion region (originated from the high intensity charged surface and trap states), which promoted the recombination of photoexcited carriers. This work implied that light illumination intensity also played a non-negligible role in solar cell processes, and the external strain as well as light irradiation intensity should be taken into account to gain high performance QDSCs.

Based on QDSC devices, many multiple quantum well (MQW) solar cells were also developed, and they showed promise in yielding a high short-circuit current density and a high conversion efficiency. Notably, the performance of MQW solar cells can also be motivated by the piezo-phototronic effect. For example, under an applied strain of 0.134%, both the PCE and J_{SC} of InGaN/GaN MQW solar cells were improved by about 11%, which was attributed to the role of the piezo-phototronic effect in promoting charge separation, as depicted in Fig. 15.[100] In detail, when external strain was applied on the InGaN/GaN MQW, external-stress-enabled piezoelectric charges were generated at the interfaces of the barrier and well, which partly compensated the internal-strain-imparted charges in InGaN wells (Fig. 15a). As such, the optical transition was tuned by external strain. Moreover, a self-consistent numerical model established in this work was used to calculate the energy band profiles in InGaN/GaN MQW solar cells with and without external strain, as shown in Fig. 15b–d. The calculation indicated that the valence
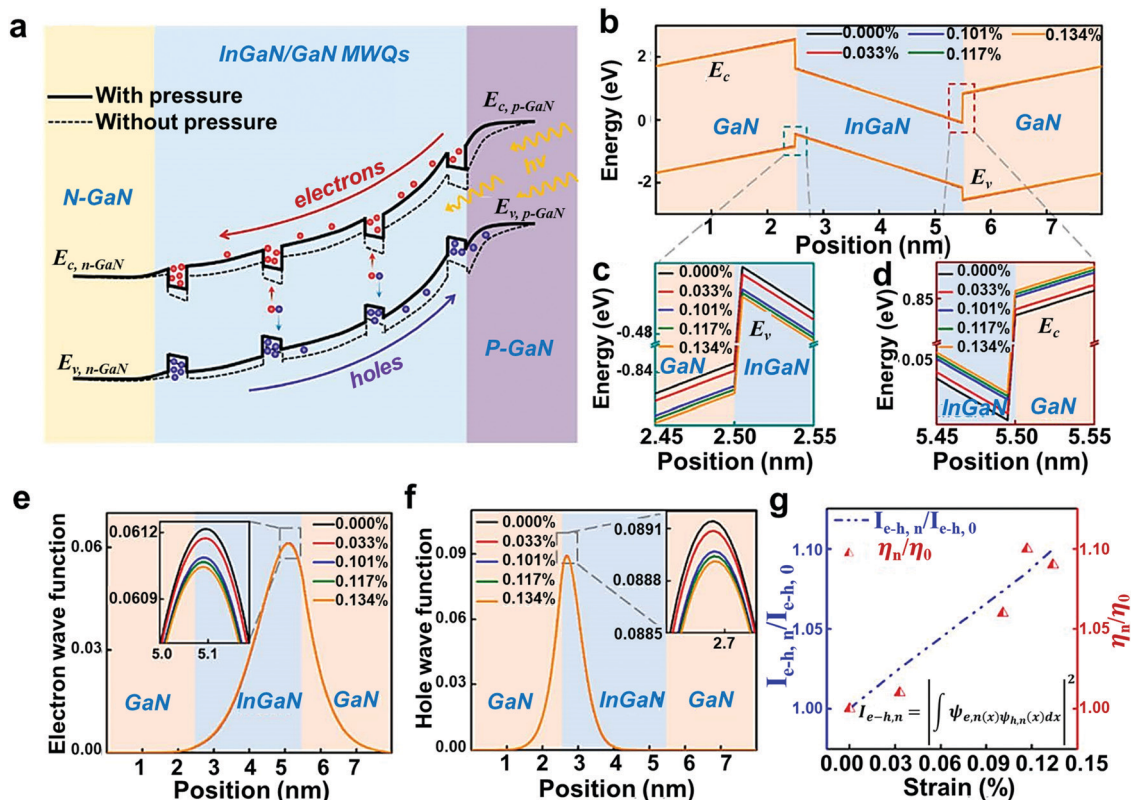
Fig. 15 (a) Mechanism of the InGaN/GaN MQW solar cell modulated by the piezo-phototronic effect. The dashed line and solid line indicate the schematic band diagram of the InGaN/GaN MQW structure with and without strain/pressure, respectively. (b) Calculated energy band profiles of the GaN/InGaN/GaN heterostructure from top to bottom under strain-free and various straining conditions. Enlarged (c) E_v at the GaN/InGaN and (d) E_c at the InGaN/GaN heterojunction interface as labeled in (b) with green and red rectangles, respectively. (e) Electron and (f) hole wave function distribution with and without strain (dark line). The inset shows the shifting peak position. (g) Normalized square of the spatial overlap of the electron–hole wave functions and the normalized experimental conversion efficiency of the solar cell under strain-free and various straining conditions. $I_{e-h,n}$ (n = 0, 1, 2, 3, 4, 0 stands for the device under no strain and 1–4 represent the device under different external strains). Reproduced from ref. 100 with permission from American Chemical Society, copyright 2017.

and conduction bands of the GaN/InGaN heterojunction trended downward and upward as the external strain increased, respectively. With respect to the quantum well structure, the lattice-mismatch-induced strain between the quantum barrier and well was partly compensated by this external strain. In addition, the enhanced optical absorption in the quantum well (more optical-generated carriers) was corroborated by the electron and hole wave functions, which moved toward the well (Fig. 15e and f). Fig. 15g suggests that the optical absorption coefficient was proportional to the square of the spatial overlap of the electron–hole wave functions, and as the external strain increased, the spatial overlap increased accordingly. Notably, the detected experimental PCE of the MQW solar cell was in good agreement with the calculated results of spatial overlap of electron–hole wave functions in this work, verifying the piezo-phototronic effect-enhanced MQW solar cell conversion efficiency.

Based on the above MQW solar cell, surface plasmon polaritons (utilizing the localized electromagnetic field surface waves that travel along the interface of the metal and dielectric and introducing electron-plasma resonance inside the material, which increases the local electromagnetic field and thus engineers the optoelectronic process) employing the scattering from the

metal have been introduced into the solar cell system to further enhance the energy conversion efficiency (Fig. 16).[101] In their work, as depicted in Fig. 16a, Ag nanoparticles were thermally annealed and distributed in a rectangular region on the surface of p-type GaN, and then an ITO layer with a thickness of about 200 nm was deposited. The current density–voltage curves of the MQW solar cell with and without Ag nanoparticles under AM 1.5 illumination indicated that the introduction of Ag resulted in an improved J_{SC} (Fig. 16b). The improvement was attributed to the increasing light absorption of Ag nanoparticles in the quantum well region and coupling incident light into guided modes to propagate through the MQW region. Importantly, compared with InGaN/GaN MQW solar cells without Ag nanoparticles, a 40% increase in J_{SC} and a 66% enhancement in PCE were achieved in the presence of a 0.152% external strain (Fig. 16c), thanks to the coupling of plasmonic with the piezo-phototronic effect (an increased effective absorption cross-section and a reduced optical reflection loss observed in the solar cell with Ag, and an increase of photogenerated carriers caused by more lattice relaxation under compressive residual stress, described in Fig. 16d and e). This work provided a demonstration that the performance of MQW solar cells can be further improved by coupling the
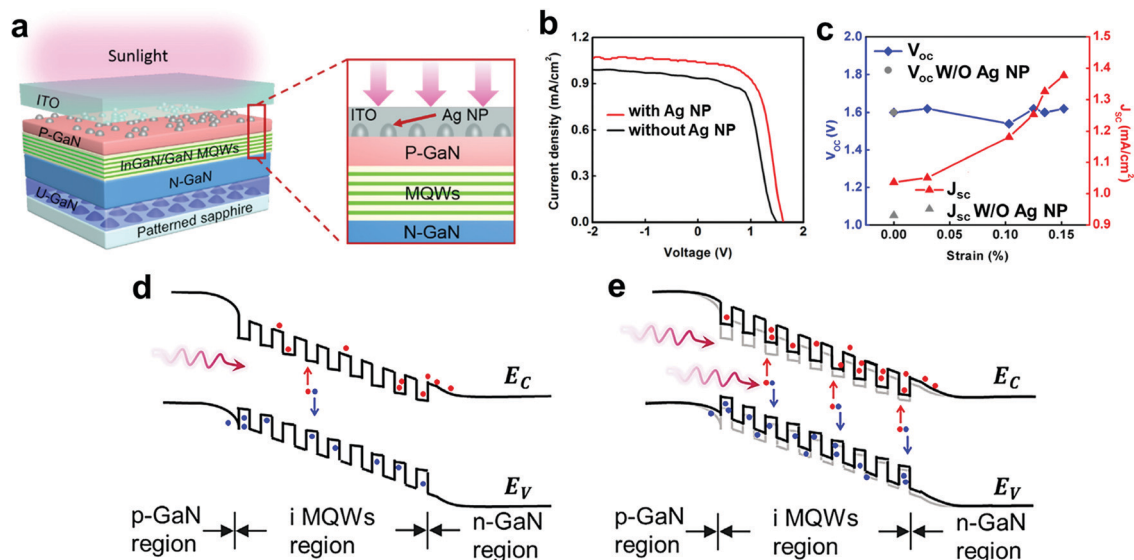
Fig. 16 (a) A schematic of the InGaN/GaN MQW solar cell structure with Ag nanoparticles. The magnified cross-sectional view of the multilayered structure shows the plasmonic nanostructures. (b) Illumination intensity and (c) external strain dependence of V_{OC} and J_{SC}. Mechanisms of the InGaN/GaN MQW solar cell (d) before and (e) after applying Ag NPs and compressive stress on the device, showing the modulation effect of the plasma coupling with the piezo-phototronic effect. Reproduced from ref. 101 with permission from Elsevier Ltd, copyright 2018.

piezo-phototronic and plasmonic effects, presenting a simple, viable yet efficient path to developing high conversion efficiency solar cells.

4.3.3 Dye sensitized solar cells. Dye sensitized solar cells (DSSCs) comprise four parts (Fig. 17a): the photo-sensitizer (dye), photo-anode (wide band gap metal oxide coated with a transparent conducting substrate), electrolyte (redox couple) and counter electrode (Pt coated with a conducting substrate).[86] The basic process of DSSCs is illustrated in Fig. 17b. At first, the photo-sensitizer (dye) is photoexcited under light illumination. Then, the excited electrons transfer to the conduction band of metal oxide and penetrate through the metal oxide film, arriving to the conducting substrate and flowing through an external circuit to the counter electrode. Meanwhile, the oxidized component of the redox couple is reduced at the counter electrode and the oxidized substance of the dye is regenerated by the reduced component of the redox couple in the electrolyte. As is true with all solar cells, charge collection and transport of photogenerated electrons play a key role in the solar cell process. To better dictate the behavior of photoinduced carriers and achieve a higher performance of DSSCs, the piezo-phototronic effect was introduced into the DSSC system, which has been demonstrated to be an efficient method to motivate charge separation and transport.

For example, the well-known ruthenium-based dye di-tetra-butylammonium *cis*-diisothiocyanato-bis(2,2′-bipyridyl-4,4′-di-carboxylic acid) ruthenium(II) (N719) was combined with ZnO (an inorganic piezoelectric semiconductor) to synthesize a nanocrystalline ZnO@N719 adduct to improve the performance of DSSCs.[102] The constructed ZnO@N719 nanoadduct possessed good piezoelectric properties, generating a bias of 1.9 V under a strain of 0.27%. Importantly, the V_{OC} value of DSSCs was modulated by polarization charges introduced by external strain and the

width of the piezoelectric charge distribution region. In this work, the V_{OC} value of the proposed ZnO@N719 based DSSC device was boosted by about 14% in the presence of an applied strain of 0.5%, which was ascribed to the positive effect of the piezoelectric field on charge separation. On the contrary, there was almost no difference in the J_{SC} values of normal solar cell devices under the characterization conditions with and without external strains. In their opinion, the unchanged short-circuit current density was attributed to the high J_{SC} value of the device, and the impact of saturation current density on total current density could be neglected. This work demonstrated how the piezo-phototronic effect can be used to significantly increase the open circuit voltage of DSSCs, opening a new avenue to further improve the performance of solar cells.

4.3.4 Perovskite solar cells. Since the first perovskite solar cell (PSC) was made in 2009, they have rapidly gained interest. Most PSCs consist of a perovskite layer, an electron-transporting layer and a hole-transporting layer, with the perovskite layer fixed between the electron- and hole-transporting layers.[103] Compared with traditional solar cells, PSCs have many advantages in light absorption, charge separation, and conversion efficiency.[104] PSCs have been recognized as one of the most promising next-generation photovoltaic solar cells. In the past years, to improve the performance of PSCs, tremendous efforts have been made, such as developing new perovskite material, interface engineering, and configuration designs.[105–107] Although some successes have been achieved, there is still room to further enhance the performance of PSCs. Recently, the piezo-phototronic effect has been corroborated as a robust and ingenious method to improve the performance of piezoelectric semiconductor perovskite and piezo-electric semiconductor/perovskite solar cells.[108,109]

In one study, a single ZnO microwire was employed as the electron transporter on a flexible polystyrene (PS) substrate to
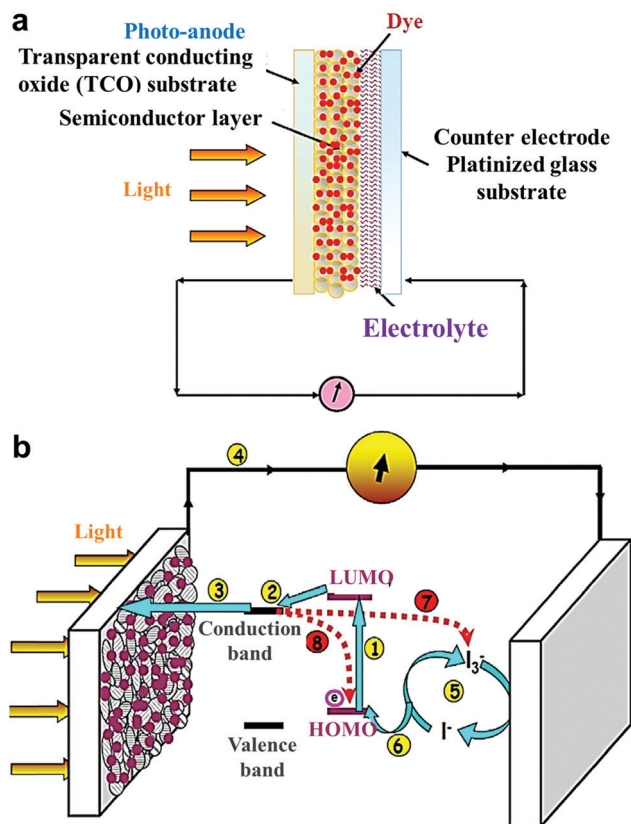
Fig. 17 Schematic diagram of (a) DSSCs and their components, and (b) the process of DSSCs (routes 1–8 represent photo-excitation of electrons in the dye, injection of electrons from the dye to the conduction band of metal oxide, transfer of electrons from metal oxide to the transparent conducting glass substrate, conduction of electrons from the photo-anode to the cathode, reduction of tri-iodide to iodide, oxidation of iodide to tri-iodide and regeneration of the dye, recombination of photo-excited electrons with the oxidized dye and recombination of photo-excited electrons with the oxidized tri-iodide, respectively). Reproduced from ref. 86 with permission from Elsevier Ltd, copyright 2016.

form a heterojunction with the perovskite $CH_3NH_3PbI_3$ to construct flexible photovoltaic solar cells.[110] Their results suggested that the strain-induced piezoelectric polarization charges in the vicinity of the ZnO/perovskite interface can promote the transport and separation of photoexcited carriers. The V_{OC}, J_{SC} and PCE of the prepared solar cell were increased by 25.42%, 629.47% and 1280% (from 0.0216% to 0.298%) under an applied compressive strain of 0.8%, respectively. To investigate the physical working mechanism for the enhanced performance of the ZnO/perovskite solar cell, a theoretical model based on energy bands (the ZnO/perovskite solar cell was treated as a p–n junction) was proposed (Fig. 18). As displayed in Fig. 17b and 18a, the heterojunction was formed between ZnO and the perovskite without strain and the solar cell performance was mainly determined by charge generation and transfer processes (Fig. 18b). Under light illumination, the electrons and holes were generated over $CH_3NH_3PbI_3$ due to its low energy bandgap of about 1.5 eV, which would be separated by the built-in electric field across

the depletion region. As a result, the photoexcited electrons and holes were found to move to the ZnO nanowire and hole transport material layer, respectively. When external strain was applied on the ZnO nanowire, the energy band at the ZnO interface was changed due to the piezoelectric effect. When the strain-enabled positive piezoelectric charges occurred at the perovskite/ZnO interface, the local piezoelectric charges gave rise to lowered conduction and valence bands of ZnO at the interface (Fig. 18c and d). Therefore, the barrier height at the perovskite/ZnO interface was decreased and the depletion width increased, strengthening the built-in electric field and consequently promoting the separation rate of photogenerated carriers. As a result, the performance of solar cells was improved (V_{OC}, J_{SC} and PCE were increased from 0.59 to 0.74 V, from 2.07 to 15.10 nA and from 0.0216% to 0.298%, respectively). Conversely, when the strain-imparted negative piezoelectric charges emerged at the perovskite/ZnO interface, the local piezoelectric charges caused the energy bands of ZnO to bend upward at the interface, which led to an increased barrier height at the perovskite/ZnO interface (Fig. 18e and f). The decreased depletion width and weakened built-in electric field boosted the recombination efficiency of photoinduced carriers and hence decreased the power conversion efficiency of the solar cells. This work was the first to experimentally illustrate the mechanism of how the piezo-phototronic effect modulates the performance of PSCs. It is necessary to point out that, to obtain enhanced performance of solar cells, optimizing/tuning the applied strain (in terms of direction and strength) to ensure the positive role of the piezo-phototronic effect in modulating optoelectronic processes (promoting charge separation and migration) is of great importance.

Based on the abovementioned work, ZnO nanowire arrays were used as the electron transport layer and combined with the perovskite $CH_3NH_3PbI_3$ to fabricate flexible hybrid PSCs (Fig. 19a).[111] In the presence of a 1.88% static strain, the absolute PCE of the constructed solar cell device was enhanced from 9.3% to 12.8% (increased by about 40%) and the J_{SC} was increased from 17.8 to 23.5 mA cm^{-2} (Fig. 19b), which was ascribed to the modulation from the piezo-phototronic effect. This work offered a robust approach to improve the performance of ultrathin and flexible PSCs by applying external strain, further corroborating the significant role of the piezo-phototronic effect in dictating the separation and transport behavior of carriers. Although ZnO is a good electron-transport layer candidate, its Lewis base character and surface defects may cause deprotonation of the perovskite, leading to severe degradation of PSCs. To solve this problem, the surface of ZnO nanorods was decorated with ZnS (forming a ZnO@ZnS core–shell nanorod), and the ZnO@ZnS was used as a bifunctional interfacial layer (Fig. 19c).[4] In the designed PSCs, ZnS was found to passivate the ZnO/perovskite interface by reducing the hydroxyl groups on the ZnO surface and also coordinate with Pb^{2+} of the perovskite to form a strong Zn–S–Pb pathway and thus tune energy levels for efficient electron transport. As such, compared with a device using just ZnO as the electron-transport layer, the PCE of the flexible PSCs constructed with ZnO@ZnS only decreased by about 12% after simulated solar
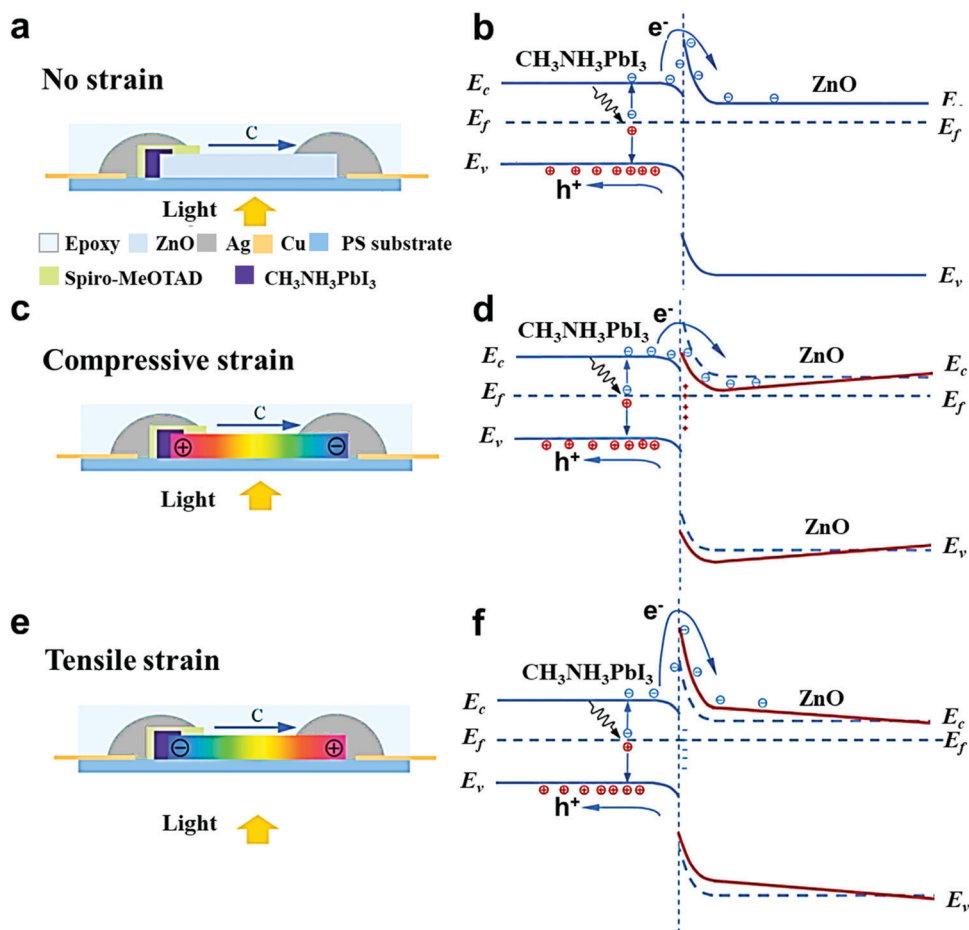
Fig. 18 Schematics and energy band diagrams demonstrating the piezo-phototronic effect on perovskite/ZnO single micro/nanowire solar cells. Piezoelectric potential generated and distributed on the solar cell device (a) without strain and under (c) compressive and (e) tensile strain, and (b, d and f) the corresponding energy band diagrams. Reproduced from ref. 110 with permission from Elsevier Ltd, copyright 2016.

light irradiation for 300 min, exhibiting good stability (Fig. 19d). Moreover, the PCE and J_{SC} of the prepared ZnO@ZnS/perovskite solar cells were increased by about 13.4% and 11.8% under a static external tensile strain of 1.5%, respectively (Fig. 19e). The increase was attributed to the modulated energy band structure of the ZnS/ZnO and ZnS/perovskite interface by the strain-induced piezo-polarization charges. This work implied that tailored structural designs (tuning the energy band structure at the interface) on perovskite solar cell devices with the piezo-phototronic effect can further improve the performance of solar cells.

Other piezoelectric semiconductors such as CdTe, CdSe, CdS, InP, InAs, InN, GaN, AlN and GaAs can also be utilized as electron transport layers to enhance the V_{OC} and PCE of perovskite-based solar cells.[112] The PCE and V_{OC} results showed that, among the abovementioned nine types of piezoelectric semiconductors, GaN and AlN presented the greatest potential to endow PSCs with a higher PCE (25.46% for GaN and 26.42% for AlN) under an applied strain of 1% due to their relatively large piezoelectric constants and small relative dielectric constants. Moreover, PSCs with a GaN electron-transport layer exhibited a higher V_{OC} of 0.713 V (increased by about 3.8% in comparison with that detected in the absence of strain) and a

PCE of 25.46% under an applied strain of 1%, thanks to the positive role of the piezo-phototronic effect. This work indicated that piezoelectric semiconductors can play a versatile role in enhancing the performance of PSCs *via* the piezo-phototronic effect, and appropriate material composition construction is needed to further optimize the properties of solar cells.

5. Piezo-phototronic effect-modulated photodetectors

5.1 Brief introduction to photodetectors

Photodetectors are vital devices for applications in light-wave communication, detection of light, measurement of the mechanical behavior of live cardiomyocytes, and optoelectronic circuits that can be distinguished into photo-emissive detectors (photocathodes) and semiconductor detectors.[113,114] In photo-emissive detectors, when photons irradiate the cathode of the detector material, electrons will be emitted into vacuum. The applied voltage difference between the photocathode and anode provides a driving force to collect the electrons, resulting in current. Differently, for semiconductor photodetectors, when
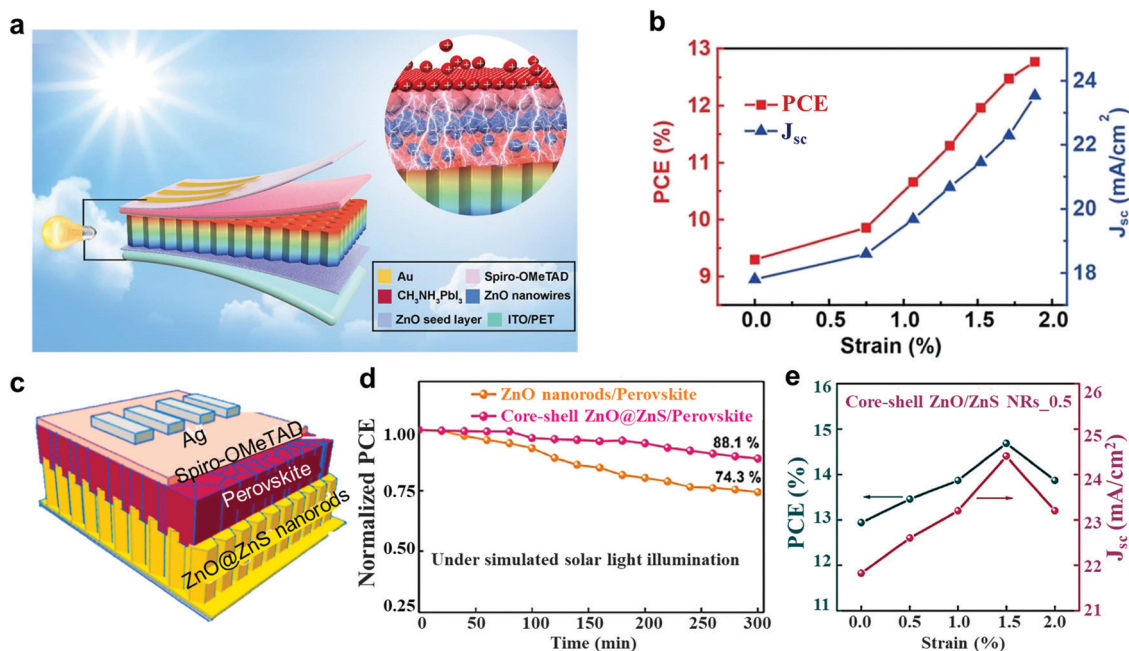
Fig. 19 (a) Schematic diagram of the ZnO nanowire perovskite solar cell. Under light irradiation, the photoinduced carriers get separated at the interface between ZnO and the perovskite, and the electrons then transport toward the ZnO nanowire. (b) Dependences of the PCE and J_{SC} of the prepared ZnO/perovskite solar cell under continuous static tensile strains. Reproduced from ref. 111 with permission from American Chemical Society, copyright 2019. (c) Schematic illustration of the constructed ZnO@ZnS/perovskite solar cell device. (d) PCE stability of the prepared unencapsulated devices stored in an ambient environment under 1 sun AM 1.5G illumination, and (e) the dependences of the PCE and J_{SC} of the prepared perovskite solar cells with ZnO@ZnS nanorods serving as the electron-transport layer under applied strain, respectively. Reproduced from ref. 4 with permission from Elsevier Ltd, copyright 2021.

the photons with an energy higher than the bandgap of the semiconductor shine on the detector, electron–hole pairs will be excited by the photons. These photoexcited electrons and holes will be separated by the built-in electric field of the semiconductor or the applied voltage, generating photocurrent proportional to the photon flux. The most used photodetectors are designed based on the metal–semiconductor contact and p–n junction.

The main parameters to evaluate the performance of semiconductor photodetectors are responsivity (R_i), gain (g, number of carriers detected per photogenerated electron–hole pair), quantum efficiency (η, number of electron–hole pairs generated per incident photon), response time, bandwidth (BW), noise equivalent power (NEP) and detectivity (D^*).[113] Responsivity is the photocurrent per unit of incident optical power, which is determined by the quantum efficiency and gain ($R_i = \frac{\lambda \eta}{hc} qg$, where λ, h, c and q are the wavelength of light, Planck constant, the speed of light and electron charge, respectively). The photodetector response time is evaluated by the decay time (τ_d) or rise time (τ_r), which is the time needed for the photocurrent to drop from 90% to 10% or increase from 10% to 90% of its maximum value under light excitation, respectively. Bandwidth is determined as the frequency at which the photocurrent is 3 dB lower than the low-frequency response. Noise equivalent power is the optical input power with a signal-to-noise ratio equal to one. For white noise, the noise equivalent

power increases with the square root of the detector bandwidth. Thus, to characterize the noise performance of a detector, it is more convenient to give the noise equivalent power normalized for frequency bandwidth $\left(\text{NEP}^* = \text{NEP}/\sqrt{\text{BW}}\right)$. Detectivity is the reciprocal of noise equivalent power, which is usually normalized for bandwidth and detector active area A_{opt} $\left(D^* = \sqrt{A_{opt}\text{BW}}/\text{NEP}\right)$.

5.2 The piezo-phototronic effect on photodetectors

Based on the above introduction, it is clear that the fundamental principle of semiconductor photodetectors is the photoelectric effect, a phenomenon in which photoexcited electron and hole pairs are separated by either the Schottky barrier height (from the metal–semiconductor contact) or p–n junction (from p-type and n-type semiconductors).[115] In this context, the Schottky barrier height and p–n junction are critical for the performance of photodetectors and can be effectively tuned by the piezo-phototronic effect. Herein, how the piezo-phototronic effect influences the Schottky barrier height and p–n junction, and thus impacts the property of the photodetector are detailed.

5.2.1 The piezo-phototronic effect on metal–semiconductor contact-based photodetectors. Metal–semiconductor contact is an often-used structure in semiconductor optoelectronics and electronics. A Schottky barrier ($e\varphi_{SB}$) would be built at the metal–semiconductor junction when a metal and an n-type
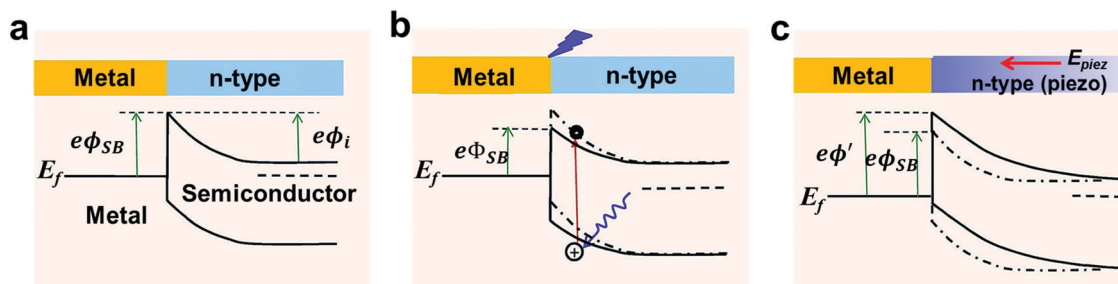
Fig. 20 Energy band diagram for illustrating the effects of laser excitation and piezoelectricity on a Schottky contacted metal–semiconductor interface. (a) Band diagram at a Schottky contacted metal–semiconductor interface. (b) Band diagram at a Schottky contact after exciting by a laser that has a photon energy higher than the bandgap, which is equivalent to a reduction in the Schottky barrier height. (c) Band diagram at the Schottky contact after applying strain in the semiconductor. The piezoelectric potential created in the semiconductor has a polarity with the end in contacting with the metal being low. Reproduced from ref. 21 with permission from WILEY-VCH Verlag GmbH & Co. KGaA, Weinheim, copyright 2012.

semiconductor (the work function of the metal is larger than the electron affinity of the semiconductor) are contacted (Fig. 20a).[21,115] If the polarity of the applied external voltage is higher than the threshold value (φ_i) at the metal side (for an n-type semiconductor), current would be formed and can only pass through this barrier. When light illuminates the metal–semiconductor junction, the incident photons will excite the generation of electron–hole pairs in the semiconductor. The generated electrons in the conduction band and the holes in the valence band tend to move away from the contact and then move towards the interface and metal side, respectively. As a result, the separation and collection of electrons and holes are modulated by the Schottky-contact-created built-in electric field, and thus the photocurrent is generated. Hence, the photocurrent can be controlled by modulating the built-in electric field in the junction region. In addition, the accumulated holes at the interface can tune the local potential profile, leading to a lowered effective height of the Schottky barrier and the increased conductance (Fig. 20b).

If the semiconductor under strain has piezoelectric properties, a negative piezoelectric potential at the semiconductor side will effectively increase the local Schottky barrier height to $e\varphi'$ (Fig. 20c), which consequently enhances the separation and collection of electrons and holes and leads to an increasing photocurrent. However, the improvement will reach a peak when the polarization charge density increases to a level at which the strong upward bending of the valence band edge is large enough to restrain the hole transport. Conversely, a positive piezoelectric potential will reduce the barrier height, and the carrier separation would be weakened by the decreased Schottky barrier height, which can also facilitate electron transport. Thus, the introduced piezoelectric potential can effectively change the local contact characteristics *via* the internal electric field depending on the crystallographic orientation of the piezoelectric semiconductor and the sign of the strain, which tunes/gates the charge carrier transport process at the metal–semiconductor contact.

On the other hand, if the energy of photons exciting the metal–semiconductor contact is larger than the bandgap of the semiconductor, electrons and holes will be generated within the vicinity of the contact. The free carriers at the interface can

effectively reduce the Schottky barrier height. That is to say, piezoelectric potential and laser excitation can increase and reduce the local barrier height, respectively, and thus control the charge transport behavior at the interface. These two effects (the coupling effect between piezoelectricity and photon excitation called the piezo-phototronic effect) could be employed in a complimentary way to modulate the photodetection process.

5.2.2 The piezo-phototronic effect on p–n junction-based photodetectors. The working principle of the piezo-phototronic effect on p–n junction-based photodetectors is the same as that on solar cells, modulating the specific performance by tuning the energy band structure and the photogenerated carrier behavior at the junction interface of p-type and n-type semiconductors (as depicted in Fig. 13, described in Section 4.2). Therefore, to avoid repetition, no further elaboration on the detailed process of the piezo-phototronic effect manipulating the performance of p–n junction-based photodetection is offered here.

Based on the above discussions, piezo-phototronic photodetection processes can be summarized in three points.[116] First, piezo-phototronic photodetection requires an appropriate charge barrier (such as Schottky barrier, p–n junction, and some special heterostructures). Under the charge barrier, a small number of piezoelectric charges can effectively control the current transport properties of photodetectors. Second, the current–voltage characteristic can be tuned by excess photoexcited free charges. Third, the piezoelectric effect plays a significant role in photodetection *via* strain-induced polarization charges at the interface of material junctions (adjusting the charge barrier height). Hence, to introduce the piezo-phototronic effect into photodetectors and significantly influence the properties of photodetectors, it is necessary to construct semiconductor photodetectors with piezoelectric nature and appropriate heights of Schottky barriers (between the metal and semiconductor) or the p–n junction (between two semiconductors). In addition, the external strain applied to photodetectors should also be optimized (*e.g.*, compressive or tensile strain, and the magnitude of the applied strain).

5.3 Photodetectors with the piezo-phototronic effect

Based on the mechanism of the piezo-phototronic effect on modulating photodetectors as discussed above, different types

Table 4 Representative photodetectors implementing the piezo-phototronic effect and their performance modulated by the piezo-phototronic effect

Materials	Applied strain, light and bias	Performance enhancement		
		Photocurrent	Photoresponsivity	Ref.
ZnO/Spiro-MeOTAD	0.753% tensile strain, 365 nm UV light (1 mW cm^{-2}), 0 V bias	1-Fold	1-Fold	117
Poly(9-vinylcarbazole)/ZnO nanorods/graphene	−1.093% compressive strain, 365 nm UV light, +5 V bias	442%	440%	118
ZnO NWs	40.83 MPa pressure, 3.95 mW cm^{-2} 365 nm UV light, +1 V bias	—	700%	119
ZnO micro/nanowires	−0.36% compressive strain, 4.1 pW, 120.0 pW, 4.1 nW, and 180.4 nW UV light, −5 V bias	—	530% (4.1 pW) 190% (120 pW) 9% (4.1 nW) 15% (180.4 nW)	123
Ag–CdTe nanowire–Ag lateral structure	−0.66% compressive strain, NIR light (808 nm) illumination, 5 V bias	430%	427%	125
γ-InSe self-powered photodetector	0.62% tensile strain, 650 nm light illumination, 0 V bias	696%	—	126
ZnO–CdS micro/nanowire	−0.31% compressive strain, 372 nm visible and 548 nm UV light, 2 V bias	—	10 times	142
ZnO/ZnS nanowire array	0.4 kg compressive load, UV (1.32 mW cm^{-2}), blue (3 mW cm^{-2}) and green (3.2 mW cm^{-2}) light, 1.5 V bias	∼31 times (UV) 18 times (blue) 19 times (green)	An order of magnitude	143
CF/ZnO–CdS double-shell microwire	−0.38% compressive strain, 480, 548 and 372 nm light, 2 V bias	36% (480 nm light)	40–60%	144
Si/ZnO/CdO three-component heterojunctions	0.7 N compressive strain, 365, 450 and 580 nm light, 0 V bias	14.6% (365 nm) 35.2% (450 nm) 23.2% (580 nm)	—	145
CH$_3$NH$_3$PbI$_3$ single crystal	43.48 kPa compressive pressure, 680 nm light irradiation, 2 V bias	120%	—	153
WS$_2$/CsPbBr$_3$	0.108% tensile strain	—	1.5 times	159
P3HT–CsPbBr$_3$/Au	−0.29% external compressive strain, 532 nm laser illumination, 2 V bias	3.5 times	7 times	160

of detectors with the piezo-phototronic effect have been implemented for enhancing their photocurrent and photoresponsivity. According to the material composition and structure, three kinds of photodetectors (*i.e.*, single semiconductor-based, heterojunction-based and perovskite-based photodetectors) will be reviewed in the following and some of them are summarized in Table 4.

5.3.1 Single semiconductor-based photodetectors. In general, semiconductors exhibiting the piezoelectric effect (mainly in the wurtzite family such as ZnO, GaN, AlN and InP) have aroused significant attention in recent years attributed to their unique semiconducting, piezoelectric and optoelectronic properties, which have been widely used in electronic, optoelectronic, environmental treatment and energy generation fields.[117–119] Typically, a large variety of ZnO nanowire-based photodetectors with high performance have been developed by utilizing the piezo-phototronic effect of ZnO.[120–122] For instance, single ZnO micro/nanowire photodetectors (a metal–semiconductor–metal device) were prepared by bonding ZnO micro/nanowires laterally on a polystyrene (PS) substrate, the contacts at the two ends of which are two back-to-back Schottky contacts.[123] To investigate the influence of the piezo-phototronic effect on the properties of the photodetector, the authors designed an experimental setup (Fig. 21). During the experiment, an axial compressive or tensile strain was applied on the ZnO nanowire by bending the PS substrate, and the applied strain was quantified by the

maximum deflection of the free end of the substrate. The responsivity of the constructed single ZnO nanowire-based photodetector was studied under different light intensities, and the results indicated that the responsivity was improved by 530%, 190%, 9%, and 15% under 4.1 pW, 120.0 pW, 4.1 nW, and 180.4 nW UV light illumination in the presence of a −0.36% compressive strain over the ZnO wire, respectively. To deduce the mechanism of strain tuning on the responsivity of the photodetector and the effect of light intensity, the piezoelectric potential distribution in the ZnO nanowire without natural doping was simulated with the finite element method. The calculation results suggested that when the nanowire was located along the *c*-axis direction from the drain to source side, a positive potential drop was formed along the ZnO nanowire under compressive strain, and the Schottky barrier height at the drain contact was decreased as the compressive strain increased, leading to boosted photocurrent and responsivity. In addition, the effect of piezoelectric potential on the responsivity of the photodetector weakened with the increases in light intensity, which may be caused by the screening effect of the newly generated charge carriers to piezoelectric potential. Upon high intensity light illumination, a large number of free electrons and holes of the ZnO nanowire were generated, which accumulated at the surface with piezoelectric potential and partially screened the piezoelectric potential (the effect of piezoelectric potential on charge separation was weakened
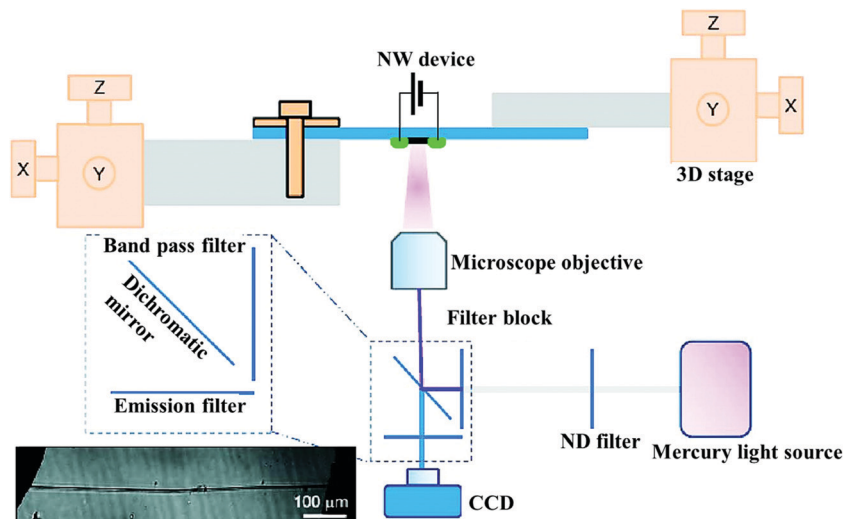
Fig. 21 Schematic diagram of the measurement system to characterize the performance of the piezoelectric potential-tuned photodetector. An optical microscopy image of a ZnO wire device is shown. Reproduced from ref. 123 with permission from American Chemical Society, copyright 2010.

and the responsivity of the photodetector was therefore slightly improved).

CdTe, a group II–VI semiconductor showing a direct bandgap of about 1.5 eV at room temperature, is regarded as a promising material for various optoelectronic applications in the visible region.[124] Moreover, it has been reported that zinc blende CdTe is also a promising piezoelectric material with a piezoelectric coefficient of 0.035 C m^{-2}.[125] In this context, CdTe nanowires with a single crystalline zinc blende structure were combined with silver paste as electrodes to fabricate photodetectors with a Ag–CdTe nanowire–Ag lateral structure.[125] The prepared photodetector presented a broadband photoresponsivity from UV to

NIR light (325–808 nm). Fig. 22a and b demonstrate that when a moderate compressive strain of 0.66% was applied on the device, the photocurrent and photoresponsivity were improved by 430% and 427% under NIR light (808 nm) illumination compared with that obtained without strain, respectively. Significantly, to gain a deeper insight into the physical mechanisms of strain-induced piezoelectric potential enhancement of photodetector performance, the authors analyzed the energy band diagrams at the local metal–semiconductor interface under mechanical deformations (Fig. 22c–e). Two back-to-back Schottky barrier contacts at the drain and source sides were created in the vicinity of the semiconductor CdTe and Ag electrode, respectively. When light
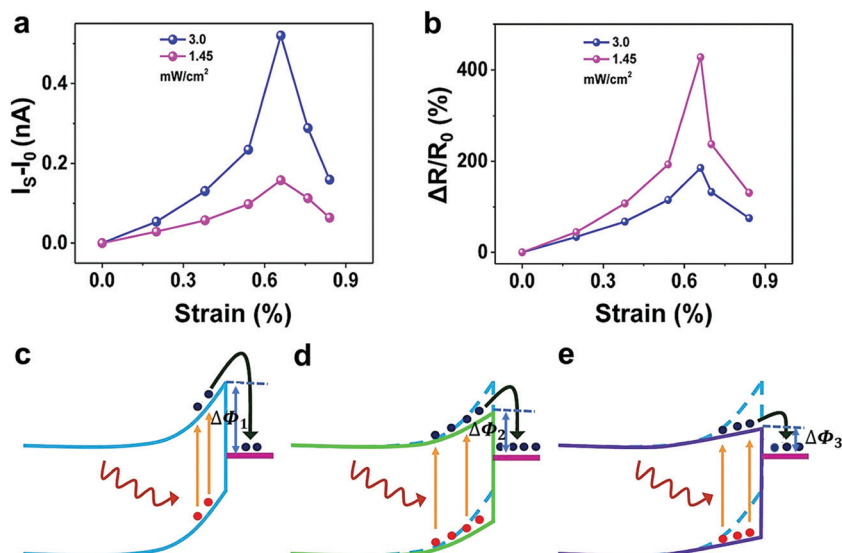

Fig. 22 Changes in the (a) photocurrent (I_0 and I_s are the photocurrent under free strain and different strain intensities, respectively) and (b) responsivity (R_0 is the responsivity under free strain); the excitation wavelength is 808 nm. Energy schematics for illustrating the piezo-phototronic effect on a Schottky contacted metal–semiconductor interface when (c) only illumination, (d) small compressive strain and illumination, and (e) large compressive strain and illumination are applied to the ultra-fine CdTe nanowire-based photodetector. Reproduced from ref. 125 with permission from AIP Publishing, copyright 2019.

with a photon energy higher than or equal to the bandgap of the CdTe nanowire shined on the photodetector device without strain, the electrons and holes of CdTe were excited, and some of them were separated and collected in the vicinity of the metal–semiconductor contact (Fig. 22c). The photogenerated carrier separation and transport led to the formation of photocurrent. In the presence of light irradiation and applied compressive strain, piezoelectric polarization was generated on the side of CdTe nanowires and thus inner piezoelectric potential was introduced, which could function as a driving force to promote the redistribution of free charges. As a consequence, the Schottky barrier height was modified by the piezoelectric charges, following the below equation:

$$\Delta\varphi_{\text{piezo}} = -\frac{1}{2\varepsilon}\rho_{\text{piezo}}W_{\text{piezo}}{}^2 \tag{1}$$

where φ_{piezo} and W_{piezo} are the strain-induced piezoelectric charge density at the semiconductor side of the Schottky contact and the width of the piezoelectric polarization charge distribution adjacent to the interface.

Moreover, the current flowing through the Schottky barrier of the piezoelectric photodetector can be described with the following equation:

$$J = J_{\text{DO}} \exp\left(\frac{qe_{33}s_{33}W_{\text{piezo}}}{2\varepsilon_s kT}\right)\left[\exp\left(\frac{qV}{kT}\right) - 1\right] \tag{2}$$

in which J_{DO}, s_{33} and e_{33} represent the saturation density in the absence of piezoelectric charges, axial strain and piezocoefficient, respectively. It indicates that the current across the Schottky contact is an exponential function of external strain, which can serve as a key factor to tune the current of piezoelectric photodetectors with Schottky contact.

Therefore, a small compressive strain can introduce relatively low-density polarization charges in the vicinity of the metal–semiconductor contact and consequently form a lower Schottky barrier height (Fig. 22d). The strain-induced Schottky barrier height change ($\Delta\Phi_2$) is evaluated by $\Delta\Phi = -kT\ln(I_s/I_0)$, in which k, T, I_s and I_0 stand for the Boltzmann constant, temperature, the measured current under a fixed bias with and without strain, respectively. A decreased Schottky barrier height ($\Delta\Phi_2 < \Delta\Phi_1$) would facilitate electron transport across the metal–semiconductor interface and thus give rise to increased photocurrent. On the other hand, a reduced Schottky barrier height would decrease the interface depletion layer and weaken the internal electric field as the applied compressive strain increases gradually. The reduction of the depletion layer and built-in electric field can be suppressed by the separation of photogenerated carriers, resulting in a decrease in photocurrent. Hence, there is a competing process when external strain is applied into the photodetector system, and the enhanced carrier transport caused by the decreased Schottky barrier height plays a more dominant role under a relatively small compressive strain (photocurrent and photoresponsivity boosted with the increase of small strain). Conversely, as the compressive strain is further increased, the Schottky barrier height ($\Delta\Phi_3$) decreases more obviously, and the further reduced

built-in electric field results in a weakened separation of photogenerated carriers, which has an increasingly significant effect on photocurrent as well as photoresponsivity (Fig. 22e). Additionally, a large strain-imparted device fatigue effect can also damage the device and therefore reduce the photocurrent output of the photodetector. This work strongly corroborated that the applied strain-enabled piezoelectric potential played an important role in modulating the Schottky barrier height of single piezoelectric semiconductor-based photodetectors and thus tuning the photocurrent as well as photoresponsivity properties of the photodetectors. More importantly, it provided a simple method to evaluate the effect of piezoelectric potential on photocurrent and corroborated that an appropriate strain was critical for achieving a higher photocurrent and photoresponsivity of the given photodetector devices. Additionally, this work expanded the choice of materials from the wurtzite to the zinc blende family for utilizing the piezo-phototronic effect in the photodetector field.

Although the above-stated traditional semiconductor-based photodetectors exhibit high performance, their fabrication requires rigid lattice-matched substrates, which hinders the fabrication and practical application of these kinds of devices.[126] To solve this issue, a new class of 2D layer-structured piezoelectric semiconductors (*i.e.*, transition metal dichalcogenides, monochalcogenide materials, *etc.*) with good physical and mechanical properties (*e.g.*, a 2D monolayer piezoelectric MoS_2 crystal could withstand relatively large strains and be deformed by a 11% strain without fracture, piezoelectric WSe_2 bilayers possess a prominent mechanical durability of 0.95%, *etc.*) have been developed as potential candidates to prepare flexible electronic and photoelectric devices.[127–134] In addition, compared with the bulk structure, the chemical and optoelectronic properties of 2D single- or few-layered materials are obviously changed, including energy band diagrams, Coulomb interactions, and crystal symmetry.[135] For instance, 2D-layered γ-InSe presents broken inversion symmetry both in odd and even numbers of layers, endowing it with great second-harmonic generation performance. Based on 2D-layered γ-InSe, a self-powered piezoelectric photodetector (Fig. 23a) which can work without an external energy supply was constructed.[126] For comparison, β-InSe (the polarization directions of which are opposite in adjacent layers with an AB stacking sequence, exhibiting comparative centrosymmetric character) based photodetectors were also prepared as a reference. In the presence of external tensile strain, the photocurrents of both multilayer γ-InSe and β-InSe based self-powered photodetectors were improved, and the photocurrent enhancement ratio of the multilayer γ-InSe photodetector was 696%, which was three times greater than that of β-InSe (211%) under a uniaxial tensile strain of 0.62% (Fig. 23b and c). The increase was attributed to the enlarged Schottky barrier height of multilayer γ-InSe due to modulation from the piezo-phototronic effect from tensile strain (Fig. 23d). Moreover, the increased photocurrent, responsivity, and detectivity of multilayer γ-InSe self-powered photodetectors under a 0.31% tensile strain demonstrated that a strain-imparted piezo-phototronic effect
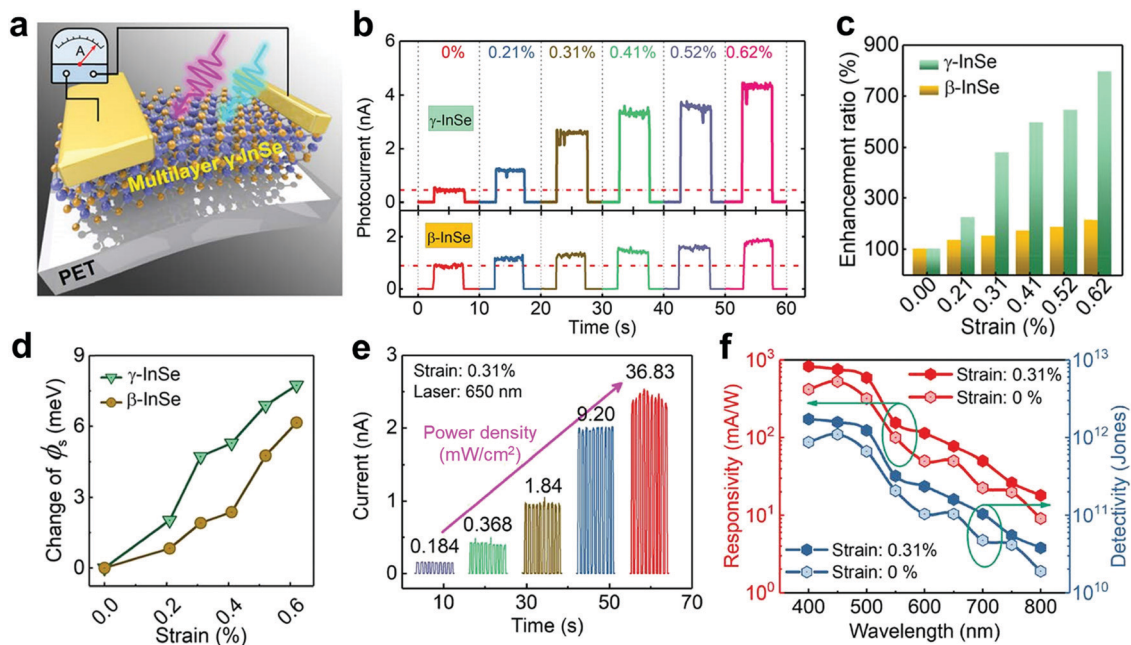
Fig. 23 (a) Schematic diagram of the prepared multilayer γ-InSe self-powered photodetector. (b) Photoswitching characteristics of the InSe self-powered photodetector with different tensile strains under 650 nm light illumination, the corresponding (c) enhancement ratio of photocurrent, and (d) Schottky barrier height change of φ_s to the applied tensile stain. (e) Transient $I–t$ characterization of the γ-InSe self-powered photodetector under 650 nm illumination with different power densities and (f) spectral responsivity and detectivity obtained from the γ-InSe photodetector in the presence and absence of a 0.31% tensile strain. Reproduced from ref. 126 with permission from American Chemical Society, copyright 2019.

can universally be used to improve the quantum efficiency (Fig. 23e and f). Moreover, the fabricated photodetector device showed excellent reliability and stability (remain stable for 1000 cycles), and could even work after 6 months of storage with a 20% degradation of photoresponsivity, showing great promise for its practical applications. The utilization of robust piezoelectric and optoelectronic multilayer γ-InSe based self-powered photodetectors presented an opportunity for developing next-generation optoelectronic detectors with excellent performance and offered an avenue to expand the application of 2D piezoelectric materials.

5.3.2 Heterojunction-based photodetectors. Although plenty of single semiconductor-based photodetectors have been developed and exhibit great photodetection performance, they can only

absorb light with an energy higher than their respective energy bandgap.[136,137] This severely restricts the wide spectral sensitivity of photodetectors. To solve this problem, some semiconductor heterojunction-based photodetectors have emerged.[138–141] For example, a novel ZnO–CdS micro/nanowire (CdS nanowire array as the shell and ZnO micro/nanowire as the core) photodetector with rapid light response ranging from visible to UV light (372–548 nm) was prepared (Fig. 24a).[142] The photocurrent and sensitivity of the constructed ZnO–CdS photodetector were 10^3 times higher that of a single CdS nanoribbon based one. These results demonstrated the significance of the construction of semiconductor heterojunction detectors in improving performance. Moreover, when a −0.31% compressive strain was applied to the ZnO–CdS wire photodetector, its
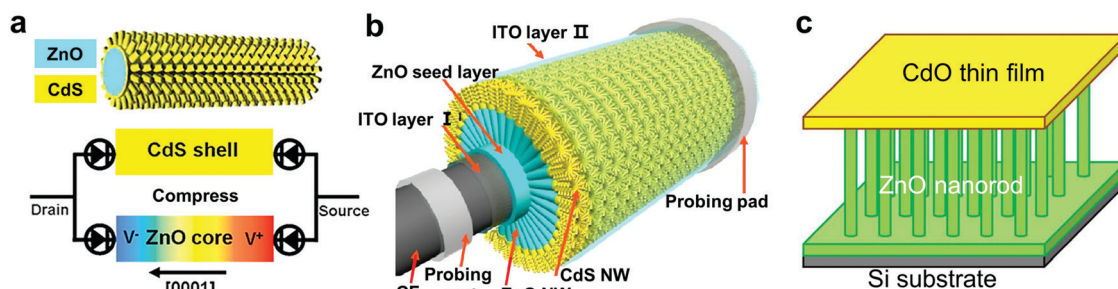

Fig. 24 Schematic diagrams of the constructed heterojunction photodetectors. (a) ZnO–CdS core–shell structure. Reproduced from ref. 142 with permission from American Chemical Society, copyright 2012. (b) CF/ZnO–CdS double core–shell structure. Reproduced from ref. 144 with permission from American Chemical Society, copyright 2013. (c) Si/ZnO/CdO three-component heterojunction. Reproduced from ref. 145 with permission from Elsevier Ltd, copyright 2017.

responsivity was further enhanced more than 10 times compared to that of an unstrained ZnO–CdS wire detector under the irradiation of both visible and UV light. The increase was attributed to the modulation from the piezo-phototronic effect. In addition to a ZnO–CdS core–shell-based photodetector device, another heterojunction core/shell nanowire array ZnO/ZnS photodetector was also fabricated, and it enabled the utilization of wide bandgap materials in broader wavelength (UV to visible light) detection due to the type-II transition at the interface of the ZnO/ZnS core–shell nanowire array structure.[143] The absolute and relative responsivities of the ZnO/ZnS detector were increased by an order and three orders of magnitude with the piezo-phototronic effect, respectively. These studies implied that the fabrication of semiconductor heterojunction photodetectors provided a strategy for broad-spectrum detection applications and that the piezo-phototronic effect can further enhance the photodetector performance.

Furthermore, based on ZnO–CdS core–shell-based photodetectors, carbon-fiber/ZnO–CdS (CF/ZnO–CdS) double-shell microwire photodetectors were prepared, in which branched ZnO–CdS double-shell nanowire arrays were grown on the surface of carbon fiber (Fig. 24b).[144] This new double-shell structure photodetector displayed many advantages. First, the "tree-like" chemical connection of ZnO–CdS possessed a type-II heterostructure that enabled visible/UV broadband sensitivity and facilitated spatial charge separation. Additionally, the outer shell CdS nanowire arrays endowed the structure with an increased specific surface area for visible/UV light absorption and an efficient path for photogenerated electron transport. With the assistance of these advantages, the photodetector showed an excellent response to visible/UV light (from 372 to 548 nm). Notably, the responsivity of the CF/ZnO–CdS wire photodetector was about 10^6 and 10^3 times higher that of a ZnSe nanobelt-based blue/UV-light sensor and a single ZnO–CdS core–shell nanowire-based detector, respectively. Importantly, a −0.38% applied compressive strain further improved the photoresponsivity of the CF/ZnO–CdS wire photodetector by 60% *via* the piezo-phototronic effect compared with that detected without external strain.

In addition to the above-mentioned core–shell structure photodetectors, the piezo-phototronic effect was also employed to enhance the properties of the broadband photodetector Si/ZnO/CdO in three-component heterojunctions.[145] In their work, ZnO nanorods were grown on the surface of a p-type Si substrate, and a layer of CdO thin film was deposited on the ZnO nanorods (Fig. 24c). The constructed Si/ZnO/CdO three-component heterojunction-based photodetector showed a fast and stable response (shorter than 0.45 s) to both the UV and visible light at zero bias. Moreover, the photoresponsivity of Si/ZnO/CdO based photodetectors can be further enhanced by the piezo-phototronic effect introduced by ZnO nanorods. In the presence of a 0.7 N compressive force, the maximal photocurrent of a Si/ZnO/CdO detector was increased by about 14.6%, 35.2% and 23.2% upon illumination with 365, 450 and 580 nm light, respectively.

Additionally, a p-ZnO/Al₂O₃/n-Si heterojunction-based photodetector (an Al₂O₃ layer was deposited on an n-Si wafer, and then Sb-doped p-ZnO nanowire arrays were synthesized on the Al₂O₃ layer) was also recently fabricated, and it showed a wider spectral detection range from UV-vis to NIR (Fig. 25a).[146] In detail, the sensitivities of the p-ZnO/Al₂O₃/n-Si heterojunction-based photodetector reached up to 50 000%, 22 000% and 31 000% under 325, 633, and 1064 nm light illumination, respectively. These values were 34.5, 5.4 and 47.5 times higher than that without Al₂O₃ under the corresponding light excitation (Fig. 25b). This suggested that introducing an insulating Al₂O₃ layer between an n-type and a p-type semiconductor was a simple yet fruitful strategy to improve photodetector sensitivity. Moreover, the photocurrents of p-ZnO/Al₂O₃/n-Si heterojunction-based photodetectors were gradually boosted as the compressive strains increased from 0% to −0.079%, which showed a linear relationship for a broad range of UV-vis-NIR light. The maximum enhancements in the responsivity of the prepared three-component photodetector were 39.7%, 21.8% and 41.0% by UV (365 nm), visible (633 nm) and NIR (1064 nm) light illumination under relatively small external strains, respectively, which was caused by the enhanced separation and collection of photoexcited carriers at the interface of the heterojunction due to the piezo-phototronic effect (Fig. 25c–e). Under UV light irradiation (Fig. 25c), numerous photoexcited carriers were generated at the p-ZnO side (UV light can excite the generation of photoexcited electrons and holes of ZnO), and the holes and electrons in ZnO were directly collected and passed through the interface through Fowler–Nordheim tunneling (FNT) under high reverse bias, respectively. Differently, the active zone consisted of ZnO and Si sides under visible light (Fig. 25d), and both the photoexcited electrons and holes were separated and collected rapidly. In the case of NIR light illumination (Fig. 25e), the active area was dominantly composed of the Si side (attributed to the temperature-dependent thermal emission), in which electrons were directly collected. Generally speaking, photoexcited holes were confined in the Al₂O₃/Si side caused by the large valence band offset and thus promoted charge recombination. On the other hand, the electrons passing through the Al₂O₃ layer were observed to gain a higher kinetic energy and collide with the Al₂O₃ lattice under a high electric field, leading to the excitation of some electrons in the valence band of Al₂O₃ (generating additional carriers). In the presence of external compressive strain, a positive piezoelectric charge was formed at the ZnO/Al₂O₃ interface, most of which would be retained instead of being shielded by local residual free carriers. As a result, the electric field density was increased and a stronger internal electric field was formed. Thus, more efficient separation and collection of photocarriers were achieved. With the increase of applied strain, the piezoelectric potential bended the depletion layer downward and modulated the effective thickness of the tunneling, reducing the accumulated charge density at the ZnO/Al₂O₃ side and resulting in improved photodetector performance. The existing research studies suggested that the piezo-phototronic effect can play a significant role in enhancing the photodetector performance (*i.e.*, responsivity and photocurrent) by designing and constructing tailored heterojunction structure-based photodetectors, which can expand the light
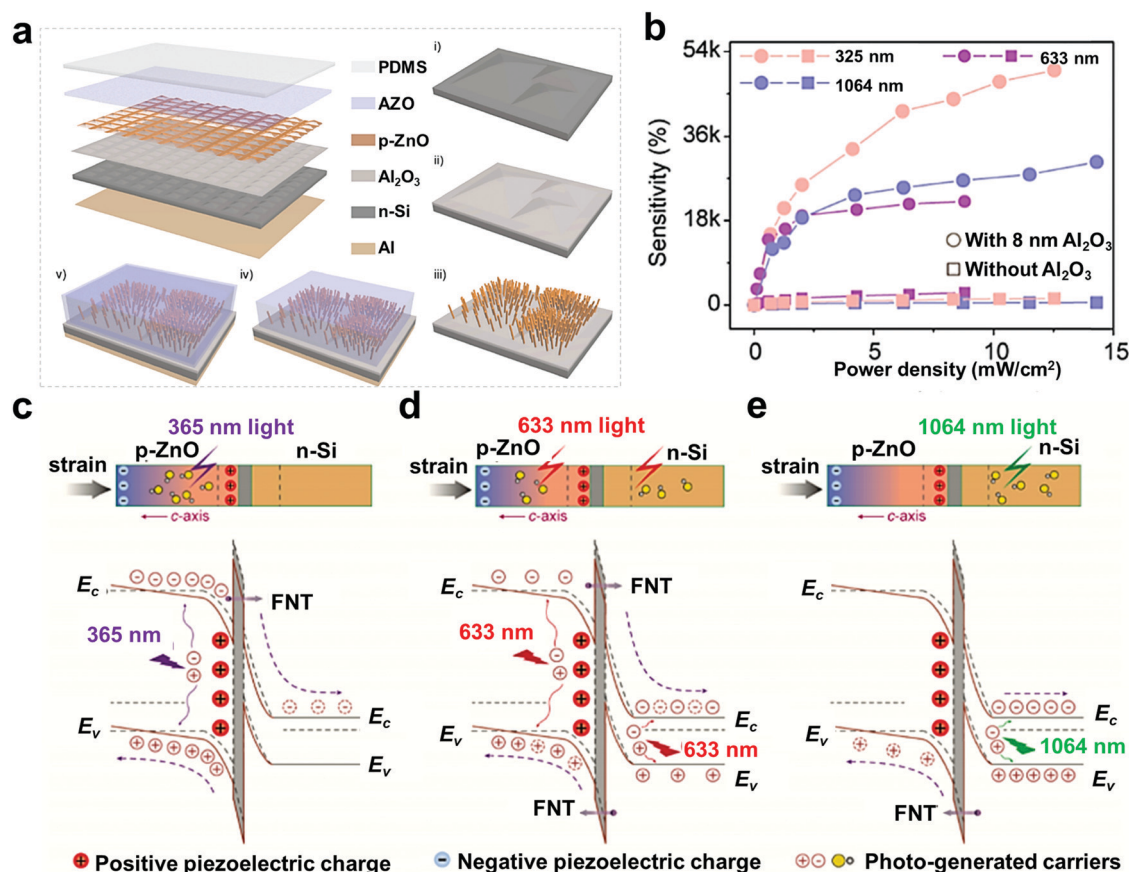
Fig. 25 Schematic illustration of the fabrication process of the p-ZnO/Al$_2$O$_3$/n-Si heterojunction, (b) sensitivity of the photodetector prepared with and without Al$_2$O$_3$ under excitation of 365, 633 and 1064 nm light, and schematic band diagrams of the p-ZnO/Al$_2$O$_3$/n-Si heterojunction under (c) 365 nm, (d) 633 nm and (e) 1064 nm light illumination and compressive strains for elucidating the regulation role of the piezo-phototronic effect in carrier behavior. Reproduced from ref. 146 with permission from Elsevier Ltd, copyright 2021.

response of detectors from UV to visible light and even to NIR.[147–152]

5.3.3 Perovskite-based photodetectors. Traditional semiconductor photodetectors, such as Si and GaN, are widely utilized as photodetectors, especially for UV-light detection. Although these detectors possess superior performance under UV irradiation, they are not suitable for visible light detection. Moreover, these detectors are costly and exhibit a low quantum efficiency. Some conventional photodetectors (including Si photodetectors) need to be operated at a low temperature to reduce the dark-current for detecting very weak light, and preamplifiers are always required to detect ultraweak light.[104] In this background, a three-dimensional lead(II) halide perovskite with the typical structure of ABX$_3$ has emerged and received intensive attention in recent years. In the perovskite, A, B and X stand for organic cations (such as CH$_3$NH$_3^+$ or MA$^+$), inorganic cations (e.g., Pb^{2+} or Sn^{2+}) and halide anions (including I$^-$, Br$^-$ and Cl$^-$), respectively. The urgent need for low-cost and solution-processable optoelectronic devices makes perovskite photodetectors appealing for applications in light detection.[104] In contrast to traditional inorganic semiconductor photodetectors, perovskite-based materials exhibit an appropriate direct band gap (with absorption coefficients up to 10^5 cm^{-1}

in the UV–visible range), a low density of defects and traps within the bandgap, strong optical absorption, superior charge-transport characteristics, and high electrical mobility. Recently, the piezo-phototronic effect was employed to further enhance the performance of perovskite-based photodetectors. Herein, some typical perovskite-based photodetectors with the piezo-phototronic effect are reviewed, including organic–inorganic and all-inorganic perovskite-based photodetectors.

(1) Organic–inorganic perovskite-based photodetectors. CH$_3$NH$_3$PbI$_3$ (MAPbI$_3$) single crystals possess a relatively high piezoelectric coefficient (d_{33} value of 2.7 pm V^{-1}) and are therefore a promising candidate to study the role of the piezo-phototronic effect in enhancing the performance of organic–inorganic perovskite-based photodetectors. As an example, a MAPbI$_3$ single-crystal-based organic–inorganic photodetector was constructed by Lai and co-authors.[153] In their work, poly-3-hexylthiophene (P3HT) was spin-coated on the surface of clean indium-tin oxide (ITO) glass to serve as a hole transport layer. Then, MAPbI$_3$ single crystals were grown on P3TH by a space-confined method. After that, [6,6]-phenyl-C61-butyric acid methyl ester (PCBM) was spin-coated on the MAPbI$_3$ surface as an electron transport layer, followed by depositing a gold

(Au) layer as the top electrode, to form an ITO/P3TH/MAPbI$_3$/PCBM/Au vertical photodetector. Finally, the prepared photodetector was enveloped by PDMS to improve its mechanical properties.[153] Under 680 nm laser illumination (power density of 3.641 mW cm^{-2}), at an external bias (2 V) and a compressive pressure of 43.48 kPa, the photocurrent of the MAPbI$_3$-based photodetector was enhanced by about 120% compared to one without strain. In addition, the response speed of the prepared MAPbI$_3$-based photodetector was 3 and 2 times faster than that obtained without pressure for the light-on and light-off states, respectively. To investigate the enhancement mechanism of the piezo-phototronic effect in the performance of the photodetector, the authors analyzed the energy band diagrams of the photodetector under different compressive pressures (Fig. 26). Fig. 26a–c display the schematic of the cross section and energy band diagrams of the photodetector with no applied pressure, moderate applied pressure, and high applied pressure, respectively. When a 680 nm laser irradiated the surface of the MAPbI$_3$ single crystal, photoinduced carriers were generated and then separated driven by the inner electric field. As the illumination power density increased, many more photoinduced carriers were excited and separated, and thus the photocurrent increased with increasing power density. Under compressive pressure, piezoelectric polarization charges were observed on the surface of the MAPbI$_3$ single crystal due to its noncentrosymmetric structure, and the positive and negative piezoelectric charges were generated simultaneously on the surface of MAPbI$_3$ near PCBM and P3HT, respectively. Therefore, the right-side and left-side energy bands of the MAPbI$_3$ single crystal were moved down and shifted up under a medium compressive pressure, respectively, enhancing the inner electric field and thus promoting charge separation and hindering carrier recombination (Fig. 26c and d). As a result, the photocurrent was increased under an appropriate compressive pressure. When the

compressive pressure was further increased, the piezoelectric potential of the MAPbI$_3$ single crystal became larger and much more piezoelectric charges were generated (Fig. 26e). The right-side energy band of MAPbI$_3$ was further moved down, and the bottom of the conduction band of MAPbI$_3$ was lower than the highest occupied molecular orbital of PCBM, introducing a potential well that could trap photogenerated electrons (Fig. 26f). Therefore, the photocurrent and response speed exhibited a slight decline with further increase of compressive pressure. Based on the above discussion, an optimized pressure existed at which the piezoelectric potential generated by MAPbI$_3$ resulted in a band value between the bottom of the conduction band of MAPbI$_3$ and the highest occupied molecular orbital of PCBM. Notably, the photoresponsivity and its relative change always nearly increased all the time as the pressure increased under lower power densities. This might be attributed to the improved metal–semiconductor contacts, which led to more trapping effect because of the overlapping energy bands. Therefore, to achieve greater photodetector performance (higher photocurrent and faster photoresponsivity), it is necessary to construct perovskite semiconductors with electron and/or hole transport layers with an appropriate energy band structure and introduce suitable mechanical strain (generating beneficial piezoelectric potential at the interface between the junction).

In addition, mixed-cation organic–inorganic Cs$_x$MA$_{1-x}$PbI$_3$ (the Cs$^+$ cation was introduced to replace the organic cation MA$^+$ to induce a certain degree of inner strain and thus bring in spontaneous piezoelectric polarization) perovskite nanowire-based photodetectors with good spontaneous piezoelectric polarization properties were fabricated to study the role of the piezo-phototronic effect in polarization-sensitive photodetectors.[154] It was observed that when the applied strain changed linearly from a +0.31% tensile strain to a −0.31% compressive strain, the photoluminescence (PL) intensity improved from 9.36 to 10.21 for excitation of linearly polarized light. Different PL intensities were detected when the excitation light was right- and left-handed circularly polarized, and the circular dichroism ratio could be modulated from 0.085 to 0.555 (improved 5.5-fold) when the applied strain ranged from a +0.31% tensile strain to a −0.31% compressive strain. A possible mechanism of the piezo-phototronic effect tuning the performance of polarization-sensitive photodetectors is shown in Fig. 27. As depicted in Fig. 27a, without external strain, the spontaneous piezoelectric polarization (thanks to the replacement of the organic cation MA$^+$ by the cation Cs$^+$, giving rise to an inner strain) along the axial direction of the nanowire of the prepared photodetector could direct the separation of photogenerated electrons and holes and thus reduced PL intensity of the photodetector. When compressive strain was applied in the axial direction of the nanowire, the external piezo-potential with the same direction of spontaneous piezoelectric polarization was formed, which promoted the carrier separation and consequently lowered the PL intensity of the perovskite photodetector (Fig. 27b). On the contrary, when tensile strain was introduced in the axial direction of the nanowire, the formed external piezo-potential weakened the spontaneous piezo-potential
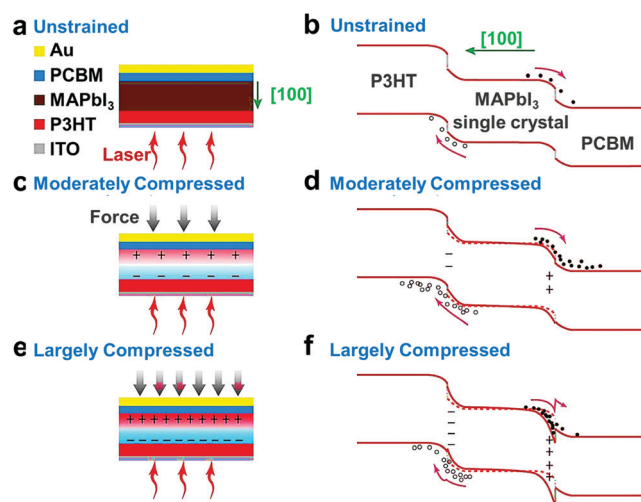

Fig. 26 Schematic structure and energy band diagrams of the perovskite-based device. (a and b) Schematic of the cross section and energy band diagram of the device without applied pressure and under (c and d) a moderate pressure and (e and f) a large pressure. Reproduced from ref. 153 with permission from American Chemical Society, copyright 2018.
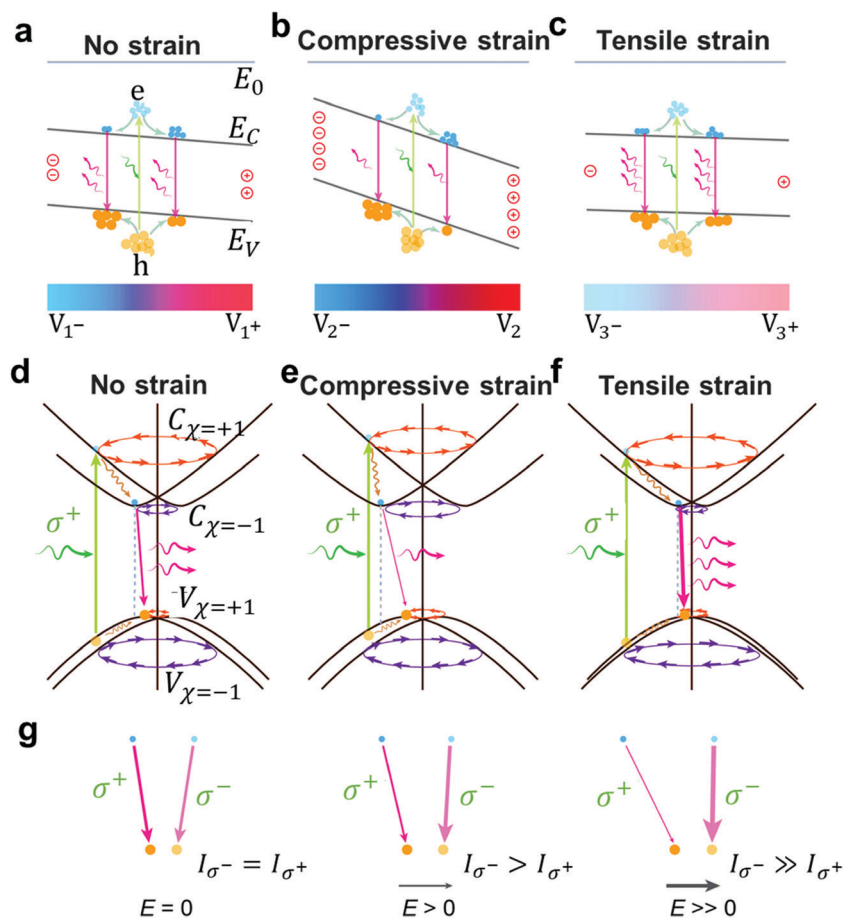
Fig. 27 Mechanisms of the piezo-phototronic effect tuning polarization-sensitive photodetectors. Schematic energy band image with (a) spontaneous piezoelectric polarization even without external strain, (b) enhanced piezoelectric polarization under compressive strain and (c) reduced piezoelectric polarization under tensile strain. Diagrams of Rashba spin-splitting bands and the electron transport paths with (d) no strain, (e) compressive strain and (f) tensile strain, where $C_{\chi=+1}$ ($V_{\chi=+1}$) and $C_{\chi=-1}$ ($V_{\chi=-1}$) represent the "counter-clockwise" and "clockwise" spin texture for conduction (valence) band electrons (holes), respectively. (g) Schematic diagrams depicting the modulation of circular dichroism *via* the effective piezoelectric field. Reproduced from ref. 154 with permission from Elsevier Ltd, copyright 2020.

and reduced the separation of electron–hole pairs, giving rise to increased PL intensity of the photodetector (Fig. 27c). The PL intensity obtained under circularly polarized light was attributed to Rashba spin–orbit coupling by the strong spontaneous piezoelectric polarization along the axial direction of the nanowires, which led to the spin splitting in the energy band (Fig. 27d). The spin polarized electrons and holes were excited by right-handed polarized light and then released to the bottom of the conduction band and the top of the valence band, respectively, where they recombined through an indirect radiative pathway attributed to inelastic photon scattering. Thus, radiative recombination could be restricted (due to the facilitated spin-splitting of the energy band) and promoted (due to the decreased spin-splitting of the energy band) when the photodetector experienced compressive and tensile strains, respectively (Fig. 27e and f). Therefore, the performance of a spontaneously polarized perovskite-based photodetector was manipulated by the piezoelectric field by spin-splitting energy bands and tuning carrier recombination. As presented in Fig. 27g, without an effective piezoelectric field ($E = 0$), no difference in PL intensities with right- and

left-handed helicity was observed. In the presence of a smaller effective piezoelectric field ($E > 0$), the radiative recombination of right- and left-handed excited carriers was suppressed and promoted, respectively, which can be attributed to the momentum mismatches. When a larger effective piezoelectric field was introduced ($E \gg 0$), carrier radiative recombination under left-handed polarized light excitation was much higher than that under right-handed one. Significantly, the results corroborated for the first time that enhanced polarization sensitivity of a photodetector was beneficial for both linearly and circularly polarized light, and that piezo-potential could be employed to efficiently adjust/control linear-polarization and circular-polarization sensitivity *via* the piezo-phototronic effect.

(2) All-inorganic perovskite-based photodetectors. Compared with organic–inorganic perovskite nanomaterials, all-inorganic halide perovskite monocrystals, such as CsPbX$_3$ (X represents Cl, Br or I), show great potential in constructing high-performance photodetectors because of their better stability, lower trap density, and longer carrier diffusion.[155–158] Recently, using

the piezo-phototronic effect to enhance the photocurrent and dark current of $CsPbBr_3$ based photodetectors was investigated by Pan's group.[159] In their work, mechanically exfoliated 2D WS_2 nanoflakes were constructed with single crystal 1D $CsPbBr_3$ nanowires to prepare $WS_2/CsPbBr_3$ van der Waals heterostructure planar photodetectors. The results showed that the photocurrent of $WS_2/CsPbBr_3$ increased with tensile strain and decreased with compressive strain, and external strain was found to exert a negligible effect on its dark current. Moreover, when the applied compressive strain increased from 0% to -0.108%, the responsivity of $WS_2/CsPbBr_3$ was reduced from 0.27 to 0.06 A W^{-1}. Conversely, when the tensile strain increased from 0% to $+0.108\%$, the responsivity of $WS_2/CsPbBr_3$ was boosted to 0.68 A W^{-1}. When the external strain was varied from -0.108% to $+0.108\%$, the photocurrent of $WS_2/CsPbBr_3$ increased 11.3 times. In contrast, the dark current of the $WS_2/CsPbBr_3$ photodetector changed less than 1 pA with strain varying from -0.153% to $+0.153\%$. This indicated that the piezoelectric potential (functioning as a gate voltage) had a relatively weak electric field modulation effect on the $WS_2/CsPbBr_3$ photodetector performance in the dark, and thus the piezo-phototronic effect was the main modulator in the generation, separation, diffusion, and recombination behavior of photon-induced carriers. As shown in Fig. 28a and b, when positive polarization charges were introduced at the interface of $WS_2/CsPbBr_3$ by compressive strain, both the energy bands of WS_2 and $CsPbBr_3$ bended further, and the energy band of WS_2 at the interface bended only very slightly. This was ascribed to the weak electric field modulation effect (red dashed line in Fig. 28b). As a consequence, the barrier for interfacial carrier

transfer was strengthened and the channel depletion remained. Therefore, although incident light was strongly absorbed by the perovskite $CsPbBr_3$, interfacial carrier transfer was hampered and photocurrent was seriously reduced. On the contrary, when tensile strain caused negative polarization charges at the interface of $WS_2/CsPbBr_3$ (Fig. 28c), both the energy bands of WS_2 and $CsPbBr_3$ bended reversely (blue dashed line in Fig. 28d) in comparison with the energy bands in the absence of strain. Thus, the barrier for interfacial carrier transfer was weakened, and interfacial carrier transfer and photocurrent were improved. This study demonstrated the strain-gated performance and strain-sensing function of $WS_2/CsPbBr_3$ planar photodetectors by the piezo-phototronic effect.

Moreover, P3HT–$CsPbBr_3$ monocrystalline microwire-based photodetectors (10 nm SiO_2 was deposited onto the $CsPbBr_3$ microwire, followed by Au NP decoration, then P3HT was deposited on one end of the $CsPbBr_3$ microwire) were constructed to investigate the coupling of surface plasmon resonance and the piezo-phototronic effect in perovskite photodetectors, in which Ag paste served as the electrode connecting P3HT and the free end of the $CsPbBr_3$ microwire, packaged with a PDMS layer to avoid chemical damage.[160] In the presence of a -0.29% external compressive strain, the photocurrent, response speed, and recovery speed of the prepared $CsPbBr_3$/Au hybrid-based photodetector device were increased about 3.5, 70 and 8.4 times under 532 nm laser illumination, respectively. These obvious performance improvements were ascribed to boosted light absorption originating from surface plasmon resonance effects and the enhanced separation of photoexcited carriers at the heterojunction interface, thanks to the piezo-phototronic effect. Significantly, this work demonstrated that the piezo-phototronic effect can couple with surface plasmon resonance to further enhance the performance of photodetectors.

Previous studies corroborated that the photocurrent, on/off ratio, responsivity, and detectivity properties of organic–inorganic and all-inorganic perovskite-based photodetectors could be modulated and optimized by robust and functional material design and by applying appropriate external strain simultaneously. Although great accomplishments have been achieved, many more perovskite-based photodetectors with the piezo-phototronic effect are highly desired for the further development and practical applications of photodetectors.
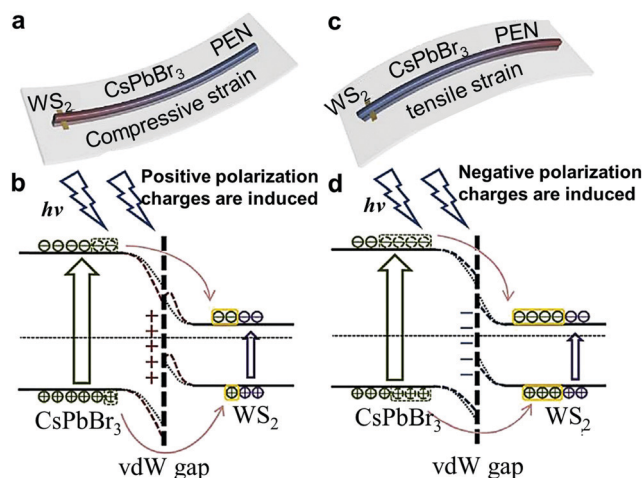

Fig. 28 Schematic illustration of the constructed $WS_2/CsPbBr_3$ photodetector (a) under compressive strain (a positive piezoelectric polarization is induced) and (c) tensile strain (a negative piezoelectric polarization is induced), and (b and d) the corresponding band structures of the $WS_2/CsPbBr_3$ photodetector in (a) and (c), respectively. Notably, the WS_2 channel is depleted; thus, the flat band part of WS_2 is included here only for convenience in depicting the excited and transferred charge carriers within WS_2. The red and blue parts in (a) and (c) indicate a positive and a negative piezoelectric potential, respectively. Reproduced from ref. 159 with permission from Elsevier Ltd, copyright 2019.

6. Piezo-phototronic effect-imparted LEDs

6.1 Fundamental process of LEDs

The first LED was reported in 1928 when Oleg Vladimirovich Losev observed the electroluminescence phenomenon over inorganic semiconductor Si carbide.[161] With great endeavors made in the past decades, numerous varieties of LEDs (for example, monochromatic, infrared, UV, and visible light) have been developed and applied in general illumination, traffic signals, bio-medical treatments, displays, and sensing due to their low-energy-consumption character and fast responsivity.[162–164]

A basic LED device consists of an emitting semiconductor layer sandwiched between a transparent conducting metal oxide anode (*e.g.*, ITO) and a metal cathode (*i.e.*, Ag, Au), as shown in Fig. 29.[89] Fig. 29a depicts a classical single-layered LED, in which only a single layer semiconductor is involved. To achieve a higher efficiency by balancing the injection and transport of electrons and holes, multi-functional layered LEDs have been developed (Fig. 29b) that contain hole-injection layers (HILs), hole-transport layers (HTLs), electron-injection layers (EILs) and electron-transport layers (ETLs). In addition, hole-blocking layers (HBLs) and electron blocking layers (EBLs) have also been constructed in some multilayered LED devices to prevent opposite charge-carrier leakage and thus further increase efficiency. Although the fabrication of multi-layered LED devices is complex, advanced and tailored structures and multi-layer composition designs provide new methods to optimize LED performance. Tandem structure LEDs are another widely used LED architecture. As presented in Fig. 29c, several light-emitting units are connected with a p–n connector in a tandem LED device, which can greatly improve luminous efficiency by producing multiple photons per unit of injected charge. Therefore, tandem LEDs have also been called multiphoton-emission (MPE) LEDs. Importantly, the tandem structure can both improve the operational lifetime of LEDs due to the reduced current density and also endow the device with fewer short-circuit defects. One challenge of tandem LED devices is that their complicated structure makes device preparation much more difficult.

The core component of LEDs is the p–n junction that functions as the emitting layer. The working principle of LEDs is similar to that of p–n junctions, which allows current passing under forward bias but blocks current flow under reverse bias.[165] In detail, when a p-type semiconductor connects with an n-type semiconductor and a p–n junction is formed, the Fermi energies of the two semiconductors will come to the same level without any applied bias. The formed potential difference at the p–n junction will cause bending of the valence and conduction bands. When an external forward bias is applied on the LED device, the holes from the p-type semiconductor will recombine with the electrons in the n-type semiconductor near the p–n junction, and fluorescence is spontaneously emitted to release the excess energy of electrons and holes. When current flows from the LED anode to the cathode under forward bias, light with a certain wavelength (depending on the energy band gap of the semiconductor used in the LED device) will be emitted over the p–n junction and the light intensity is related to the formed current. As a result, the electricity is converted into light energy directly. When reverse bias is applied on LED devices, the injection of minority carriers into the p–n junction is difficult, and thus no light is emitted.

The characteristics of the emitted light are determined by the status and recombination rate of photogenerated carriers as well as the current and the effective charge recombination. Notably, photogenerated carrier separation, recombination, and migration behaviors can be tuned by the energy band structure of semiconductors, which can be manipulated *via* the piezo-phototronic effect. Therefore, to enhance the properties of LEDs, the piezo-phototronic effect was employed and introduced into LED devices.[166–169]

6.2 Mechanism of the piezo-phototronic effect on LEDs

To clearly elucidate the mechanism of how the piezo-phototronic effect regulates the performance of LEDs, the efficiency of LEDs consisting of two kinds of p-type and n-type semiconductors is discussed exclusively, shown in Fig. 30.[21] If the LED device is composed of a p-type piezoelectric semiconductor and an n-type semiconductor (without piezoelectric properties) and external strain is applied on the piezoelectric p-type semiconductor, the preserved local net negative piezoelectric charges at the junction will raise the local energy band of the p-type semiconductor slightly and thus cause the band structure to slope slowly (Fig. 30a), decreasing the recombination rate of photogenerated electrons and holes (the intensity of emitted light is also weakened to some degree). On the
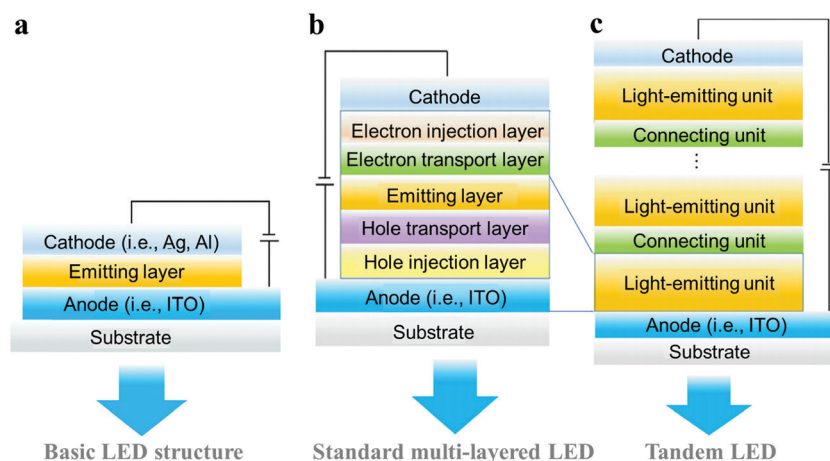

Fig. 29 Structure diagrams of the (a) basic LED, (b) multi-layered LED and (c) tandem LED. Reproduced from ref. 89 with permission from Elsevier Inc, copyright 2019.
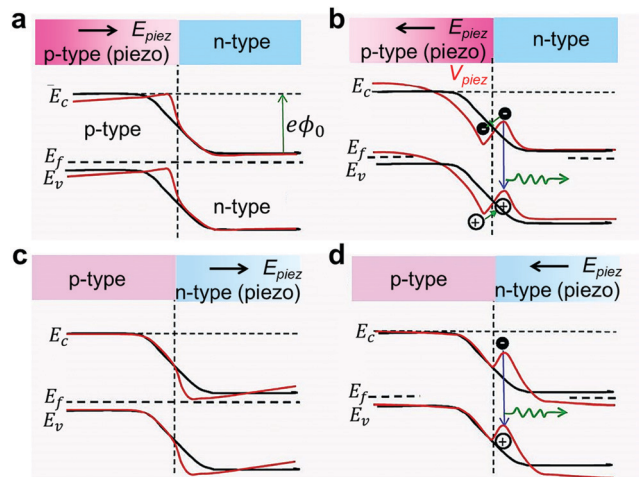
Fig. 30 Energy band diagram illustrating the mechanism as to how the piezo-phototronic effect modulates the carrier behavior and the performance of LEDs composed of two semiconductors with similar bandgaps. The band diagrams for the p–n junction with and without the presence of the piezoelectric effect for four possible cases are shown by black and red curves, respectively. Reproduced from ref. 21 with permission from WILEY-VCH Verlag GmbH & Co. KGaA, Weinheim, copyright 2012.

contrary, if the applied strain changes to the opposite direction, the introduced positive piezoelectric charges at the interface will give rise to the formation of a dip in the local energy band, which can trap the holes (Fig. 30b). Consequently, the possibility of electron–hole recombination is efficiently enhanced, and therefore the efficiency of LEDs is promoted. By the same token, if a p-type semiconductor (without piezoelectric properties) and an n-type piezoelectric semiconductor are combined to prepare a LED device and the n-type semiconductor is subjected to external strain, similar energy band structure changes will occur due to the piezoelectric effect, and the controlled carrier recombination behavior and the corresponding LED's performance will be achieved (Fig. 30c and d). Moreover, if a LED device consists of two piezoelectric semiconductors (p- and n-type semiconductors), a more sophisticated energy band variation and carrier behavior (separation, transport and injection) will occur under applied strain, in which piezoelectric potential functions as a "gate" voltage to manipulate the LED's efficiency.

6.3 Piezo-phototronic effect-modulated LEDs

6.3.1 Traditional inorganic LEDs. High-efficiency light emitters have aroused intensive attention for applications in chemical, biological, and medical technologies. The light emitting properties of semiconductors are determined by carrier injection and recombination as well as extraction efficiency.[170] To achieve higher light emission performance, the piezo-phototronic effect has been employed and introduced into typical traditional inorganic light emitting systems. ZnO, with its good piezoelectric properties and a relatively wide energy bandgap, has been widely used to manufacture optoelectronic devices, which can also be used to construct LED devices with outstanding performance.[24,171–173] Take the inorganic p–n heterojunction semiconductor UV LED device composed of an

n-type ZnO nanowire (with noncentral symmetric character) and p-type GaN as an example.[174] This LED exhibited emission intensity, injection current, and conversion efficiency with the enhancement factors of 17, 4, and 4.25 under an external compressive strain of 0.093% (Fig. 31), respectively. The improved performance was attributed to the piezo-phototronic effect. In detail, under compressive strain, the localized positive piezoelectric potential from ZnO near the GaN/ZnO interface was formed, which led to the creation of carrier trapping channels. This generated carrier channel could then trap and accumulate electrons and holes in the conduction and valence bands, respectively. Because of the abundant available electrons of ZnO, the LED's efficiency was predominately dependent on local hole concentration, and the trapped holes might increase the number of holes injected from p-type GaN into n-type ZnO. Therefore, the carrier recombination rate near the junction interface was boosted and a higher light emission intensity was achieved. Additionally, based on the ZnO nanowire/GaN film (a ZnO nanowire grown on a flexible GaN film substrate) LED, a flexible pressure sensor array possessing high resolution, stability and fast response properties was fabricated to acquire 2D pressure distribution mapping (corresponding to different illumination intensities of LED pixels).[175] Importantly, the intensity of each pixel could be improved by applying compressive strain due to the piezo-phototronic effect. These studies corroborated that the piezo-phototronic effect could play an efficient role in enhancing the light emission properties of LEDs and the corresponding performance of relative optoelectronic devices.

Moreover, Si-based flexible LED array devices (with the merits of being lightweight, energy saving, and highly efficient) exhibit great promise in applications as strain sensors, flexible screens, and human–machine interfaces.[176] To this end, pressure-sensitive Si/ZnO heterojunction matrix white LED arrays were developed (Fig. 32a).[177] The results suggested that the light emission intensity of the single LED heterojunction increased with increasing external strain, reached a maximum value under a compressive strain of 0.15–0.2%, and then decreased when the applied strain was further increased (Fig. 32b). This phenomenon was ascribed to the piezo-phototronic effect on modulating the emission intensity of LEDs by tuning the energy bands at the heterojunction and regulating carrier generation, separation, recombination, and transport behaviors through strain-induced piezoelectric polarization charges (Fig. 32c). Under lower compressive strain, the decreased conduction band edge of ZnO at the interface facilitated electron transport and the dip trapped more electrons at the interface. Therefore, the carrier recombination rate was increased and the number of photons introduced by radiative transition at the interface was boosted. However, when the external strain was further increased and the conduction band edge of ZnO dropped to align with the edge of p-side Si, the light emission intensity reached its peak value. However, when compressive strain continued increasing, the conduction band edge of ZnO was further decreased lower than that of Si, hampering electron transport, and the carrier recombination was restricted consequently. Thus, the light emitting properties of the LEDs
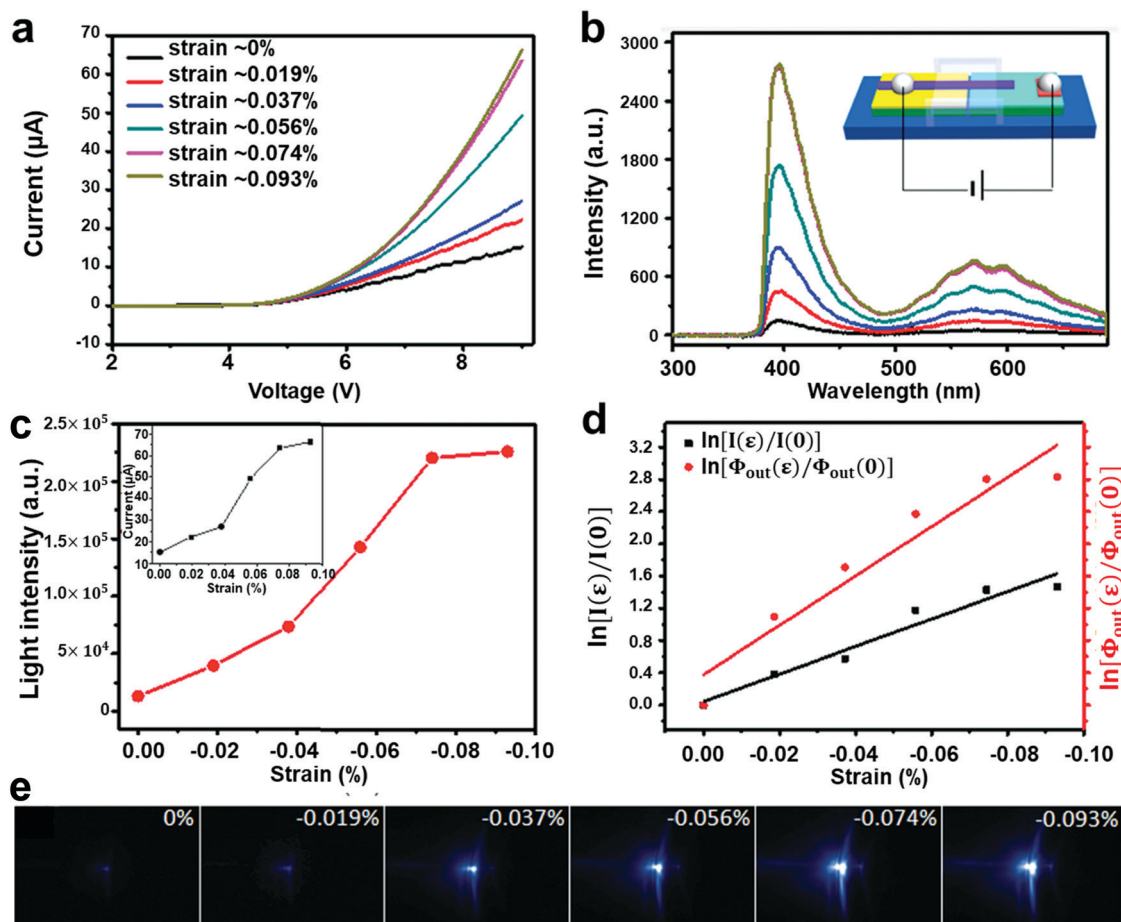
Fig. 31 Enhancement of the emission intensity and conversion efficiency of a (n-ZnO wire)−(p-GaN film) LED under applied strain. (a) *I−V* characteristics of the device under forward bias with the variation of the applied strain; and (b) the corresponding optical spectra of the emitted light at a bias of 9 V (inset: schematic diagram of the fabricated device). (c) Integrated emission light intensities from the data shown in (b) (inset: injection current of the LED at a 9 V bias voltage with the increase of strain). (d) Change in relative injection current $\ln[I(\varepsilon)/I(0)]$ and relative emission light intensity $\ln[\Phi_{out}(\varepsilon)/\Phi_{out}(0)]$ under different strains. (e) CCD images recorded from the emitting end of a packaged single wire LED under different applied strains. Reproduced from ref. 174 with permission from American Chemical Society, copyright 2011.

were hindered. This work not only systematically discussed the influence of the strain-induced piezoelectric potential on the energy bands and charge behaviors of the semiconductor, but also presented the regulatory role of applied strain intensity in the emission intensity of silicon-based LEDs *via* the piezo-phototronic effect. Most importantly, it directly corroborated with experimental data that the piezoelectric potential introduced by applied strain had opposite influences on the performance of LEDs (in the presence of external strain, LEDs properties were enhanced or weakened). Therefore, this work offered a theoretical guideline for achieving a higher LED efficiency by constructing an inorganic piezoelectric semiconductor heterojunction and introducing proper external stress.

Similarly, InGaN/GaN MQW nanopillar based LEDs (composed of n-type GaN, $In_{0.25}Ga_{0.75}N/GaN/In_{0.18}Ga_{0.82}N/$ GaN MQWs and p-type GaN) were fabricated for visible light communication applications (Fig. 33a).[178] The crafted LEDs simultaneously provided a light illumination and communication signal with a low bit error rate. In this work, with the help of the piezo-phototronic effect, the dual-channel transmission

mode (two emission peaks centered at around 452 nm (2.737 eV) and 510 nm (eV)) was obtained (Fig. 33b), where PL intensity outputs in the presence (force on) and absence (force off) of applied compressive force were defined as logical levels "0" and "1" for achieving real-time data transmission. In addition, the regulatory role of the piezo-phototronic effect in modifying luminescence characteristics at a high temperature was also investigated over $In_{0.18}Ga_{0.82}N/GaN$ MQW microstrip array-based LEDs by Du and co-authors (Fig. 33c).[179] In their work, as depicted in Fig. 33d, external strain was applied to the chip with a stress controller and the temperature was continuously tuned by a heating stage. As the temperature increased, the emission intensity at 364 K dropped to 67.8% of that at 300 K without strain. Conversely, the integrated emission light intensity at 364 K was as high as 104% of that at 300 K in the presence of a 0.09% strain (Fig. 33e). The results implied that the external strain-caused piezoelectric potential can tune the quantum transition behavior of photoinduced carriers by changing the energy band structure and therefore increased light emission efficiency. It provided an efficient method to alleviate
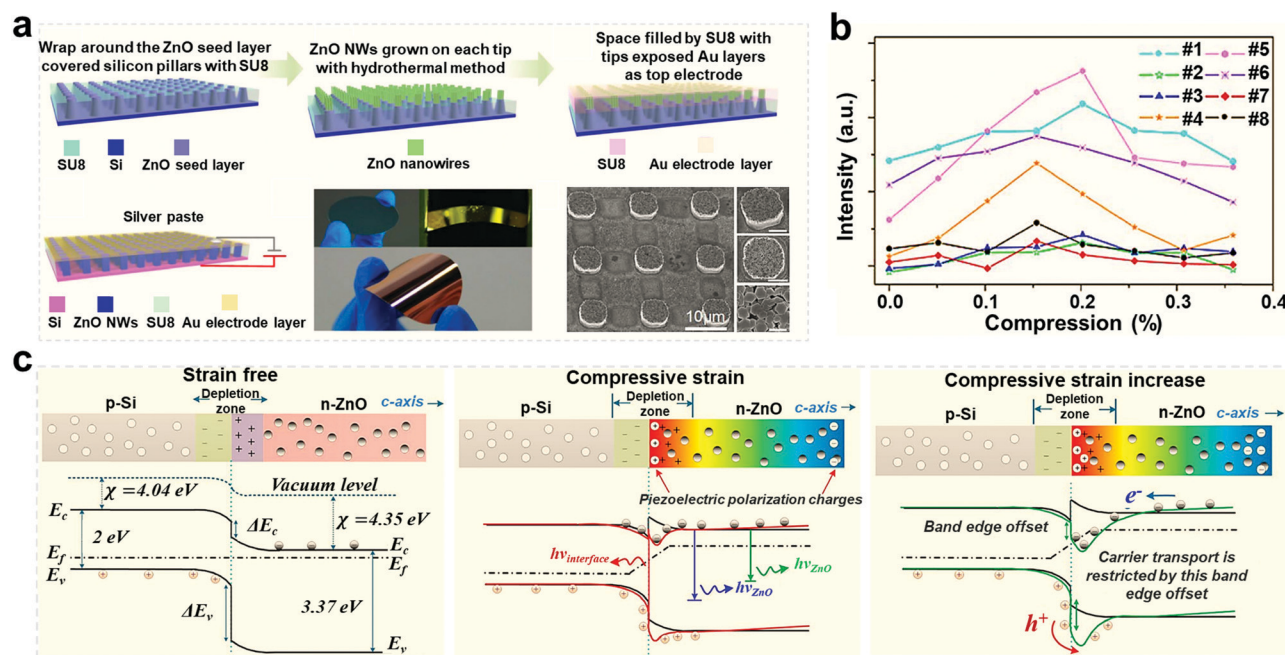
Fig. 32 (a) Schematic diagram of the fabrication process of the Si/ZnO nanowire array heterojunction matrix LED device and the corresponding structure design, the LED device fabricated on a flexible wafer and the SEM image of the ZnO nanowire array grown on p-Si wafers (the scale bar is 3 μm), (b) light intensity changes under increasing compressive strain demonstrated by the calculated intensities for eight single LEDs (each number (1–8) stands for one heterojunction LED), and (c) the mechanism of the piezo-phototronic effect on the light intensity modulation process. Reproduced from ref. 177 with permission from American Chemical Society, copyright 2016.

the negative impact of thermal effects on LEDs for a higher power output. In a wider perspective, the piezo-phototronic effect could facilitate the development and utilization of industrial LEDs.

In addition to p–n heterojunction semiconductors, the homojunction (with the advantage of a similar energy bandgap and crystal structure) can also be employed to manufacture LED devices. For example, p–n homojunction GaN nanowire-based UV LEDs with the wurtzite structure were fabricated (Fig. 33f), and they showed improved light-output efficiency (Fig. 33g) and suppressed efficiency droop with the assistance of the piezo-phototronic effect.[180] In detail, the efficiency droop is dropped from 46.6% to 7.5% and the corresponding droop onset current density gradually increased from 10 to 26.7 A cm^{-2} as the external compressive strain shifted to −0.12% (Fig. 33h). Furthermore, the relative external quantum efficiency of the GaN nanowire-based UV LED device significantly increased by over 600% under an applied compressive strain of −0.12% perpendicular to the homojunction interface, thanks to the piezo-phototronic effect (Fig. 33i). The striking efficiency enhancement of GaN based LEDs was revealed and theoretically confirmed to result in improved electron confinement and boosted hole injection efficiency owing to the piezo-phototronic effect (piezoelectric polarization charges distributing at the homojunction interface tuned the recombination and transport behaviors of the local photoexcited carriers). Notably, this study provided an in-depth understanding of the piezo-phototronic effect on p–n homojunctions, and it presented a robust approach to obtain high light-output efficiency and bright UV or visible light LEDs. In addition, the successful

preparation and utilization of GaN homojunction based LEDs enabled the birth of III-nitride light emitters.

6.3.2 Inorganic/organic hybrid LEDs. Compared with traditional inorganic LEDs, inorganic/organic hybrid LEDs possess the merits of the high flexibility of organic substances (enabling LEDs to be used in flexible conditions and thus extending the practical applications of LEDs), the chemical stability of inorganic semiconductors, high carrier recombination and injection rates, and high extraction efficiency.[181] Therefore, inorganic/organic hybrid LEDs have been integrated into mainstream LEDs, such as wide bandgap ZnO and narrow bandgap CdS based hybrid LEDs. To increase the external quantum efficiency of ZnO based inorganic UV LEDs, a ZnO nanowire/p-polymer (poly(3,4-ethylenedioxythiophene):poly(sodium-p-styrene-sulfonate), PEDOT:PSS) hybrid inorganic/organic LED system was constructed and the piezo-phototronic effect was introduced by applying external strain to further manipulate the carrier behavior (Fig. 34a).[182] The applied strain-imparted piezoelectric polarization charges over ZnO were observed to enhance the external efficiency of the constructed hybrid LEDs at least 2 times (up to 5.92%) in comparison with that detected in samples without strain. The improvement mechanism can be described as shown in Fig. 34b. Due to the high barrier height of about 3 eV between ZnO and PEDOT:PSS, the injection and transport of photogenerated holes from PEDOT:PSS into ZnO were difficult, limiting the recombination rate of carriers. When a proper strain and a forward bias were applied to the fabricated device, however, the energy band structure changed and a dip at the local band was created by the piezoelectric effect. This dip introduced
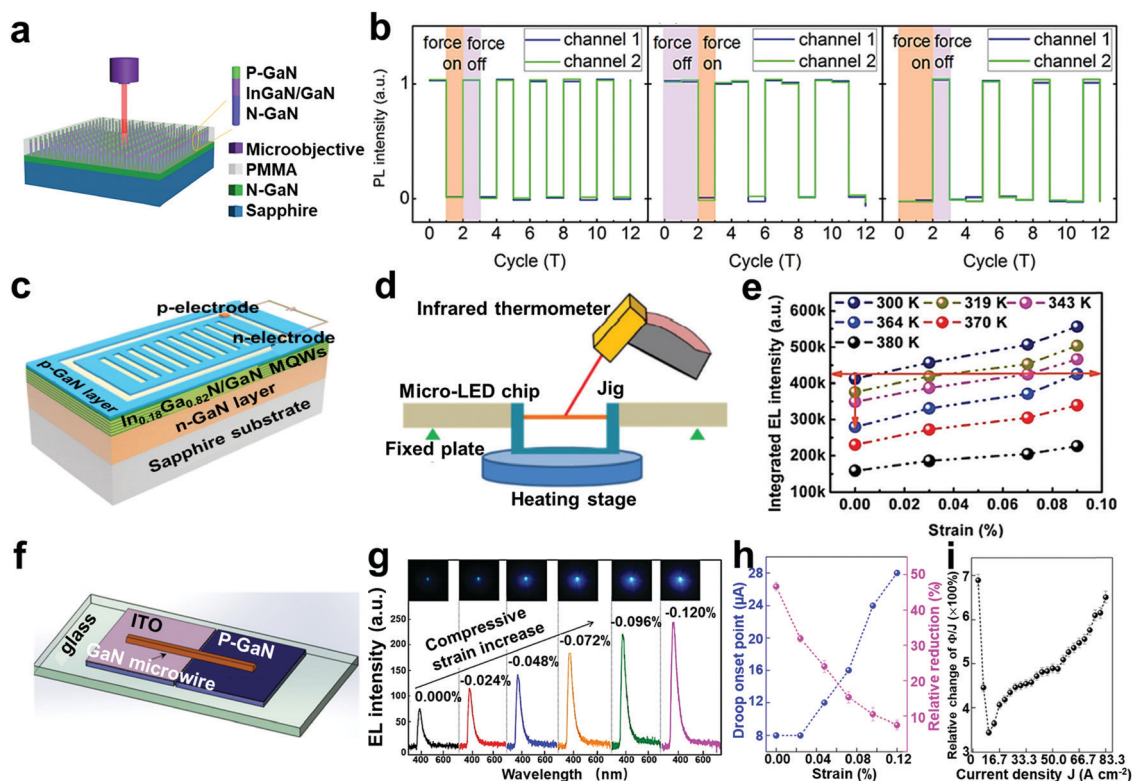
Fig. 33 (a) Schematic diagram of the structure of the prepared InGaN/GaN multi-quantum well nanopillar-based LED. (b) The outputs of different strings of "101010101010," "110110110110," and "001001001001" by the as-prepared light communication systems ("force off" and "force on" refer to the logic states "1" and "0", respectively). Reproduced from ref. 178 with permission from Wiley-VCH Verlag GmbH & Co. KGaA, Weinheim, copyright 2015. (c) Schematic diagram of the as-prepared $In_{0.18}Ga_{0.82}N/GaN$ multi-quantum well microstrip array-based LED. (d) The setup for high-temperature electroluminescence (EL) characteristic measurements. (e) The detected strain dependence of the integrated EL intensity at different temperatures. Reproduced from ref. 179 with permission from The Royal Society of Chemistry, copyright 2018. (f) Schematic diagram of the fabricated GaN microwire-based LED and (g) its optical spectra and corresponding CCD images under various compressive strains. (h) Droop onset current densities and the change of efficiency drop values under external strain and (i) relative change of relative external quantum efficiency (η_{ex}) under different injection current densities. Reproduced from ref. 180 with permission from American Chemical Society, copyright 2017.

a carrier channel to trim electron current to match hole current and improved the localized hole density near the interface. Consequently, the carrier recombination efficiency of the LED device was increased and the light output was significantly boosted. This work offered an available yet efficient method to boost the efficiency of inorganic/organic hybrid flexible LEDs. Based on the above-mentioned work, a flexible LED array composed of organic PEDOT:PSS and patterned inorganic ZnO nanowires with a spatial resolution of 7 μm was fabricated (Fig. 34c).[183] The results indicated that the strain-enabled piezo-electric polarization charges formed at junction interfaces could reduce the barrier height for hole injection from PEDOT:PSS *via* the piezo-phototronic effect and thus facilitated the recombination of electrons and holes in ZnO. This was found to enhance the light-emitting intensity of the prepared flexible LED device (Fig. 34d and e).

In addition to organic polymers, inorganic piezoelectric semiconductors can also be combined with organic light-emitting semiconductors to fabricate hybrid LED devices with higher performance. For instance, a hybrid LED device with the structure of ITO-coated substrate/ZnO nanowire array/4,4'-cyclo-hexylidenebis [*N*,*N*-bis(*p*-tolyl)-aniline] (TAPC) hole transport

layer/tris(4-carbazoyl-9-ylphenyl)amine (TCTA) exciton blocking layer/1,3-di-9-carbazolylbenzene (mCP):tris(2-phenylpyridinato-C^2,*N*)iridium(III) (Ir(ppy)₃) (6 wt%) emitting layer/1,3,5-tris(1-phenyl-1*H*-benzimidazol-2-yl)benzene (TPBi) electron transport layer/LiF electron injection layer/Al electrode was fabricated (Fig. 34f).[184] The light emission of this hybrid device was mainly dependent on the organic light-emitting layer, and the light-emission performance of this organic device was enhanced by ZnO nanowire arrays through modification of their energy band structure and reduction of Schottky barrier height at the interface of the electrode *via* the piezo-phototronic effect (Fig. 34g).

In addition to ZnO, other piezoelectric semiconductors have been combined with organic polymers or organic LEDs to construct hybrid LED devices. For example, CdS nanorods with a direct narrow band gap of 2.4 eV and good piezoelectric properties have been synthesized and combined with organic PEDOT:PSS to investigate the influence of the piezo-phototronic effect on the performance of inorganic/organic hybrid LEDs.[185] A linear relationship between the light emitting performance of the hybrid LED array device and the applied pressure (changing from 0 to 100 MPa) corroborated the significant and versatile role
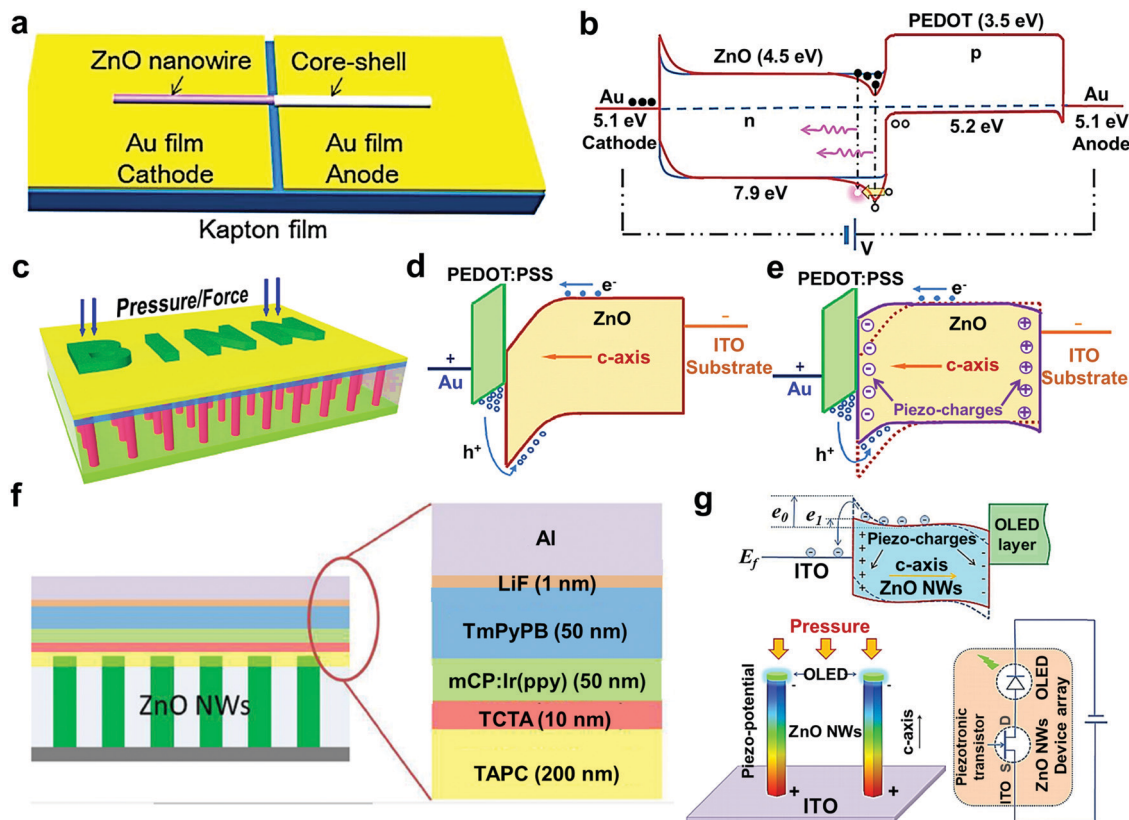
Fig. 34 Schematic diagrams of the (a) ZnO/p-polymer LED device structure and (b) the enhanced light emission under strain for a ZnO/p-polymer core–shell UV LED under different strains (the red and blue lines represent the band diagrams with and without considering the piezo–phototronic effect, respectively). Reproduced from ref. 182 with permission from American Chemical Society, copyright 2013. (c) Schematic diagram of the ZnO/PEDOT:PSS LED device and the band diagrams of an n-ZnO/PEDOT:PSS p–n junction in the (d) absence and (e) presence (solid line in the bottom) of a compressive strain (the local negative piezoelectric charges at the p–n junction region will raise the energy band in the ZnO nanowire near the junction region). Reproduced from ref. 183 with permission from WILEY-VCH Verlag GmbH & Co. KGaA, Weinheim, copyright 2015. (f) Schematic of the ZnO/organic LED and (g) band diagram of ZnO nanowires under compressive strain (solid line) and a device equivalent circuit. Reproduced from ref. 184 with permission from American Chemical Society, copyright 2017.

of the piezo-phototronic effect in modulating the recombination and transport behaviors of photoexcited carriers at the junction interface, and thus improving the light emission intensity of LEDs. Importantly, the prepared CdS/PEDOT:PSS based hybrid LED array possessed excellent flexibility and can be grown on flexible polymers, fibers and clothes, suggesting its great potential in a wide range of applications, such as pressure mapping or sensing and human–machine interfacing.

7. General conclusions and future outlook

7.1 Conclusions

With the rapid development of physics, semiconductors, and nanotechnology, plenty of optoelectronic materials and devices (such as photocatalysts, solar cells, photodetectors and LEDs) have emerged and aroused worldwide attention and how to improve their energy conversion efficiency has become one of the hottest research topics. Although past decades have witnessed great achievements, the quantum yield efficiencies

of these optoelectronic materials and devices are still limited due to the poorly manipulated behavior of photoinduced electron–hole pairs in semiconductors. Recently, the piezo-phototronic effect was proposed and corroborated to be effective at controlling optoelectronic processes and thus improving energy conversion efficiency in optoelectronic materials and devices. Previous studies indicated that the piezo-phototronic effect plays a versatile and robust role in enhancing the performance of photocatalysts, solar cells, photodetectors, and LEDs. This promising enhancement stands as a roadmap to directing the development of optoelectronic materials and devices with a higher energy conversion efficiency. Hence, it is highly desirable to review the recent progress of the piezo-phototronic effect in enhancing the performance of photocatalysts, solar cells, photodetectors and LEDs.

In this review, we summarized the basic principles of photocatalysts, solar cells, photodetectors and LEDs and the barriers preventing high quantum yields. Significantly, the mechanisms of how the piezo-phototronic effect works in the processes of photocatalysts, solar cells, photodetectors and LEDs are discussed in detail with representative material

models. During these optoelectronic processes, the applied strain-enabled piezoelectric field functions as a "gate" and efficiently controls the generation, separation/recombination, and migration behaviors of photoexcited carriers of photocatalysts, solar cells, photodetectors and LEDs by tuning the energy band structure. Moreover, various kinds of photocatalysts, solar cells, photodetectors and LEDs were presented as examples of the favorable and generic role of the piezo-phototronic effect in boosting energy conversion efficiencies. The specific structures, compositions, and properties of the above-mentioned optoelectronic materials and devices are summarized below.

Photocatalysts are semiconductor materials and can covert solar energy into a chemical form. For semiconductor photocatalysts possessing the piezoelectric effect, the piezo-phototronic effect can directly impact their activities in the presence of light illumination and ultrasonic vibration (introducing applied strain over the photocatalyst). Piezoelectric polarization charges are generated on the surface of semiconductors (forming piezoelectric potential) that facilitate the separation of photoexcited electron–hole pairs, resulting in increased photocatalytic activity. For photocatalysts without the piezoelectric effect, the piezo-phototronic effect can also be employed to improve their photocatalytic properties by combining photocatalysts with inorganic or organic piezoelectric substances to form inorganic-based photocatalyst composites or flexible organic piezoelectric-based-photocatalytic hybrids, respectively. The generation of piezoelectric potential on the surface of inorganic piezoelectric substances of inorganic-based photocatalyst composites is mainly dependent on ultrasonic vibration due to the hard nature of inorganic piezoelectrics. Notably, a mild natural low-density energy (*i.e.*, flowing water and wind) is sufficient to drive flexible organic piezoelectrics to form piezoelectric potential and thus promote charge separation of photocatalysts. This opens a door to improve the quantum yield efficiency of photocatalysts under their conventional reaction conditions, enriching the development of photocatalytic technology as well as its practical applications. Importantly, compared with piezoelectric semiconductor photocatalysts, inorganic/organic piezoelectric-based photocatalysts are often constructed with materials that possess better photocatalytic activity and piezoelectric properties (*i.e.*, high electromechanical coupling coefficient and good flexibility), but a compact interface combination between piezoelectrics and photocatalysts is required for piezoelectric potential to efficiently modulate the carrier behavior of the semiconductor photocatalysts. More significantly, the piezo-phototronic effect possesses the ability to couple with other effects (such as local surface plasmon resonance, accelerated mass transfer, and broadened light absorption) to synergistically enhance photocatalytic performance. In addition, the piezo-phototronic effect can not only boost the photocatalytic organic pollution degradation rate, but also improve photocatalytic hydrogen evolution activity and carbon dioxide conversion efficiency, exhibiting great potential in alleviating current energy shortage and environmental contamination issues.

Solar cells are optoelectronic devices that can directly convert solar light into electricity *via* the internal photovoltaic effect and mainly consist of two semiconductors (an n-type semiconductor and a p-type semiconductor), electrodes, an electron transporting layer, a hole transporting layer and an external circuit. The core component of a solar cell is the p–n junction between the two semiconductors, and the photoexcited carrier behavior near the p–n junction predominantly determines the performance of the solar cell. Therefore, the piezo-phototronic effect was introduced in solar cells to improve quantum yield efficiency due to its role in modulating the energy band structure and thus tuning the charge behavior near the junction. Based on this, various kinds of solar cells with the piezo-phototronic effect were developed, including silicon-based solar cells, QDSCs, DSSCs and PSCs. In addition, piezoelectric electron or hole transporting layers connected with the semiconductor (without the piezoelectric effect) can also be chosen and constructed into solar cell devices to execute the piezo-phototronic effect, generating piezoelectric potential under external strain, bending the energy band of semiconductors, and thus controlling carrier behavior as well as optoelectronic properties. Previous investigations substantiate that the J_{SC}, V_{OC}, and PCE of solar cells can be manipulated by the piezo-phototronic effect, which can be further enhanced by coupling with the surface plasmonic resonance effect. It is worth noting that the energy band bending of the semiconductor near the p–n junction caused by piezoelectric potential may promote charge separation or recombination, leading to increased or decreased photocurrent output, respectively. Hence, it is extremely vital to introduce suitable applied strain into specific solar cell systems to optimize photocurrent output and convert solar light into electricity with high quantum yield efficiency.

Photodetectors are optoelectronic devices that detect photons/optical signals and convert them into electrical ones through an internal photoelectric effect. They are often prepared based on metal–semiconductor (forming single semiconductor-based photodetectors) or p–n junction (heterojunction-based photodetectors) contacts. In the photoelectric process of photodetection, the separation of the photoexcited electrons and holes is driven by Schottky barrier height (for metal–semiconductor contact) or the p–n junction, both of which can be impacted by the piezo-phototronic effect. Therefore, the piezo-phototronic effect has been widely employed to adjust the properties of photodetectors consisting of piezoelectric semiconductors by tuning the energy band structure (manipulating the Schottky barrier height or p–n junction) and controlling the carrier separation/recombination behavior. Moreover, compared with single piezoelectric semiconductor-based photodetectors, heterojunction-based photodetectors exhibit the ability to respond within a wider range of light (from UV to visible and even to NIR light), which leads to a higher photocurrent and broadened light detection ability. In addition, piezoelectric perovskite-based photodetectors (including organic–inorganic perovskite-based and all-inorganic perovskite-based photodetectors) possess the advantages of low cost, solution processability, strong optical absorption, and superior charge-transport characteristics in comparison with traditional photodetectors. All these properties could be further improved *via* the

Chem Soc Rev

Review Article

piezo-phototronic effect. Moreover, the construction of self-powered piezoelectric perovskite photodetectors opens an avenue to further enhance their stability and photoresponsivity. Notably, the modulation effect of applied strain-imparted piezoelectric potential on the photocurrent, response speed and responsivity of photodetectors can be affected by incident light density and boosted by the plasmonic resonance effect, and therefore the appropriate applied strain accompanying suitable illumination density as well as ingenious structure design is highly desired to optimize the role of the piezo-phototronic effect in enhancing the photodetector performance.

LEDs are designed to emit light with incoherent wavelengths under electrical injection into a p–n junction (converting electricity into light signals rapidly) and are widely used in illumination and sensing. Similar to solar cells, the vital component of a LED device is the p–n junction, and the behavior of photoexcited carriers near the junction under applied bias remarkably influences the efficiency of LEDs. Based on the fundamental principle of the piezo-phototronic effect and working process of LEDs, many LED devices consisting of a p-/n-type piezoelectric semiconductor or two piezoelectric semiconductors were fabricated, including inorganic piezoelectric heterojunction/homojunction LEDs and flexible inorganic/organic hybrid LEDs. By introducing proper applied compressive or tensile strains, the illumination intensity, sensor resolution and device stability can all be strikingly boosted over the as-prepared LEDs with piezoelectric properties due to the piezo-phototronic effect. This performance can be attributed to the altered carrier behavior (separation, recombination and migration) originating from the bending of energy bands in the semiconductor (resulting from the external strain-enabled piezoelectric potential). In addition, the advent of flexible LED arrays composed of an organic substance and an inorganic piezoelectric semiconductor extends the practical application of LEDs in pressure mapping, light or pressure sensing, and so forth.

7.2 Future outlook

7.2.1 Material and structure designs. On the basis of the above-stated discussions, to execute the profound role of the piezo-phototronic effect in the optoelectronic process of photocatalysts, solar cells, photodetectors and LEDs and consequently enhance their specific performance, it is crucial to construct materials or devices with piezoelectric semiconductors exhibiting high piezoelectric properties and inherent quantum yields. Hence, exploring and developing new efficient piezoelectrics and semiconductors, and combining them into optoelectronic materials and devices have great potential in the fields of energy conversion and utilization. Advanced controllable material synthesis methods and strategies are also expected to craft semiconductors or piezoelectrics with improved properties. Some strategies to synthesize new semiconductors with enhanced properties include confining piezoelectric crystals to grow towards one direction (orientating dipoles) to boost their piezoelectric properties during material preparation processes, introducing an internal electric field into semiconductors to intrinsically facilitate charge separation, exposing a highly reactive crystal facet

of semiconductors to improve carrier generation, and preparing quantum dots or multi-quantum well semiconductors to promote carrier migration.

Second, for the piezo-phototronic effect to work in optoelectronic materials and devices, single piezoelectric semiconductors or piezoelectric–semiconductor composites/hybrids have to be formed and affect the process. For optoelectronic materials and devices constructed with a single piezoelectric semiconductor, there is no doubt that the energy bands and photoinduced carriers are within the control of the applied strain-imparted piezoelectric fields, whereas, when preparing piezoelectric–semiconductor heterojunction/homojunction composites and hybrids (semiconductors with or without the piezoelectric effect grown on flexible piezoelectric organic substrates, for instance), a compact interface bonding between piezoelectrics and semiconductors is highly required for the piezo-phototronic effect to manipulate energy bending and carrier migration. To this end, ingenious and tailored structured composites are welcomed, *i.e.*, core–shell and Janus (Janus nanoparticle/nanorod/nanofiber) structured homojunction/heterojunction-based optoelectronic materials and devices.

Third, as discussed above, the piezo-phototronic effect may improve or weaken the optoelectronic performance of given substances (serving as a "gate" to control energy band bending and carrier behavior), and therefore a proper external driving force (in the same direction as spontaneous polarization with appropriate strength) is indispensable for introducing a piezoelectric field into optoelectronic systems. Natural low-density energy forms, including human motion, water flow, wind, *etc.*, are better to function as driving forces by modifying the physical characteristics of optoelectronic materials and devices (*i.e.*, flexibility, piezoelectric properties, *etc.*). It is vital to optimize the direction and strength of the applied strain to achieve the positive role of the piezo-phototronic effect, which are determined by the semiconductor properties (an n-type or a p-type semiconductor with the piezoelectric effect and the spontaneous polarization direction of piezoelectrics), intrinsic bandgap, and energy band structure near the junctions of semiconductors. To this end, theoretical simulation calculations are highly desired to determine optimal driving forces before conducting specific experiments. Moreover, polarizing piezoelectrics along their spontaneous polarization direction is an efficient route to further improve the potential output under a given strain, which is also anticipated for strengthening the piezo-phototronic effect.

Fourth, the form of external strain needed to drive the generation of a piezoelectric field is mainly determined by the physical character of the optoelectronic materials and devices. For example, the formation of a piezoelectric field over hard inorganic piezoelectric films is predominantly dependent on mechanical strain (like ultrasonic vibration), whereas flexible inorganic or organic piezoelectrics can generate considerable piezoelectric potential under relatively mild external forces (*i.e.*, water flow, wind, finger press). Thus, exploring and developing flexible photocatalysts, solar cells, photodetectors and LEDs (with the piezo-phototronic effect) with much more viable

and ingenious structures, such as flexible helical macro/nano-size fibers, flexible porous films, bionic structures, nano-arrays/films/pillars and so on, stands as a promising strategy to boost the energy conversion efficiency of optoelectronic materials.

Fifth, as reported in previous studies, the piezo-phototronic effect can couple with other effects to synergistically facilitate optoelectronic processes in photocatalysts, solar cells, photodetectors and LEDs. Combining these optoelectronic materials and devices with additional functional components may result in further improved specific performance, which is an exciting new direction in the development of the piezo-phototronic effect and its application in optoelectronic materials and devices. For example, materials with the plasmon resonance effect can endow photocatalysts, solar cells and photodetectors with the ability to respond to visible light, generating much more effective carriers and thus increasing their quantum yield efficiencies; photothermal substances can convert infrared light into thermal energy (increasing system temperature) which can be used to accelerate the migration of photoexcited carriers and consequently boost the reaction rate or responsivity of optoelectronic materials and devices; pyroelectric components may generate electric potential in the presence of temperature variation *via* the pyroelectric effect, which with piezoelectric potential could modulate the carrier behavior and optoelectronic processes. Additionally, constructing the abovementioned optoelectronic devices with all different functional materials/components could also further promote their performance *via* synergistic effects.

7.2.2 Characterization and deep investigation into the modulation of the piezo-phototronic effect on optoelectronic processes. Characterization of piezoelectric properties, potential output, energy band structure changes, and the dynamic generation, and separation/recombination and migration of photoexcited charges is very important for deep insights into the modulation mechanisms of the piezo-phototronic effect on optoelectronic processes for increasing energy conversion efficiency. By now, piezoresponse force microscopy has been reported as the most viable and efficient technology to detect the piezoelectric properties in low-dimensional materials. Unfortunately, it is unable to record the dynamic generation process of piezoelectric fields and the potential output over nano-scale piezoelectrics under external strain in practical applications. Although theoretical simulation calculations based on COMSOL Multiphysics software provide a route to estimate the electric potential formed on the surface of piezoelectrics, there are always some differences between the theoretical and actual values. In this context, optimizing the applied force (with desirable direction and strength) to best utilize the beneficial role of the piezo-phototronic effect in optoelectronic processes remains a challenge. Hence, viable and efficient measurement technologies to detect the real-time piezoelectric potential output during the practical optoelectronic processes of photocatalysts, solar cells, photodetectors or LEDs are greatly needed.

In addition, energy band bending under applied strain-enabled piezoelectric fields and its influence on the separation/recombination and transfer process of photoexcited carriers

cannot be observed directly by experiments at present. This phenomenon is core to understanding the relationship between the piezoelectric field and carrier behavior and therefore needs to be better understood. To this end, in addition to developing advanced characterization strategies, theoretical simulation calculation methods on the basis of Materials Studio, COMSOL Multiphysics and other robust software should be explored and carried out to provide researchers with some guidelines to better understand the physical and chemical essences of the piezo-phototronic effect and more efficiently manipulate/control the optoelectronic processes of photocatalysts, solar cells, photodetectors and LEDs in the future.

Although transient photovoltage, photoelectrochemical characterization, and time-resolved PL technologies have been used to study carrier behavior under light illumination, no viable measurement exists to record the dynamic carrier generation, separation, recombination and transfer processes in the presence of an applied strain-imparted piezoelectric field to the best of our knowledge (because the piezoelectric field is not easy to be introduced when using the above techniques). Furthermore, the potentiation quantitative relationships among the applied external force, generated piezoelectric field, tuned carrier behavior and the enhanced performance of photocatalysts (*i.e.*, photocatalytic degradation rate, hydrogen evolution efficiency, carbon dioxide conversion efficiency), solar cells (PCE, J_{SC} and V_{OC}), photodetectors (photocurrent and responsivity) and LEDs (light emission intensity) are still unknown mysteries. The ascertainment of the abovementioned quantitative relationships will provide researchers working in the field of optoelectronic materials and devices theoretical guidance to carry out experimental investigations and apply them in practical applications. In this regard, it is urgent to develop an efficient strategy to solve this problem.

Conflicts of interest

The authors declare no competing financial interest.

Acknowledgements

References

1 L. Wan, Q. Zhou, X. Wang, T. E. Wood, L. Wang, P. N. Duchesne, J. Guo, X. Yan, M. Xia, Y. F. Li, A. A. Jelle, U. Ulmer, J. Jia, T. Li, W. Sun and G. A. Ozin, *Nat. Catal.*, 2019, **2**, 889–898.

2 A. Akhundi, A. Habibi-Yangjeh, M. Abitorabi and S. Rahim Pouran, *Catal. Rev.*, 2019, **61**, 595–628.

3 K. Asare-Yeboah, Q. Li, C. Jiang, Z. He, S. Bi, Y. Liu and C. Liu, *J. Phys. Chem. Lett.*, 2020, **11**, 6526–6534.

4 M. Fahim, I. Firdous, W. Zhang and W. A. Daoud, *Nano Energy*, 2021, **86**, 106127.

5 Z. Li, L. Zhang, Y. Liu, C. Shao, Y. Gao, F. Fan, J. Wang, J. Li, J. Yan, R. Li and C. Li, *Angew. Chem., Int. Ed.*, 2020, **59**, 935–942.

6 A. Akhundi, A. Habibi-Yangjeh, M. Abitorabi and S. Rahim Pouran, *Catal. Rev.*, 2019, **61**, 595–628.

7 X. Wang, S. Blechert and M. Antonietti, *ACS Catal.*, 2012, **2**, 1596–1606.

8 L. Zheng, S. Han, H. Liu, P. Yu and X. Fang, *Small*, 2016, **12**, 1527–1536.

9 X. Meng, X. Cui, M. Rager, S. Zhang, Z. Wang, J. Yu, Y. W. Harn, Z. Kang, B. K. Wagner, Y. Liu, C. Yu, J. Qiu and Z. Lin, *Nano Energy*, 2018, **52**, 123–133.

10 M. He, B. Li, X. Cui, B. Jiang, Y. He, Y. Chen, D. O. Neil, P. Szymanski, M. A. EI-Sayed, J. Huang and Z. Lin, *Nat. Commun.*, 2017, **8**, 16045.

11 L. Han, M. Peng, Z. Wen, Y. Liu, Y. Zhang, Q. Zhu, H. Lei, S. Liu, L. Zheng, X. Sun and H. Li, *Nano Energy*, 2019, **59**, 492–499.

12 Y. Lee, J. Kwon, E. Hwang, C. Ra, W. J. Yoo, J. Ahn, J. H. Park and J. H. Cho, *Adv. Mater.*, 2015, **27**, 41–46.

13 M. Kneissl, T. Seong, J. Han and H. Amano, *Nat. Photonics*, 2019, **13**, 233–244.

14 Y. Kondo, K. Yoshiura, S. Kitera, H. Nishi, S. Oda, H. Gotoh, Y. Sasada, M. Yanai and T. Hatakeyama, *Nat. Photonics*, 2019, **13**, 678–682.

15 C. Pan, J. Zhai and Z. L. Wang, *Chem. Rev.*, 2019, **119**, 9303–9359.

16 Z. Lu, L. Zeng, W. Song, Z. Qin, D. Zeng and C. Xie, *Appl. Catal., B*, 2017, **202**, 489–499.

17 T. Jia, A. Kolpin, C. Ma, R. C. Chan, W. Kwok and S. C. E. Tsang, *Chem. Commun.*, 2014, **50**, 1185–1188.

18 M. Zalfani, B. van der Schueren, Z. Hu, J. C. Rooke, R. Bourguiga, M. Wu, Y. Li, G. Van Tendeloo and B. Su, *J. Mater. Chem. A*, 2015, **3**, 21244–21256.

19 H. Hengming, D. Baoying, W. Wei, L. Chunhua, K. Jiahui, N. Yaru, W. Lianzhou and X. Zhongzi, *Nano Lett.*, 2017, **17**, 3803–3808.

20 Y. Hu, Y. Zhang, Y. Chang, R. L. Snyder and Z. L. Wang, *ACS Nano*, 2010, **4**, 4220–4224.

21 Z. L. Wang, *Adv. Mater.*, 2012, **24**, 4632–4646.

22 W. Wang, M. O. Tade and Z. Shao, *Chem. Soc. Rev.*, 2015, **44**, 5371–5408.

23 V. Bhavanasi, V. Kumar, K. Parida, J. Wang and P. S. Lee, *ACS Appl. Mater. Interfaces*, 2016, **8**, 521–529.

24 G. Hwang, M. Byun, C. K. Jeong and K. J. Lee, *Adv. Healthcare Mater.*, 2015, **4**, 646–658.

25 L. Pan, S. Sun, Y. Chen, P. Wang, J. Wang, X. Zhang, J. J. Zou and Z. L. Wang, *Adv. Energy Mater.*, 2020, **10**, 2000214.

26 L. Zhu and Z. L. Wang, *Adv. Funct. Mater.*, 2019, **29**, 1808214.

27 C. Pan, M. Chen, R. Yu, Q. Yang, Y. Hu, Y. Zhang and Z. L. Wang, *Adv. Mater.*, 2016, **28**, 1535–1552.

28 J. Curie and P. Curie, *Acad. Sci., Paris, C. R.*, 1880, **91**, 1880.

29 Z. Gao, J. Zhou, Y. Gu, P. Fei, Y. Hao, G. Bao and Z. L. Wang, *J. Appl. Phys.*, 2009, **105**, 113707.

30 Z. L. Wang, *Nano Today*, 2010, **5**, 540–552.

31 Y. Hu, C. Pan and Z. L. Wang, *Semicond. Sci. Technol.*, 2017, **32**, 53002.

32 J. Li, D. Wu, J. Iocozzia, H. Du, X. Liu, Y. Yuan, W. Zhou, Z. Li, Z. Xue and Z. Lin, *Angew. Chem., Int. Ed.*, 2019, **58**, 1985–1989.

33 Q. Wang, M. Nakabayashi, T. Hisatomi, S. Sun, S. Akiyama, Z. Wang, Z. Pan, X. Xiao, T. Watanabe, T. Yamada, N. Shibata, T. Takata and K. Domen, *Nat. Mater.*, 2019, **18**, 827–832.

34 P. Li, X. Chen, H. He, X. Zhou, Y. Zhou and Z. Zou, *Adv. Mater.*, 2018, **30**, 1703119.

35 E. Nurlaela, T. Shinagawa, M. Qureshi, D. S. Dhawale and K. Takanabe, *ACS Catal.*, 2016, **6**, 1713–1722.

36 J. Kou, C. Lu, J. Wang, Y. Chen, Z. Xu and R. S. Varma, *Chem. Rev.*, 2017, **117**, 1445–1514.

37 Y. Park, K. J. McDonald and K. Choi, *Chem. Soc. Rev.*, 2013, **42**, 2321–2337.

38 X. Chen, S. Shen, L. Guo and S. S. Mao, *Chem. Rev.*, 2010, **110**, 6503–6570.

39 H. Wang, L. Zhang, Z. Chen, J. Hu, S. Li, Z. Wang, J. Liu and X. Wang, *Chem. Soc. Rev.*, 2014, **43**, 5234–5244.

40 A. Ajmal, I. Majeed, R. N. Malik, H. Idriss and M. A. Nadeem, *RSC Adv.*, 2014, **4**, 37003–37026.

41 L. Li, P. A. Salvador and G. S. Rohrer, *Nanoscale*, 2013, **6**, 24–42.

42 L. Wang, S. Liu, Z. Wang, Y. Zhou, Y. Qin and Z. L. Wang, *ACS Nano*, 2016, **10**, 2636–2643.

43 Z. Jiang, H. Wang, H. Huang and C. Cao, *Chemosphere*, 2004, **56**, 503–508.

44 Y. Cui, H. Du and L. Wen, *Environ. Chem. Lett.*, 2009, **7**, 321–324.

45 Y. Xu, D. Zhong, J. Jia, K. Li, J. Li and X. Quan, *Chem. Eng. J.*, 2013, **225**, 138–143.

46 H. Li, Y. Sang, S. Chang, X. Huang, Y. Zhang, R. Yang, H. Jiang, H. Liu and Z. L. Wang, *Nano Lett.*, 2015, **15**, 2372–2379.

47 Z. Liang, C. Yan, S. Rtimi and J. Bandara, *Appl. Catal., B*, 2019, **241**, 256–269.

48 H. You, Y. Jia, Z. Wu, X. Xu, W. Qian, Y. Xia and M. Ismail, *Electrochem. Commun.*, 2017, **79**, 55–58.

49 J. Wang, M. Yan, K. Zhao, X. Liao, P. Wang, X. Pan, W. Yang and L. Mai, *Adv. Mater.*, 2017, **29**, 1604464.

50 J. Lin, Y. Tsao, M. Wu, T. Chou, Z. Lin and J. M. Wu, *Nano Energy*, 2017, **31**, 575–581.

51 M. Wang, B. Wang, F. Huang and Z. Lin, *Angew. Chem., Int. Ed.*, 2019, **58**, 7526–7536.

52 S. Singh and N. Khare, *Nano Energy*, 2017, **38**, 335–341.

53 Y. C. Wang and J. M. Wu, *Adv. Funct. Mater.*, 2019, **30**, 1907619.

54 H. A. Abbood, A. Adnan, A. B. Al Hawash, A. A. Abbood and K. Huang, *Catal. Lett.*, 2020, **150**, 3059–3070.

55 X. Xue, W. Zang, P. Deng, Q. Wang, L. Xing, Y. Zhang and Z. L. Wang, *Nano Energy*, 2015, **13**, 414–422.

56 W. Lu, C. M. Quezada and K. Chang, *Mater. Chem. Phys.*, 2020, **247**, 122880.

57 X. Liu, L. Xiao, Y. Zhang and H. Sun, *J. Materiomics*, 2020, **6**, 256–262.

58 Y. Wang and K. Chang, *J. Am. Ceram. Soc.*, 2016, **99**, 2593–2600.

59 X. Zhou, Q. Sun, D. Zhai, G. Xue, H. Luo and D. Zhang, *Nano Energy*, 2021, **84**, 105936.

60 D. Liu, C. Jin, Y. Zhang, Y. He and F. Wang, *Ceram. Int.*, 2021, **47**, 7692–7699.

61 K. Wang, Z. Fang, X. Huang, W. Feng, Y. Wang, B. Wang and P. Liu, *Chem. Commun.*, 2017, **53**, 9765–9768.

62 Y. Zhao, X. Huang, F. Gao, L. Zhang, Q. Tian, Z. Fang and P. Liu, *Nanoscale*, 2019, **11**, 9085–9090.

63 C. Hu, H. Huang, F. Chen, Y. Zhang, H. Yu and T. Ma, *Adv. Funct. Mater.*, 2020, **30**, 1908168.

64 L. Zhang, D. Zhu, H. He, Q. Wang, L. Xing and X. Xue, *J. Phys. Chem. Solids*, 2017, **102**, 27–33.

65 L. Guo, C. Zhong, J. Cao, Y. Hao, M. Lei, K. Bi, Q. Sun and Z. L. Wang, *Nano Energy*, 2019, **62**, 513–520.

66 D. Kumar, S. Sharma and N. Khare, *Renewable Energy*, 2021, **163**, 1569–1579.

67 H. Li, Y. Sang, S. Chang, X. Huang, Y. Zhang, R. Yang, H. Jiang, H. Liu and Z. L. Wang, *Nano Lett.*, 2015, **15**, 2372–2379.

68 X. Guo, Y. Fu, D. Hong, B. Yu, H. He, Q. Wang, L. Xing and X. Xue, *Nanotechnology*, 2016, **27**, 375704.

69 D. Hong, W. Zang, X. Guo, Y. Fu, H. He, J. Sun, L. Xing, B. Liu and X. Xue, *ACS Appl. Mater. Interfaces*, 2016, **8**, 21302–21314.

70 G. Venugopal, S. Thangavel, V. Vasudevan and K. Zoltán, *J. Phys. Chem. Solids*, 2020, **143**, 109473.

71 Q. Shi, M. Zhang, Z. Zhang, Y. Li, Y. Qu, Z. Liu, J. Yang, M. Xie and W. Han, *Nano Energy*, 2020, **69**, 104448.

72 B. Dai, C. Lu, J. Kou, Z. Xu and F. Wang, *J. Alloys Compd.*, 2017, **696**, 988–995.

73 B. Dai, L. Zhang, H. Huang, C. Lu, J. Kou and Z. Xu, *Appl. Surf. Sci.*, 2017, **403**, 9–14.

74 Y. Li, Q. Wang, H. Wang, J. Tian and H. Cui, *J. Colloid Interface Sci.*, 2019, **537**, 206–214.

75 Y. Yu, B. Yao, H. He, B. Cao, Y. Ren and Q. Sun, *Appl. Surf. Sci.*, 2020, **528**, 146819.

76 Y. Kim, Y. Xie, X. Wen, S. Wang, S. J. Kim, H. Song and Z. L. Wang, *Nano Energy*, 2015, **14**, 77–86.

77 R. Tian, Q. Xu, C. Lu, X. Duan and R. Xiong, *Chem. Commun.*, 2017, **53**, 7933–7936.

78 B. Dai, H. Huang, W. Wang, Y. Chen, C. Lu, J. Kou, L. Wang, F. Wang and Z. Xu, *Catal. Sci. Technol.*, 2017, **7**, 5594–5601.

79 B. Dai, H. Huang, F. Wang, C. Lu, J. Kou, L. Wang and Z. Xu, *Chem. Eng. J.*, 2018, **347**, 263–272.

80 W. Tong, Y. Zhang, H. Huang, K. Xiao, S. Yu, Y. Zhou, L. Liu, H. Li, L. Liu, T. Huang, M. Li, Q. Zhang, R. Du and Q. An, *Nano Energy*, 2018, **53**, 513–523.

81 W. Wu, X. Yin, B. Dai, J. Kou, Y. Ni and C. Lu, *Appl. Surf. Sci.*, 2020, **517**, 146119.

82 B. Dai, Y. Yu, Y. Chen, H. Huang, C. Lu, J. Kou, Y. Zhao and Z. Xu, *Adv. Funct. Mater.*, 2019, **29**, 1807934.

83 Y. Chen, J. Fang, B. Dai, H. Wei, J. Kou and C. Lu, *Catal. Sci. Technol.*, 2020, **10**, 2337–2342.

84 P. Mandal and S. Sharma, *Renewable Sustainable Energy Rev.*, 2016, **65**, 537–552.

85 C. Xu and Z. L. Wang, *Adv. Mater.*, 2011, **23**, 873–877.

86 D. Sengupta, P. Das, B. Mondal and K. Mukherjee, *Renewable Sustainable Energy Rev.*, 2016, **60**, 356–376.

87 K. Gu, D. Zheng, L. Li and Y. Zhang, *RSC Adv.*, 2018, **8**, 8694–8698.

88 G. Richhariya, A. Kumar, P. Tekasakul and B. Gupta, *Renewable Sustainable Energy Rev.*, 2017, **69**, 705–718.

89 F. Wang, X. Liu and F. Gao, *Advanced Nanomaterials for Solar Cells and Light Emitting Diodes*, Elsevier, 2019, pp. 1–35.

90 A. Polman, M. Knight, E. C. Garnett, B. Ehrler and W. C. Sinke, *Science*, 2016, **352**, d4424.

91 X. Wen, W. Wu and Z. L. Wang, *Nano Energy*, 2013, **2**, 1093–1100.

92 D. Q. Zheng, Z. Zhao, R. Huang, J. Nie, L. Li and Y. Zhang, *Nano Energy*, 2017, **32**, 448–453.

93 W. Wu and Z. L. Wang, *Nat. Rev. Mater.*, 2016, **1**, 1–17.

94 M. Que, R. Zhou, X. Wang, Z. Yuan, G. Hu and C. Pan, *J. Phys.: Condens. Matter*, 2016, **28**, 433001.

95 G. Shen, MSc thesis, Hebei University, 2019.

96 L. Zhu, L. Wang, C. Pan, L. Chen, F. Xue, B. Chen, L. Yang, L. Su and Z. L. Wang, *ACS Nano*, 2017, **11**, 1894–1900.

97 E. H. Sargent, *Nat. Photonics*, 2012, **6**, 133–135.

98 W. A. Tisdale, K. J. Williams, B. A. Timp, D. J. Norris, E. S. Aydil and X. Zhu, *Science*, 2010, **328**, 1543–1547.

99 J. Shi, P. Zhao and X. Wang, *Adv. Mater.*, 2013, **25**, 916–921.

100 C. Jiang, L. Jing, X. Huang, M. Liu, C. Du, T. Liu, X. Pu, W. Hu and Z. L. Wang, *ACS Nano*, 2017, **11**, 9405–9412.

101 C. Jiang, Y. Chen, J. Sun, L. Jing, M. Liu, T. Liu, Y. Pan, X. Pu, B. Ma, W. Hu and Z. L. Wang, *Nano Energy*, 2019, **57**, 300–306.

102 S. Bettini, R. Pagano, L. Valli and G. Giancane, *Chem. – Asian J.*, 2016, **11**, 1240–1245.

103 R. Wang, M. Mujahid, Y. Duan, Z. K. Wang, J. Xue and Y. Yang, *Adv. Funct. Mater.*, 2019, **29**, 1808843.

104 M. Ahmadi, T. Wu and B. Hu, *Adv. Mater.*, 2017, **29**, 1605242.

105 L. Zhu, L. Wang, F. Xue, L. Chen, J. Fu, X. Feng, T. Li and Z. L. Wang, *Adv. Sci.*, 2017, **4**, 1600185.

106 C. Pan, S. Niu, Y. Ding, L. Dong, R. Yu, Y. Liu, G. Zhu and Z. L. Wang, *Nano Lett.*, 2012, **12**, 3302–3307.

107 Y. You, W. Liao, D. Zhao, H. Ye, Y. Zhang, Q. Zhou, X. Niu, J. Wang, P. Li, D. Fu, Z. Wang, S. Gao, K. Yang, J. Liu, J. Li, Y. Yan and R. Xiong, *Science*, 2017, **357**, 306–309.

108 Y. Zhang, Y. Yang and Z. L. Wang, *Energy Environ. Sci.*, 2012, **5**, 6850–6856.

109 S. Qiao, J. Liu, G. Fu, K. Ren, Z. Li, S. Wang and C. Pan, *Nano Energy*, 2018, **49**, 508–514.

110 G. Hu, W. Guo, R. Yu, X. Yang, R. Zhou, C. Pan and Z. L. Wang, *Nano Energy*, 2016, **23**, 27–33.

111 J. Sun, Q. Hua, R. Zhou, D. Li, W. Guo, X. Li, G. Hu, C. Shan, Q. Meng, L. Dong, C. Pan and Z. L. Wang, *ACS Nano*, 2019, **13**, 4507–4513.

112 Y. Wang, D. Zheng, L. Li and Y. Zhang, *ACS Appl. Energy Mater.*, 2018, **1**, 3063–3069.

113 E. Monroy, F. Omn Es and F. Calle, *Semicond. Sci. Technol.*, 2003, R33–R51.

114 Q. Zheng, M. Peng, Z. Liu, S. Li, R. Han, H. Ouyang, Y. Fan, C. Pan, W. Hu, J. Zhai, Z. Li and Z. L. Wang, *Sci. Adv.*, 2021, **7**, e7738.

115 X. Han, M. Chen, C. Pan and Z. L. Wang, *J. Mater. Chem. C*, 2016, **4**, 11341–11354.

116 Y. Liu, Q. Yang, Y. Zhang, Z. Yang and Z. L. Wang, *Adv. Mater.*, 2012, **24**, 1410–1417.

117 Y. Shen, X. Yan, H. Si, P. Lin, Y. Liu, Y. Sun and Y. Zhang, *ACS Appl. Mater. Interfaces*, 2016, **8**, 6137–6143.

118 X. Zhang, J. Zhang, B. Leng, J. Li, Z. Ma, W. Yang, F. Liu and B. Liu, *Adv. Mater. Interfaces*, 2019, **6**, 1901365.

119 X. Han, W. Du, R. Yu, C. Pan and Z. L. Wang, *Adv. Mater.*, 2015, **27**, 7963–7969.

120 Z. Zhang, Q. Liao, Y. Yu, X. Wang and Y. Zhang, *Nano Energy*, 2014, **9**, 237–244.

121 W. Zhang, D. Jiang, M. Zhao, Y. Duan, X. Zhou, X. Yang, C. Shan, J. Qin, S. Gao, Q. Liang and J. Hou, *J. Appl. Phys.*, 2019, **125**, 24502.

122 C. An, H. Qi, L. Wang, X. Fu, A. Wang, Z. L. Wang and J. Liu, *Nano Energy*, 2021, **82**, 105653.

123 Q. Yang, X. Guo, W. Wang, Y. Zhang, S. Xu, D. H. Lien and Z. L. Wang, *ACS Nano*, 2010, **4**, 6285–6291.

124 D. Lee, G. Mohan Kumar, P. Ilanchezhiyan, F. Xiao, S. U. Yuldashev, Y. Woo, D. Kim and T. Kang, *Nanomaterials*, 2019, **9**, 178.

125 X. Wang, G. Dai, Y. Chen, X. Mo, X. Li, W. Huang, J. Sun and J. Yang, *J. Appl. Phys.*, 2019, **125**, 94505.

126 M. Dai, H. Chen, F. Wang, Y. Hu, S. Wei, J. Zhang, Z. Wang, T. Zhai and P. Hu, *ACS Nano*, 2019, **13**, 7291–7299.

127 K. Zhang, M. Peng, W. Wu, J. Guo, G. Gao, Y. Liu, J. Kou, R. Wen, Y. Lei, A. Yu, Y. Zhang, J. Zhai and Z. L. Wang, *Mater. Horiz.*, 2017, **4**, 274–280.

128 P. Lin, L. Zhu, D. Li, L. Xu and Z. L. Wang, *Nanoscale*, 2018, **10**, 14472–14479.

129 W. Wu, L. Wang, R. Yu, Y. Liu, S. Wei, J. Hone and Z. L. Wang, *Adv. Mater.*, 2016, **28**, 8463–8468.

130 X. Wang, P. Wang, J. Wang, W. Hu, X. Zhou, N. Guo, H. Huang, S. Sun, H. Shen, T. Lin, M. Tang, L. Liao, A. Jiang, J. Sun, X. Meng, X. Chen, W. Lu and J. Chu, *Adv. Mater.*, 2015, **27**, 6575–6581.

131 P. Lin, L. Zhu, D. Li, L. Xu, C. Pan and Z. Wang, *Adv. Funct. Mater.*, 2018, **28**, 1802849.

132 F. Xue, L. Chen, J. Chen, J. Liu, L. Wang, M. Chen, Y. Pang, X. Yang, G. Gao, J. Zhai and Z. L. Wang, *Adv. Mater.*, 2016, **28**, 3391–3398.

133 C. W. Jang, H. Kim, M. K. Nazeeruddin, D. H. Shin and S. Choi, *Nano Energy*, 2021, **84**, 105899.

134 G. Michael, G. Hu, D. Zheng and Y. Zhang, *J. Phys. D: Appl. Phys.*, 2019, **52**, 204001.

135 K. Rogdakis, N. Karakostas and E. Kymakis, *Energy Environ. Sci.*, 2021, **14**, 3352–3392.

136 P. Sahatiya and S. Badhulika, *J. Mater. Chem. C*, 2017, **5**, 11436–11447.

137 M. Chen, B. Zhao, G. Hu, X. Fang, H. Wang, L. Wang, J. Luo, X. Han, X. Wang, C. Pan and Z. L. Wang, *Adv. Funct. Mater.*, 2018, **28**, 1706379.

138 Z. Wang, R. Yu, X. Wen, Y. Liu, C. Pan, W. Wu and Z. L. Wang, *ACS Nano*, 2014, **8**, 12866–12873.

139 J. Liu, Y. Zhang, C. Liu, M. Peng, A. Yu, J. Kou, W. Liu, J. Zhai and J. Liu, *Nanoscale Res. Lett.*, 2016, **11**, 281.

140 J. Sun, P. Li, R. Gao, X. Lu, C. Li, Y. Lang, X. Zhang and J. Bian, *Appl. Surf. Sci.*, 2018, **427**, 613–619.

141 D. J. Lee, S. R. Ryu, G. M. Kumar, H. D. Cho, D. Y. Kim and P. Ilanchezhiyan, *Appl. Surf. Sci.*, 2021, **558**, 149896.

142 F. Zhang, Y. Ding, Y. Zhang, X. Zhang and Z. L. Wang, *ACS Nano*, 2012, **6**, 9229–9236.

143 S. C. Rai, K. Wang, Y. Ding, J. K. Marmon, M. Bhatt, Y. Zhang, W. Zhou and Z. L. Wang, *ACS Nano*, 2015, **9**, 6419–6427.

144 F. Zhang, S. Niu, W. Guo, G. Zhu, Y. Liu, X. Zhang and Z. L. Wang, *ACS Nano*, 2013, **7**, 4537–4544.

145 B. Yin, H. Zhang, Y. Qiu, Y. Luo, Y. Zhao and L. Hu, *Nano Energy*, 2017, **40**, 440–446.

146 Z. Huo, Y. Zhang, X. Han, W. Wu, W. Yang, X. Wang, M. Zhou and C. Pan, *Nano Energy*, 2021, **86**, 106090.

147 K. Zhang, M. Peng, W. Wu, J. Guo, G. Gao, Y. Liu, J. Kou, R. Wen, Y. Lei, A. Yu, Y. Zhang, J. Zhai and Z. L. Wang, *Mater. Horiz.*, 2017, **4**, 274–280.

148 F. Li, W. Peng, Z. Pan and Y. He, *Nano Energy*, 2018, **48**, 27–34.

149 Y. Chen, C. Wang, G. Chen, Y. Li and C. Liu, *Nano Energy*, 2015, **11**, 533–539.

150 A. Sarkar, A. K. Katiyar, S. Mukherjee and S. K. Ray, *J. Phys. D: Appl. Phys.*, 2017, **50**, 145104.

151 Z. Zhao and Y. Dai, *Phys. Chem. Chem. Phys.*, 2019, **21**, 9574–9580.

152 X. Yu, H. Yin, H. Li, W. Zhang, H. Zhao, C. Li and M. Zhu, *Nano Energy*, 2017, **34**, 155–163.

153 Q. Lai, L. Zhu, Y. Pang, L. Xu, J. Chen, Z. Ren, J. Luo, L. Wang, L. Chen, K. Han, P. Lin, D. Li, S. Lin, B. Chen, C. Pan and Z. L. Wang, *ACS Nano*, 2018, **12**, 10501–10508.

154 L. Zhu, Q. Lai, W. Zhai, B. Chen and Z. L. Wang, *Mater. Today*, 2020, **37**, 56–63.

155 J. Liang, J. Liu and Z. Jin, *Sol. RRL*, 2017, **1**, 1700086.

156 C. Bao, J. Yang, S. Bai, W. Xu, Z. Yan, Q. Xu, J. Liu, W. Zhang and F. Gao, *Adv. Mater.*, 2018, **30**, 1803422.

157 T. Yang, Y. Zheng, Z. Du, W. Liu, Z. Yang, F. Gao, L. Wang, K. Chou, X. Hou and W. Yang, *ACS Nano*, 2018, **12**, 1611–1617.

158 M. Xue, H. Zhou, G. Ma, L. Yang, Z. Song, J. Zhang and H. Wang, *Sol. Energy Mater. Sol. Cells*, 2018, **187**, 69–75.

159 Q. Xu, Z. Yang, D. Peng, J. Xi, P. Lin, Y. Cheng, K. Liu and C. Pan, *Nano Energy*, 2019, **65**, 104001.

160 Z. Yang, M. Jiang, L. Guo, G. Hu, Y. Gu, J. Xi, Z. Huo, F. Li, S. Wang and C. Pan, *Nano Energy*, 2021, **85**, 105951.

161 N. Zheludev, *Nat. Photonics*, 2007, **1**, 189–192.

162 Z. Guo, H. Li, L. Zhou, D. Zhao, Y. Wu, Z. Zhang, W. Zhang, C. Li and J. Yao, *Small*, 2015, **11**, 438–445.

163 S. Tsai, C. Lu and C. Liu, *Nano Energy*, 2016, **28**, 373–379.

164 W. Z. Tawfik, G. Y. Hyeon and J. K. Lee, *J. Appl. Phys.*, 2014, **116**, 164503.

165 B. Xu, PhD thesis, Tianjing University, 2015.

166 X. Li, M. Chen, R. Yu, T. Zhang, D. Song, R. Liang, Q. Zhang, S. Cheng, L. Dong, A. Pan, Z. L. Wang, J. Zhu and C. Pan, *Adv. Mater.*, 2015, **27**, 4447–4453.

167 R. Bao, J. Tao, C. Pan and Z. L. Wang, *Small Sci.*, 2021, **1**, 2000060.

168 Z. Huo, Y. Peng, Y. Zhang, G. Gao, B. Wan, W. Wu, Z. Yang, X. Wang and C. Pan, *Adv. Mater. Interfaces*, 2018, **5**, 1801061.

169 J. Li, R. Bao, J. Tao, Y. Peng and C. Pan, *J. Mater. Chem. C*, 2018, **6**, 11878–11892.

170 C. Pan, L. Dong, G. Zhu, S. Niu, R. Yu, Q. Yang, Y. Liu and Z. L. Wang, *Nat. Photonics*, 2013, **7**, 752–758.

171 K. Momeni and H. Attariani, *Phys. Chem. Chem. Phys.*, 2014, **16**, 4522–4527.

172 Q. Guo, D. Li, Q. Hua, K. Ji, W. Sun, W. Hu and Z. L. Wang, *Nano Lett.*, 2021, **21**, 4062–4070.

173 J. Lu, C. Xu, F. Li, Z. Yang, Y. Peng, X. Li, M. Que, C. Pan and Z. L. Wang, *ACS Nano*, 2018, **12**, 11899–11906.

174 Q. Yang, W. Wang, S. Xu and Z. L. Wang, *Nano Lett.*, 2011, **11**, 4012–4017.

175 Y. Peng, M. Que, H. E. Lee, R. Bao, X. Wang, J. Lu, Z. Yuan, X. Li, J. Tao, J. Sun, J. Zhai, K. J. Lee and C. Pan, *Nano Energy*, 2019, **58**, 633–640.

176 X. Li, R. Liang, J. Tao, Z. Peng, Q. Xu, X. Han, X. Wang, C. Wang, J. Zhu, C. Pan and Z. L. Wang, *ACS Nano*, 2017, **11**, 3883–3889.

177 M. Chen, C. Pan, T. Zhang, X. Li, R. Liang and Z. L. Wang, *ACS Nano*, 2016, **10**, 6074–6079.

178 C. Du, C. Jiang, P. Zuo, X. Huang, X. Pu, Z. Zhao, Y. Zhou, L. Li, H. Chen, W. Hu and Z. L. Wang, *Small*, 2015, **11**, 6071–6077.

179 C. Du, L. Jing, C. Jiang, T. Liu, X. Pu, J. Sun, D. Li and W. Hu, *Mater. Horiz.*, 2018, **5**, 116–122.

180 X. Wang, W. Peng, R. Yu, H. Zou, Y. Dai, Y. Zi, C. Wu, S. Li and Z. L. Wang, *Nano Lett.*, 2017, **17**, 3718–3724.

181 C. Wang, R. Bao, K. Zhao, T. Zhang, L. Dong and C. Pan, *Nano Energy*, 2015, **14**, 364–371.

182 Q. Yang, Y. Liu, C. Pan, J. Chen, X. Wen and Z. L. Wang, *Nano Lett.*, 2013, **13**, 607–613.

183 R. Bao, C. Wang, L. Dong, R. Yu, K. Zhao, Z. L. Wang and C. Pan, *Adv. Funct. Mater.*, 2015, **25**, 2884–2891.

184 R. Bao, C. Wang, Z. Peng, C. Ma, L. Dong and C. Pan, *ACS Photonics*, 2017, **4**, 1344–1349.

185 R. Bao, C. Wang, L. Dong, C. Shen, K. Zhao and C. Pan, *Nanoscale*, 2016, **8**, 8078–8082.